# Structural Design and Analysis of an Earth Observation 3U CubeSat for Hyperspectral Imaging

Pratheek Ranjan Mitra

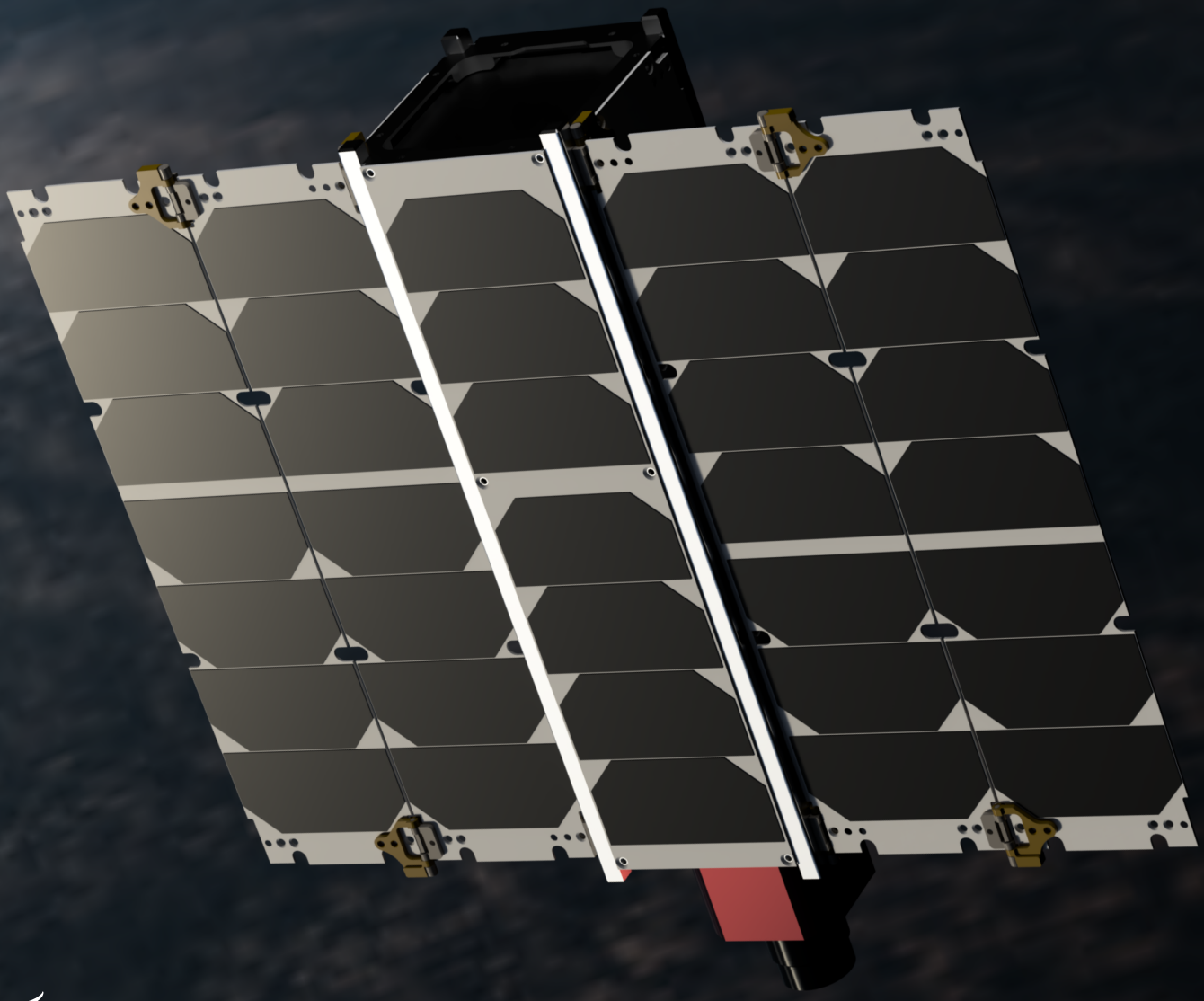

TU Delft

# Structural Design and Analysis of an Earth Observation 3U CubeSat for Hyperspectral Imaging

## Thesis Report for AE5722

by

Pratheek Ranjan Mitra

to obtain the degree of **Master of Science in Aerospace Engineering**
at the **Delft University of Technology**,
to be defended publicly on **Friday, 29th August 2025** at **9:30 AM**.

| | | |
|---|---|---|
| Student Number: | 5905508 | |
| Project Duration: | 1st January 2025 – 31st July 2025 | |
| Supervisory Committee: | Dr. Vahid Yaghoubi Nasrabadi, | Delft University of Technology |
| | Dr. Mojtaba Raouf, | Leiden University |
| | Prof. Bernard Foing, | ILEWG LUNEX EuroMoonMars |

| | |
|---|---|
| Cover: | Artistic rendering of the EMEC-1 CubeSat, with background image retrieved from: https://malteullrich.gumroad.com/l/mmfuz |
| Style: | Delft University of Technology report style, with modifications by Daan Zwaneveld |

An electronic version of this thesis is available at `https://repository.tudelft.nl`.

TU Delft

EURO MOON MARS

# Acknowledgements

*I wish to express my gratitude to Prof. Bernard Foing for providing me with the incredible opportunity to pursue this project as part of my thesis. I am also grateful to Dr. Mojtaba Raouf and Dr. Vahid Yaghoubi Nasrabadi for their valuable guidance throughout this project. Finally, I would like to thank my fellow team members Panin Ananwatanyoo, Ulrich Ny Aina N'Tchougan Sonou, and Alex Riñon Pacheco for their contributions.*

*My work would not have been possible without the support of a few external companies. I appreciate the timely responses of EnduroSat and AAC Clyde Space in providing datasheets of the various CubeSat subsystem components I requested. I also credit Exolaunch for showing me an in-person demonstration of their CubeSat dispenser and their willingness to clarify numerous doubts I had. Lastly, I am grateful to MTB3D for their assistance in 3D printing certain components for a mock-up model.*

*As someone with an interest in working on projects at the intersection of mechanical engineering and space engineering, this project allowed me to further enhance my existing knowledge of CubeSats. By equipping me with a variety of both technical and soft skills, this project has proved to be a stepping stone for my future endeavours as an aerospace engineer.*

*Pratheek Ranjan Mitra*
*Delft, August 2025*

# Contents

# List of Figures

# List of Tables

# Nomenclature

## Abbreviations

| Abbreviation | Definition |
|---|---|
| AOCS | Attitude and Orbit Control Subsystem |
| CAD | Computer-Aided Design |
| CDHS | Command and Data Handling Subsystem |
| CDS | CubeSat Design Specifications |
| CG | Center of Gravity |
| CNC | Computer Numerical Control |
| COTS | Commercial-Off-The-Shelf |
| EMEC | Earth Moon Education CubeSats |
| EPS | Electrical Power Subsystem |
| FE | Finite Element |
| GNSS | Global Navigation Satellite System |
| ISS | International Space Station |
| MDOF | Multiple Degree of Freedom |
| MOI | Moment of Inertia |
| MPC | Multipoint Constraint |
| MPE | Maximum Predicted Environment |
| NDA | Non-Disclosure Agreement |
| PCB | Printed Circuit Board |
| PSD | Power Spectral Density |
| SDOF | Single Degree of Freedom |
| SRS | Shock Response Spectrum |
| TCS | Thermal Control Subsystem |
| TTCS | Telemetry, Tracking, and Command Subsystem |

## Symbols

| Symbol | Definition | Unit |
|---|---|---|
| $E$ | Young's modulus of elasticity | [GPa] |
| $\alpha$ | Coefficient of thermal expansion | [1/K] |
| $\mu$ | Coefficient of static friction | - |
| $\nu$ | Poisson's ratio | - |
| $\rho$ | Density | [kg/m$^3$] |
| $\sigma$ | Stress | [MPa] |
| $\zeta$ | Damping ratio | - |

# Abstract

Hyperspectral imaging has a variety of commercially important applications in Earth observation because of its advanced functionalities that enable precise material identification. This thesis presents the structural design and analysis of a 3U CubeSat carrying a hyperspectral imaging payload, as part of the Earth Moon Education CubeSats mission by EuroMoonMars. Due to its high resource demands, hyperspectral imaging requires an efficient design of the structural subsystem to accommodate the payload and other subsystem components, but publicly available research on this is extremely limited. A CAD model of the complete CubeSat was designed in Autodesk Fusion based on the mass, protrusion, and CG requirements from the dispenser. The design satisfied these requirements, and the total mass of the CubeSat was 6.482 kg after accounting for margins. Structural FE analyses were performed using ANSYS Workbench to ensure that the CubeSat withstands the vibrational loads (quasi-static loads, random vibrations, and shock loads) from the launch vehicle and the thermoelastic response from the thermal loads (full load and idle load cases) in orbit. After simplifying the geometry of the CAD model to reduce the computational effort, and applying appropriate loads and constraints, the analyses were run on a multi-core processor. The first natural frequency of the CubeSat was 822.69 Hz, which was above the minimum requirement of 115 Hz, indicating that resonance was unlikely. The margins of safety for the quasi-static loads, random vibrations, and shock loads were 9.95, 3.09, and 0.13, respectively. The margins of safety for the full load and idle load cases were 2.06 and 0.83, respectively. Based on these preliminary results that showed positive margins of safety against yielding, it was concluded that the CubeSat withstands these loads. Sensitivity analyses on uncertain parameters were conducted in optiSLang, and the results of these will be used for validating and updating the FE analyses, to be carried out in the next phase of the mission by testing a physical model of the CubeSat in dedicated setups.

# 1

# Introduction

## 1.1. Satellites Overview

A satellite, more specifically, an artificial satellite, is defined as an object that is placed in orbit around a much larger celestial body. Satellites were initially developed as an outcome of geopolitical competition, and the first satellite was Sputnik 1, launched by the Soviet Union during the height of the Cold War in 1957. The USA followed suit a year later by launching Explorer 1, thus beginning the Space Race between the two nations. Other nations such as France, Japan, China, the UK, and India also launched their own satellites over the next decade. These early satellite designs were constrained to low mass and volume primarily due to the maximum payload capacities of the launch vehicles available at that time. However, an improvement in launch system technologies from 1970 to 1996 enabled the mass of satellites to grow and made them capable of performing more complex operations [1].

During the late 1990s, breakthroughs in microelectronics, as a direct consequence of Moore's Law, allowed for miniaturisation in the sensors and actuators used for satellites, along with an increase in solar cell efficiency and battery energy density. This, coupled with the ability to quickly and cheaply manufacture high-quality custom PCBs, enabled small satellites to once again come into the limelight to challenge the paradigm of traditionally large and expensive satellites [1]. Although there is no universally agreed-upon formal definition of how satellites are classified on the basis of mass, Table 1.1 depicts one such classification with a decimal prefix system at its base. Small satellites typically have a mass of less than 500 kg, along with various sub-classifications.

**Table 1.1:** Classification of satellites based on mass [2]

| Type | Wet mass [kg] | Mission cost [USD] |
|---|---|---|
| Large satellite | > 1000 | 0.1 B – 2 B |
| Medium satellite | 500 – 1000 | 50 M – 100 M |
| Small satellite | < 500 | < 50 M |
| *Minisatellite* | 100 – 500 | 10 M – 50 M |
| *Microsatellite* | 10 – 100 | 2 M – 10 M |
| *Nanosatellite* | 1 – 10 | 0.2 M – 2 M |
| *Picosatellite* | 0.1 – 1 | 20 k – 200 k |
| *Femtosatellite* | 0.001 – 0.1 | 3 k – 20 k |

At the time of defending this thesis, there are approximately 13,000 active satellites orbiting the Earth [3] and a few more orbiting other celestial bodies such as the Moon and Mars. Each of these satellites serves a particular application, depending on its payload, the most common ones being [4]:

- **Earth observation:** These satellites monitor or survey the Earth through a process called remote sensing. The data from these satellites is used for cartography, environmental monitoring, meteorology, and defence. E.g.: Copernicus Sentinel satellites.

- **Communication:** These satellites relay and amplify radio telecommunication signals via a transponder and, by doing so, create a communication channel between a source transmitter and a receiver at different locations on the Earth. E.g.: Starlink satellites.
- **Navigation:** These satellites transmit radio time signals and enable stationary or mobile receivers on the Earth to determine their exact location in real-time to accuracies on the order of a few meters. E.g.: GNSS satellites such as GPS and Galileo.
- **Astronomy:** These satellites are used to observe distant stars, planets, galaxies, and other outer space objects, free from light pollution and the scattering effects of the Earth's atmosphere. E.g.: Hubble Space Telescope.

The form factors of these satellites can also be vastly different from each other, depending on their ease of construction and the organisation of internal and external components. As a result, most conventional satellites come in rectangular, cylindrical, or even completely irregular shapes.

## 1.2. CubeSat Standard

CubeSats are a special type of small satellite having a standardised form factor. They were initially developed in 1999 through a collaboration between California Polytechnic State University and Stanford University to provide a platform for education and space exploration. As shown in Figure 1.1, the standard CubeSat size uses a 'one unit' or '1U', measuring approximately 100 mm × 100 mm × 100 mm and having a mass of not more than 2 kg. These can then be stacked in numerous combinations to create larger configurations, each generally referred to by the number of units they comprise, such as 2U, 3U, 6U, and so on. It should be noted that CubeSats fall into both the nanosatellite and microsatellite categories, as their masses cover a wide range depending on the number of units present [5].

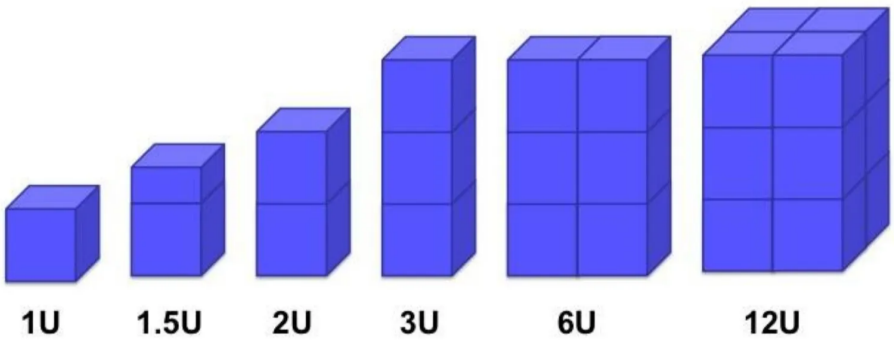


**Figure 1.1:** CubeSat sizes [5]

The CubeSat standard, along with the extensive usage of COTS components, has drastically reduced space mission costs and development times, thus making a satellite launch feasible for small companies, research institutes, and universities. Hence, CubeSats are increasingly being used for technology demonstration, scientific studies, and even commercial purposes, not just within Earth orbit, but also to the Moon and beyond. Since the launch of the first CubeSats in 2003, more than 2,500 of them have been launched into space at the time of defending this thesis, and this number is projected to increase by 1,000 over the next five years [6].

It is interesting to note that 3U is the most popular size, with around 1,500 launches, followed by 6U and 1U, with around 370 and 330 launches, respectively [6]. This is because the 3U form factor provides sufficient space for accommodating both the mission payloads and their associated subsystems, without becoming too heavy or complex.

## 1.3. Hyperspectral Imaging Mission

EuroMoonMars is a collaborative initiative between space agencies, industries, and universities that involves research efforts towards the colonisation of the Moon and the eventual colonisation of Mars. It comprises field campaigns in lunar or Martian analogue environments, regular workshops to stimulate knowledge exchange in space science, and international projects within the space sector [7][8]. One such project from EuroMoonMars is the Earth Moon Education CubeSats (EMEC) mission, which aims to develop 3U CubeSats for remote sensing of the Earth and the Moon, and is jointly undertaken by Leiden University, Inholland University of Applied Sciences, and Delft University of Technology. The mission is a technology demonstration whose objectives include monitoring spectral signatures of the Earth's vegetation and analysing the composition of regolith on the Moon's surface. By identifying valuable resources within the regolith, such as water-ice and hydrogen, the data from this mission serves to aid in planning future sample return missions [9][10].

The mission is split into two phases, each of which uses a 3U CubeSat. The first phase, EMEC-1, involves a CubeSat operating in Earth orbit, while the second phase, EMEC-2, involves a CubeSat equipped with wheels to function as a rover and is brought to the Moon by a lander [9][10]. The scope of this thesis is focused on the structural design and analysis of the 3U CubeSat for EMEC-1. This CubeSat would be in a circular sun-synchronous orbit having an altitude of 800 km, an inclination of 98°, and a longitude of ascending node of 99.24°. The nominal mission duration is two years, and the CubeSat's data transmission will be managed through the McMurdo ground station in Antarctica, with an access time of three hours per day.

At the core of this CubeSat is a hyperspectral imaging payload, which is the most advanced among the three methods of optical remote sensing, as shown in Figure 1.2. RGB imaging payloads capture data in three broad spectral bands, which are red, green, and blue, thus mimicking human vision. Multispectral imaging payloads capture data from near-infrared wavelengths in addition to RGB and typically span 5 to 20 discrete spectral bands. Hyperspectral imaging payloads go a step further and capture hundreds of narrow spectral bands across the visible to near-infrared spectrum [11].

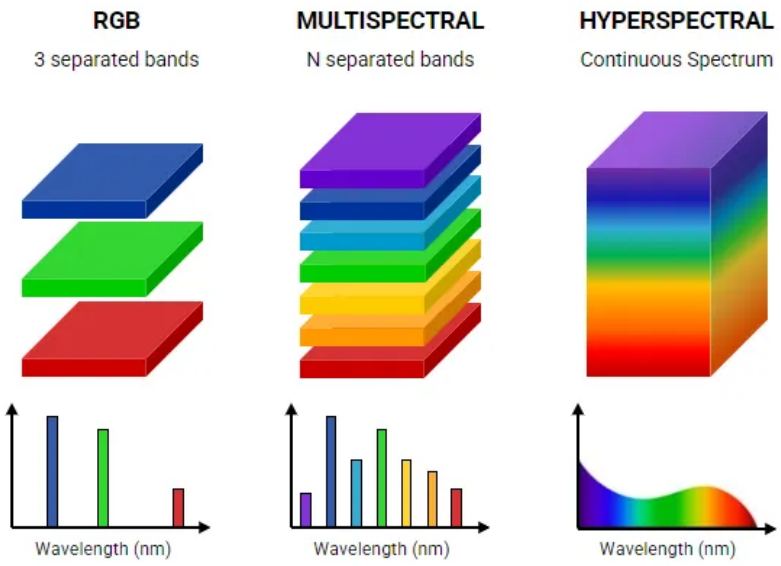


**Figure 1.2:** RGB, multispectral, and hyperspectral imaging [12]

The collected data forms a hyperspectral data cube as shown in Figure 1.3, in which two dimensions represent the spatial extent of the image, and the third is its spectral content. Due to the almost continuous spectral sampling for each pixel in an image, hyperspectral imaging payloads enable precise material identification, which is valuable in agriculture, mineralogy, and oceanography [11]. These payloads were initially used aboard aircraft in the 1980s, and the first spaceborne mission for hyperspectral imaging was the EO-1 satellite, launched in 2000 [13]. In recent years, many New Space

companies such as Pixxel [14] and Wyvern [15] have emerged, and they are currently developing small satellites carrying hyperspectral imaging payloads to commercialise the generated datasets.

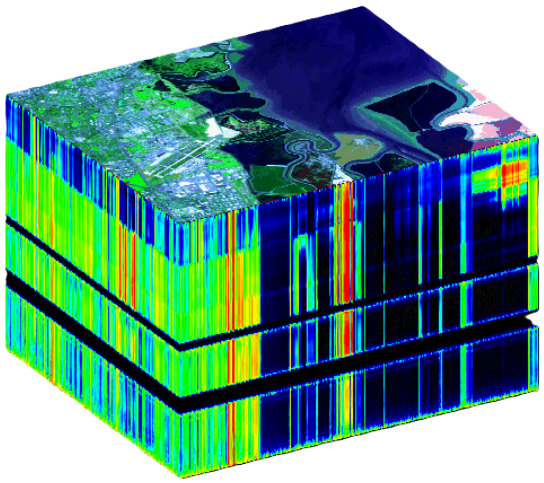

**Figure 1.3:** Hyperspectral data cube with pseudo colours [16]

Unsurprisingly, hyperspectral imaging payloads have presented a unique set of challenges in satellites, which are even more relevant in the case of the much smaller CubeSats. One of these is the complex data processing and downlink demands, as a raw data cube can be hundreds of megabytes. Secondly, a high pointing stability is required during imaging to ensure the quality of acquired data is not compromised. Thirdly, efficient power and thermal management systems are necessary because of mass and volume constraints [17].

## 1.4. Thesis Outline

Chapter 1, the current chapter, begins with a brief overview of satellites and CubeSats in general. The purpose of the mission and the working of hyperspectral imaging are then introduced.

Chapter 2 provides the state-of-the-art in the realm of CubeSat structures as well as the various drivers, such as the dispenser, the launch vehicle, the space environment, and the bus subsystems, that influence structural design. It ends with a summary of previous theses on educational CubeSats.

Chapter 3 presents the main research question of the thesis along with a few sub-questions. It also lists a plan of research activities that need to be carried out to answer the research questions.

Chapter 4 explains the design of the CAD model of the complete CubeSat, consisting of the payload, the primary structure, and the selected bus subsystem components, based on the requirements from the dispenser.

Chapter 5, perhaps the most important chapter, describes the vibrational analyses of the CubeSat based on the launch vehicle loads. It includes sensitivity analyses to study how the results are influenced by the uncertainty of a few input parameters, along with a calibration methodology using synthetic experimental data.

Chapter 6 describes thermoelastic analyses of the CubeSat using the temperature results obtained from thermal analyses of two load cases during orbit.

Chapters 7 and 8 showcase the conclusions of the research and the recommendations for future work, respectively. Finally, appendices containing important information supporting the main chapters are provided at the end.

# 2

# State-Of-The-Art

## 2.1. External Drivers of CubeSat Structural Design

### 2.1.1. Dispenser

The dispenser (also known as deployer) shown in Figure 2.1 is a container-based integration system which serves as the mechanical and electrical interface between the CubeSat and the launch vehicle. This is unlike the case of conventional satellites, which are directly connected to the launch vehicle by means of separation systems. As the CubeSat follows a standardised form factor, dispensers have also been standardised to specific dimensions and can store single or multiple CubeSats, depending on their size. Once the launch vehicle sends the deployment signal to the dispenser, an actuation mechanism opens the door, and a spring-loaded backplate pushes the CubeSats out of the launch vehicle. Although deployment from a launch vehicle is the most followed approach, some dispensers are transported to the ISS and attached to a module on its exterior, which then deploys CubeSats stored within it. Dispensers are designed with two types of mechanical constraint systems, namely, rails or tabs [18].

**Figure 2.1:** Latest version of the P-POD [19]

A rail-type dispenser supports CubeSats having rails running along their four parallel edges. These rails slide along the guide rails inside the dispenser once the door opens. For most of these dispensers, there exists a thin gap between the dispenser's guide rails and the CubeSat rails. As a result, the CubeSat can shift its position slightly within the dispenser, and this creates a 'floating' non-linear boundary condition which is difficult to model exactly in a structural FE analysis. Despite this shortcoming, rail-type dispensers are the most widely manufactured configuration [20].

A tab-type dispenser supports CubeSats with tabs which run along any of its two parallel edges. These tabs are gripped by clamps in the dispenser and are released only when the door opens. As shown in Figure 2.2, this dispenser provides a fixed boundary condition at the CubeSat tabs, which can be easily applied in a structural FE analysis, unlike the rail-type dispenser [20].

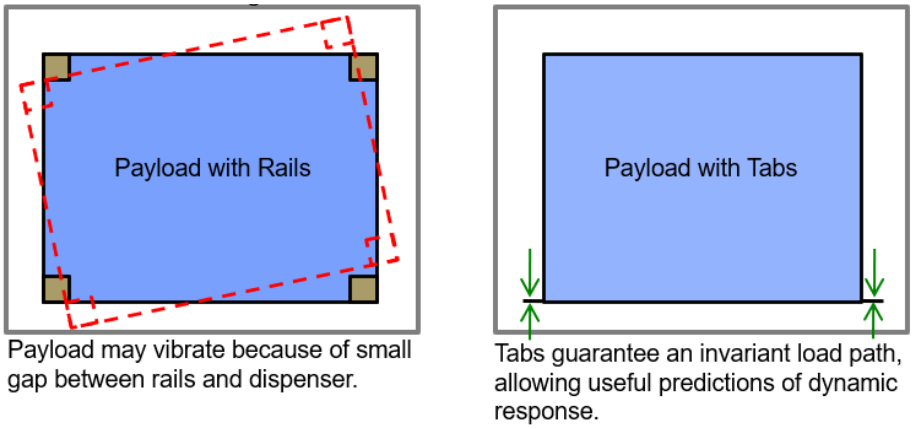


**Figure 2.2:** Rail-type and tab-type dispensers [21]

The Poly Picosatellite Orbital Deployer (P-POD), developed when the CubeSat standard was first introduced, is one of the most well-known dispensers and has extensive flight heritage. Apart from the P-POD, there are New Space companies that have developed their own dispensers, as shown in Table 2.1, capable of accommodating various sizes of CubeSats. In order to keep up with the increasing demand for launching CubeSats, larger dispensers were developed which could deploy more CubeSats at a time. Some of these dispensers have innovative features to stand out and remain competitive, such as extra volume within them for additional CubeSat components, or better isolation from the launch vehicle loads, among others.

**Table 2.1:** Partial list of dispensers

| Name | Launch platform | Constraint system | CubeSat sizes | Reference |
|---|---|---|---|---|
| ASTROFEIN PSL | Rocket | Rails | 1U, 2U, 3U, 6U, 12U | [22] |
| Cal Poly P-POD | Rocket | Rails | 1U, 2U, 3U | [19] |
| Dhruva Space DSOD | Rocket | Rails | 1U, 2U, 3U, 6U, 12U | [23] |
| Exolaunch EXOpod Nova | Rocket | Rails | 1U, 2U, 3U, 4U, 6U, 8U, 12U, 16U | [24] |
| ISISPACE DuoPack | Rocket | Rails | 1U, 2U, 3U, 6U | [25] |
| JAXA J-SSOD | ISS | Rails | 1U, 2U, 3U, 6U | [26] |
| Rocket Lab CSD | Rocket | Tabs | 1U, 3U, 6U, 12U | [21] |
| Voyager NRCSD | ISS | Rails | 1U, 2U, 3U, 4U | [27] |

While CubeSat developers can generally decide whether to utilise rails or tabs, the choice of the actual dispenser always lies in the hands of the launch vehicle provider, as they would have already

determined which dispensers can be integrated on their launch vehicle. Furthermore, there are launch broker companies that have contracts with specific launch vehicle providers and dispenser manufacturers to coordinate all CubeSat launch opportunities. As each dispenser provides slightly different requirements, it is beneficial for the CubeSat to be designed for as wide a range of dispensers as possible to maximise launch opportunities [20].

### 2.1.2. Launch Vehicle

The launch vehicle market involves a mix of traditional companies such as United Launch Alliance (Atlas V and Vulcan Centaur) and Arianespace (Ariane 6 and Vega-C), as well as New Space companies such as SpaceX (Falcon 9 and Falcon Heavy) and Rocket Lab (Electron), and has emerged as a popular means to launch small satellites, including CubeSats. Moreover, many other companies, such as ISAR Aerospace, Rocket Factory Augsburg, PLD Space, Orbex, Firefly Aerospace, and Skyroot Aerospace, to name a few, are currently developing their launch vehicles, which are likely to become fully operational in the near future [28]. Each launch vehicle provider aims to showcase the lowest cost per kg to the satellite developer and hence utilise various techniques such as reusability of stages, low-cost manufacturing, and novel propulsion systems. As shown in Figure 2.3, small satellites usually adopt one of three different approaches to launch, which are dedicated, piggyback, and rideshare.

A dedicated launch involves the satellite becoming the primary payload of the launch vehicle. By doing so, the satellite developer has total control over all the launch parameters, such as launch date, specific orbit, and precisely timed trajectories. Furthermore, they have a readiness 'go/no-go' call on launch day in case of any anomalies with their satellite prior to launch. A major disadvantage of a dedicated launch is that it is much more expensive compared to other launch options [20].

A piggyback launch is possible when a launch vehicle can fit small satellites within its excess mass and volume margins. For secondary payloads that piggyback onto a larger primary payload, the launch parameters are always determined by the primary payload, and the developers of the secondary payloads have no choice but to accept what is available [20]. NASA's CubeSat Launch Initiative [29] and ESA's Fly Your Satellite [30] are two programs that provide piggyback launches to CubeSats developed by university students.

A rideshare launch is where multiple small satellites are deployed from a single launch vehicle. The orbits of all these satellites are quite similar, but they may be deployed at different altitudes [20]. Since their commencement in 2021, the Transporter missions of Falcon 9 are one of the most well-known rideshare programs and have deployed more than 1,000 satellites over the course of 14 launches [31].

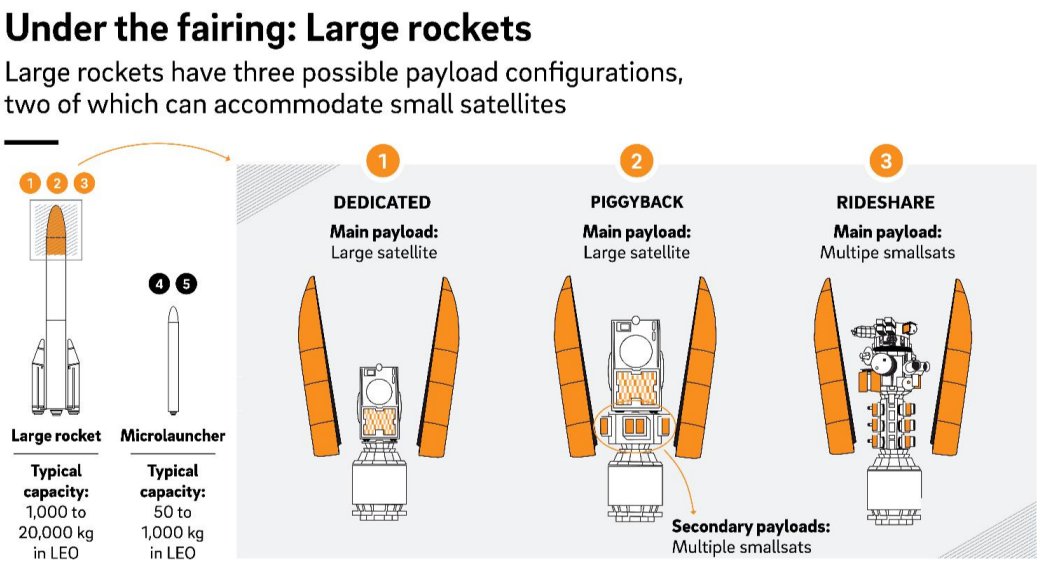


**(a)** Large rockets

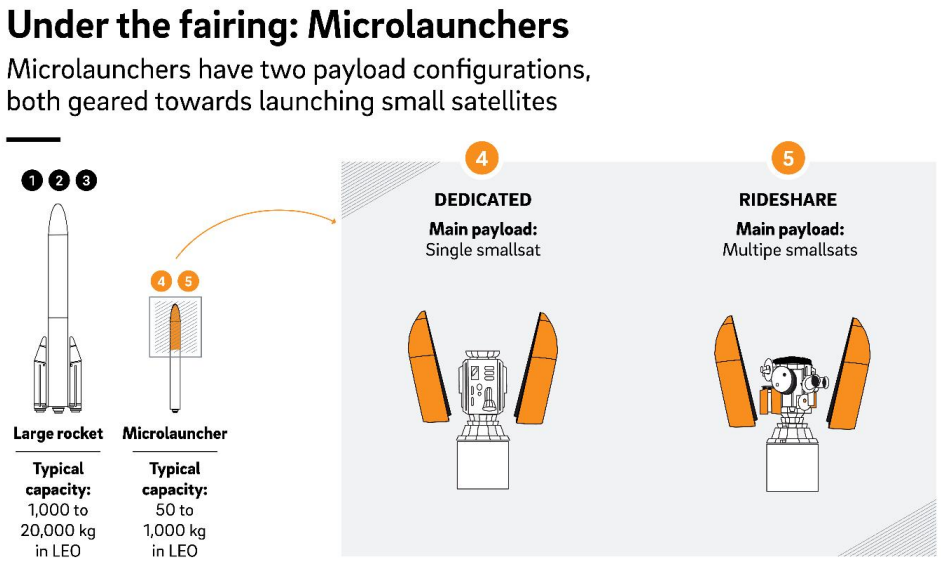


**(b)** Microlaunchers

**Figure 2.3:** Small satellite launch approaches [32]

The main drivers behind launch vehicle selection for CubeSat missions are the cost per kg launched, the availability of desired orbits, the frequency of launches, and the types of CubeSat dispensers that serve the chosen launch vehicle. This is a complex process involving various stakeholders of the mission, and the major decision points are summarised in Figure 2.4. The structural design of the CubeSat is also directly influenced by the launch vehicle, as the CubeSat within the dispenser must withstand the mechanical loads specified as the MPE during the launch phase [33]. The magnitudes of these loads can differ significantly among different launch vehicles, but until the exact one is finalised, a few potential vehicles can be compared so that the most conservative values are used in structural FE analyses and hardware testing.

Irrespective of the particular launch vehicle chosen eventually, the loads experienced can be classified into five major types [34][35]:

- **Quasi-static loads:** These are caused by the engine thrust and trajectory manoeuvres during launch. They are specified as load factors in $g$, and scale with the mass of the system. The quasi-static assumption arises from the fact that these loads change slowly with time, so the dynamic response of the structure is not significant. As a result, they are treated as steady-state accelerations acting on the CG of the CubeSat.
- **Sinusoidal vibrations:** These are low-frequency vibrations (up to 100 Hz) caused by the combustion within the engines, especially the POGO effect. In this phenomenon, combustion instability causes variations in engine thrust, which causes oscillations in the acceleration of the launch vehicle structure, which in turn affects the propellant pressure and flow rate, thus causing the cycle to repeat. These vibrations are specified as an acceleration amplitude, in $g$ versus frequency.
- **Random vibrations:** These vibrations (up to 2,000 Hz) are due to unsteady aerodynamic phenomena in the atmosphere, such as shock waves and boundary layer turbulence along the sides of the launch vehicle. Unlike the other load types, they are not deterministic and are defined in terms of a probabilistic distribution. These vibrations are specified as an acceleration Power Spectral Density (PSD), in $g^2$/Hz versus frequency.
- **Acoustic loads:** These are due to the exhaust noise of the engines and are predominant during lift-off and transonic flight. They are defined as a sound pressure level, in dB versus frequency, and are assumed to be a diffuse sound field, where the intensity of the sound is the same in all directions. These loads are of particular importance when there are large panel-like structures, as the pressure waves can impinge on them and produce a significant response.

- **Shock loads:** These are short-duration and high-frequency transient vibrations (up to 10,000 Hz) that occur due to the separation of launch vehicle stages, the jettisoning of the fairing, and sometimes also during deployment from the dispenser. They are defined as an acceleration Shock Response Spectrum (SRS), in $g$ versus frequency.

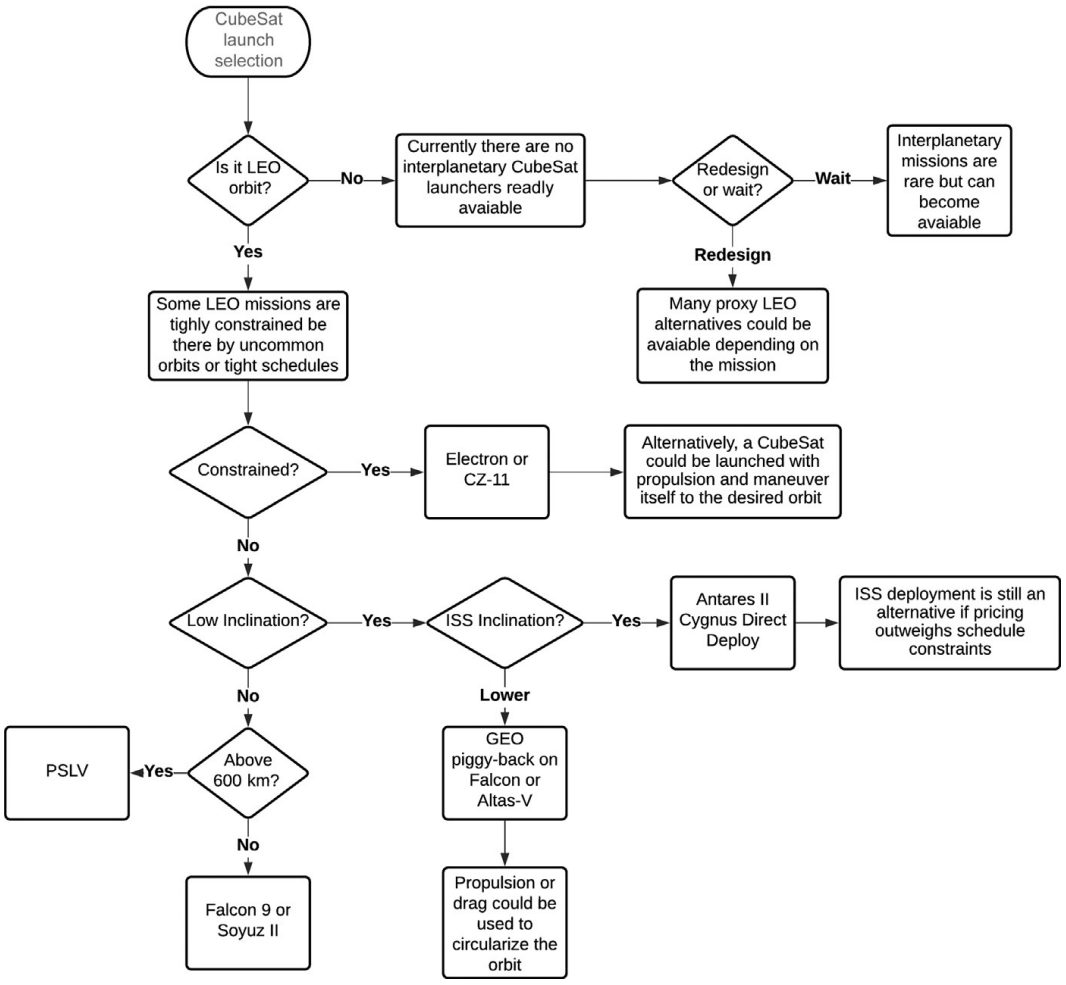


**Figure 2.4:** Launch vehicle selection flowchart [33]

### 2.1.3. Space Environment

While the CubeSat endures the launch vehicle loads only for a few hours, it will spend the majority of its lifetime in the harsh environment of space. This necessitates appropriate design choices to ensure that the CubeSat can remain operational in these conditions.

The CubeSat experiences thermal loads from various sources, such as solar radiation, albedo from the Earth, infrared radiation from the Earth, and also the heat dissipated from its electronic components [36]. Each of these loads varies depending on the orbital position of the CubeSat and its mode of operation. As a result, there are significant variations in the temperatures of components, which can damage them if they exceed their permissible limits. Moreover, expansions and contractions of the structure can cause thermal fatigue and also misalign the imaging payload, affecting the quality of the data captured. Efficient thermal management can stabilise the temperature variations under these transient loads, while the materials of the structure should be carefully selected based on their thermoelastic properties [37].

The vacuum of space can cause outgassing, which is the release of gases from a material. This can be due to the release of absorbed gases from the bulk of the material, adsorbed gases from the surface of the material, or evaporation of the material itself. These outgassed molecules pose a particular threat

when they condense onto the surfaces of optical components within an imaging payload and cause irreversible contamination. Hence, there is a restriction on the choice of materials that can be used in order to minimise the occurrence of outgassing in space. Prior to launch, the CubeSat will be placed in a thermal vacuum chamber for a bake-out test to check whether the volume of outgassed materials is sufficiently low [37].

Material selection is also constrained by the effects of degradation from ultraviolet radiation and atomic oxygen. Ultraviolet radiation worsens the mechanical properties of polymers through the mechanisms of cross-linking and chain scission, but does not affect metals or ceramics. Atomic oxygen is produced when ultraviolet radiation reacts with molecular oxygen in the upper atmosphere. This oxidises certain metals and polymers depending on their reactivity, characterised by a parameter known as erosion yield. Ceramics, along with metals such as aluminium, and polymers such as Teflon, are unaffected by atomic oxygen due to their low erosion yields [37].

## 2.2. Internal Drivers of CubeSat Structural Design

Similar to conventional satellites, CubeSats also consist of a number of bus subsystems that support the operation of the payload. The functions of the payload and each subsystem, along with an explanation of their possible influence on the structural design, are mentioned below [38]:

- **Payload:** This is perhaps the most important component of the CubeSat due to its role in carrying out the primary tasks of the mission. The requirements on the structure are not limited to dimensions compatibility with the payload, but are also dictated by the payload functions. In the case of an imaging payload, it should be accommodated in such a way that its aperture has access to the exterior of the CubeSat. As the payload works in tandem with the bus subsystems, it is not surprising that certain requirements overlap between them, such as withstanding the space environment or the launch vehicle loads.
- **AOCS:** This subsystem estimates and controls the attitude and orbital states of the CubeSat. It utilises hardware such as sensors (sun sensors, magnetometers, and GNSS receivers) and actuators (reaction wheels, magnetorquers, and thrusters), along with software supporting various algorithms. To ensure the proper functioning of this subsystem, structural designers must take into account the mass distribution of the CubeSat as it affects the CG and the inertia tensor relative to this point. Moreover, the use of deployment mechanisms should be carefully analysed, as these systems can cause torques during on-orbit operations.
- **EPS:** This subsystem provides the CubeSat with the necessary electrical power by collecting, storing, and distributing it through various hardware. The power generated by the solar panels is dependent on the size of the solar panels, the packing factor of their cells, and the choice of body-mounted or deployable solar panels. Battery selection also affects the total mass of the CubeSat. The power distribution systems are simplified in CubeSats due to standardised connectors that minimise the need for cables. PCBs can be stacked one on top of another (PC104 standard) or inserted into one common board that acts as an integrated backplane connector.
- **TTCS:** This subsystem, together with the ground station, enables the uplink of commands to the CubeSat and the downlink of payload data from the CubeSat. A tracking signal is also continuously sent from the CubeSat to the ground station, which contains critical data about the health of the CubeSat. As antenna dimensions are correlated with the wavelength and hence, the frequency, CubeSats make use of deployable antennae that can be stowed within the structure or patch antennae that are flat and compact. Another aspect that should be taken into account is the antenna radiation pattern, which depends on where it is placed on the structure.
- **TCS:** This subsystem ensures that the temperatures of all components are within their required limits. It is also responsible for minimising temperature gradients across the CubeSat, especially in optical components within an imaging payload. Due to the vacuum of space, heat transfer mainly occurs through conduction and radiation. Depending on whether they require an energy input or not, thermal control methods are of two types, which are passive (surface coatings and radiators) and active (heaters and coolers). The effectiveness of this subsystem is determined by the positions of other components within the CubeSat, as this affects thermal resistances.
- **CDHS:** There are several modes of operation for the CubeSat, such as idle mode, detumbling

mode, imaging mode, sun-pointing mode, downlinking mode, as well as a safe mode for emergencies. This subsystem provides internal communication and control capabilities needed for the CubeSat to execute a particular mode of operation, either autonomously or controlled by the ground station. It often interfaces directly with the payload and provides data processing and mass storage functionalities.

## 2.3. Design Methodologies

### 2.3.1. CubeSat Design Specifications

To aid developers in designing their CubeSats such that they will be compatible with dispensers, launch vehicles, and the space environment, the CDS document provides a variety of baseline requirements [39]. After all, it is the responsibility of the developers to ensure the safety and success of their CubeSat missions by implementing good engineering practices. In the scope of the present work, the mechanical specifications of a 3U CubeSat are of particular importance, such as:

- The CubeSat shall use the coordinate system with the origin at its geometric centre as defined in Figure 2.5 and conform to the physical dimensions.
- No components on the yellow shaded sides shall protrude farther than 6.5 mm normal to the surface from the plane of the rail.
- Rails shall have a minimum width of 8.5 mm measured from the edge of the rail to the first protrusion on each face, that is, the maximum width of these protrusions shall be 83 mm.
- Extra cylindrical volume of diameter 64 mm and length 36 mm, also referred to as the ‘tuna-can volume’, may be available for the CubeSat, as shown in Figure 2.6.
- The CubeSat shall have a maximum mass of 6 kg.
- The CubeSat CG shall fall within the following ranges as measured from its geometric centre: ±20 mm for the $X$ axis, ±20 mm for the $Y$ axis, and ±70 mm for the $Z$ axis.
- The CubeSat structure should be made from aluminium alloy, typically 7075, 6061, 6082, 5005, and/or 5052. Any aluminium on external surfaces, such as rails and standoffs that are in contact with the dispenser rails, shall be hard anodised to prevent any cold welding within the dispenser.
- If a CubeSat shares a dispenser with another CubeSat(s), each CubeSat shall employ a mechanism to encourage separation from neighbouring CubeSats within the dispenser.
- Deployables shall be constrained by the CubeSat, not the dispenser.

The second to fifth specifications will need to be discussed with the specific dispenser provider, as some of them are more lenient by permitting higher CubeSat masses, and larger protrusions or tuna-can dimensions for their dispenser. The document also defines a number of electrical and operational specifications, including, but not limited to, requirements regarding propulsion systems, battery protection circuitry, radio frequency transmissions, and limitation of space debris.

### 2.3.2. Trends in CubeSat Structural Design

CubeSat structures are classified into primary and secondary structures depending on their function. The primary structures transmit the launch vehicle loads through the CubeSat from the dispenser interface and also serve as the mechanical interface with the payload and the bus subsystems. The failure of the primary structure affects the overall structural integrity of the CubeSat. Secondary structures are appendages whose only function is to support themselves, and while their failure could still have significant effects on the mission, it does not necessarily result in a catastrophic event, as in the case of a primary structure failure. The CubeSat frame or chassis is a primary structure, while deployable solar panels and antennae are secondary structures [38][40].

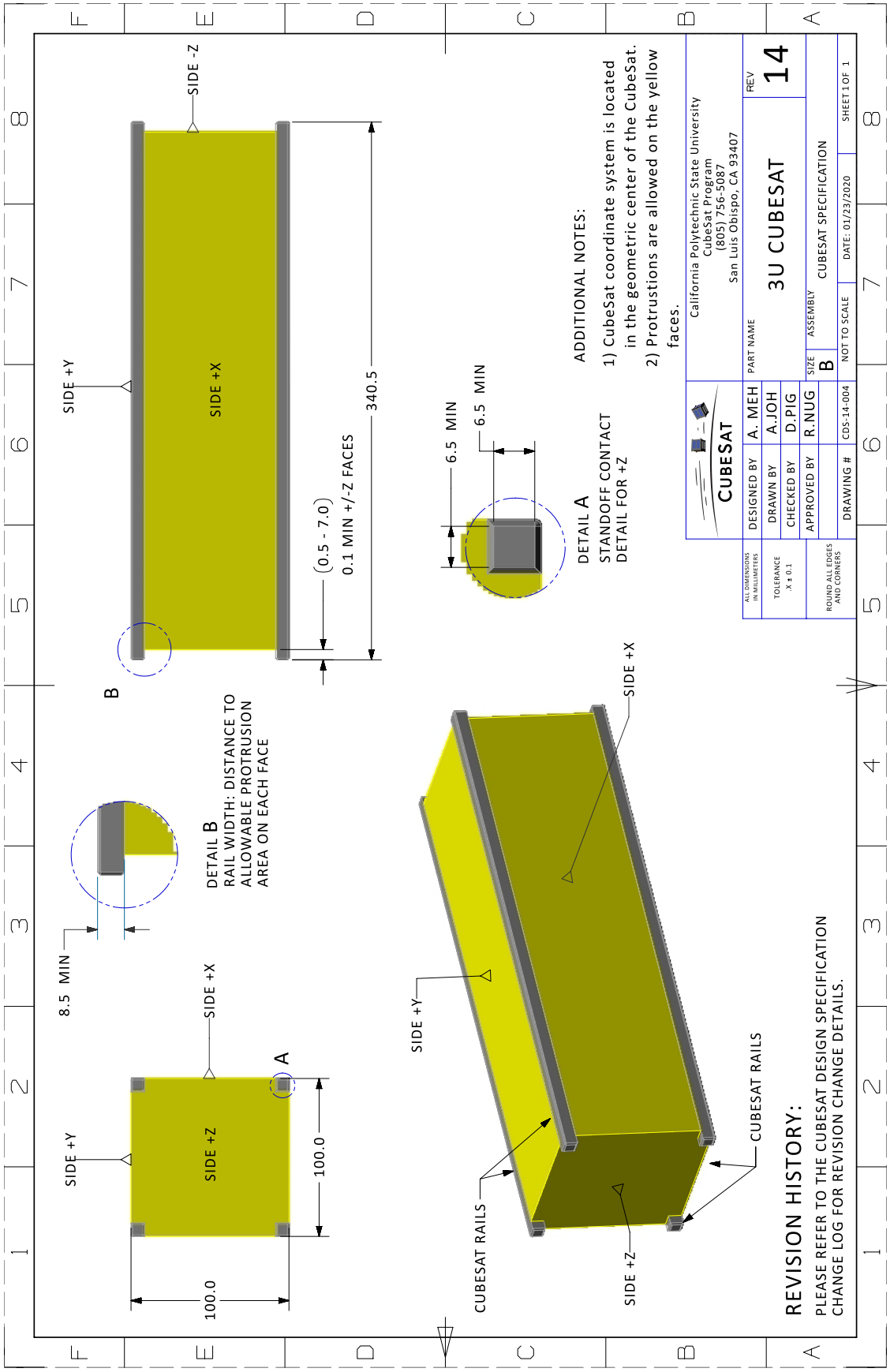


**Figure 2.5:** 3U CubeSat physical dimensions [39]

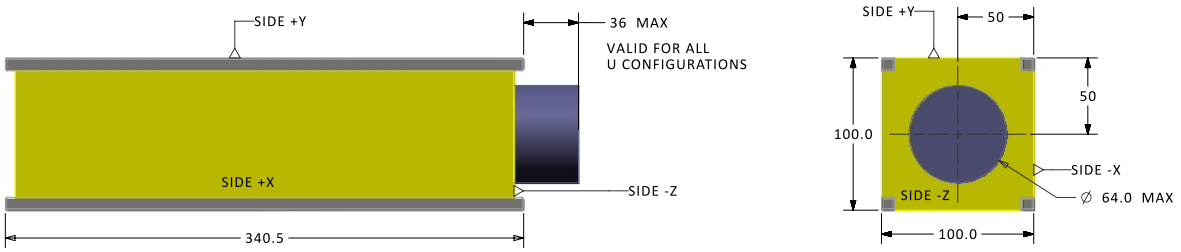


**Figure 2.6:** 3U CubeSat extra volume [39]

The primary structure can be constructed from one of two different design methodologies, which are monocoque or modular. Monocoque structures consist of load-bearing skins similar to those used on aircraft. The main intent of this structure is to maximise internal volume and provide more mounting points for components. Despite these structures being heavier, they have more thermal mass, which allows for better thermal control. Modular structures allow for a flexible internal design for urgent missions while still ensuring strict adherence to the physical dimensions of the CubeSat standard. These allow better accessibility of internal components as they tend to require the de-integration of fewer fasteners on average, compared to monocoque structures. As they are lighter, they allow for more mass to be used by the components of other subsystems. Although COTS monocoque structures were popularly used in early CubeSat designs, there has been a recent interest in modular structures, particularly due to the mass and accessibility benefits [40].

There are two possible ways to develop the CubeSat primary structure, which are either using an existing COTS structure or designing a completely new structure from scratch. For the first option, many New Space companies offer flight-certified 3U CubeSat structures, as shown in Table 2.2 and Figure 2.7. These structures can greatly shorten the development process, as they have already been tested under thermal vacuum and the launch vehicle loads, such as sinusoidal vibrations, random vibrations, and shock loads. Furthermore, many of them have flight heritage, indicating their popularity among CubeSat developers. However, these structures are quite expensive and are useful only when their designs are compatible with the payload and bus subsystems. Any attempts to modify these structures, such as drilling new attachment holes or applying coatings for thermal control, would be unwise as they risk damaging the structure [38][40].

**Table 2.2:** Partial list of COTS 3U CubeSat primary structures

| Name | Construction | Cost | Reference |
|---|---|---|---|
| 2NDSpace | Modular | EUR 3,100 | [41] |
| AAC Clyde Space | Monocoque | Unspecified | [42] |
| C3S | Monocoque | Unspecified | [43] |
| EnduroSat | Modular | EUR 4,000 | [44] |
| Gran Systems | Modular | Unspecified | [45] |
| NPC Spacemind | Modular | EUR 2,800 | [46] |
| Pumpkin Space Systems | Monocoque | USD 2,955 | [47] |
| Serenum Space | Modular | Unspecified | [48] |

The second option offers the greatest freedom in terms of customising the structure, which can be done using unique materials, creating specific mounting points, or following a certain manufacturing approach. A custom-built monocoque structure can be manufactured relatively easily using CNC machining, waterjet cutting, or laser cutting. Furthermore, the space qualification of certain materials used in additive manufacturing, such as PEEK, has allowed this technique to be used for developing CubeSat structures. The downside of these custom-built structures is that extensive knowledge of design, analysis, manufacturing, and testing from the CubeSat developer is required to ensure that nothing from the CDS document is violated [38][40].

The two most common types of internal layouts observed in CubeSats are the backplane and PC104 configurations, as shown in Figure 2.8. In the backplane configuration, there are single connection


**(a)** 2NDSpace [41] **(b)** AAC Clyde Space [42] **(c)** EnduroSat [44]

**(d)** NPC Spacemind [46] **(e)** Serenum Space [48]

**Figure 2.7:** COTS 3U CubeSat primary structures

points between PCBs and the backplane, whereas in the PC104 configuration, there are dual connection points present above and below the PCBs. Upon considering $n$ different PCBs attached to a backplane, and a similar PC104 configuration with $n$ PCBs, the backplane configuration offers better accessibility as fewer PCBs are required to be removed on average to access one particular PCB, for a typical case when $n$ is five or six. This is because PCBs can be directly removed from the backplane, whereas in the PC104 configuration, additional PCBs need to be removed on either side of the PCB which is to be accessed. However, most COTS CubeSat structures encourage a PC104 configuration due to the close size of its PCBs (95.89 mm × 90.17 mm) to the CubeSat physical dimensions, and

also because most COTS components of other subsystems are designed according to this configuration [38].

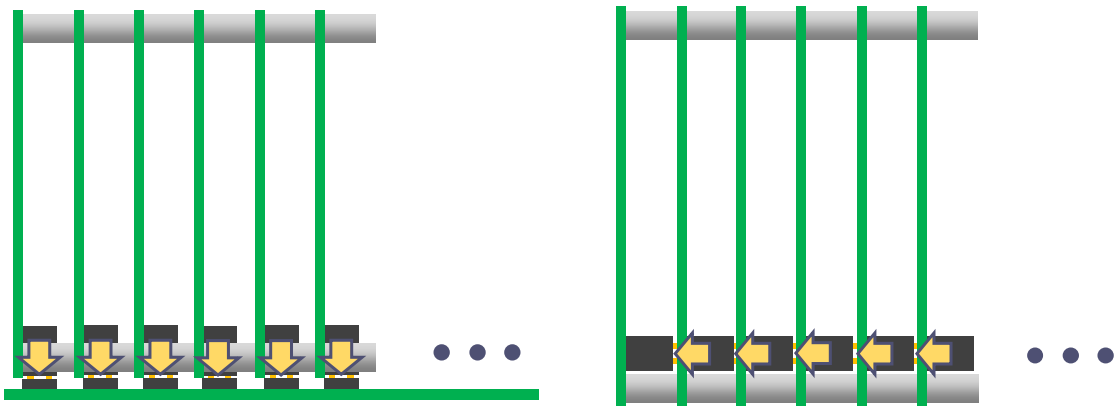

**(a)** Backplane **(b)** PC104

**Figure 2.8:** CubeSat internal layouts [49]

## 2.4. Educational CubeSats

The increase in accessibility to space has influenced a new generation of students, as they now have a chance to be involved in many aspects of the CubeSat development process, such as conceptualisation, design, manufacturing, assembly, integration, testing, and operations. As a result of this exposure, students in the past have worked extensively on the structural design and analysis of their CubeSats. Many have prepared theses on this topic as part of their bachelor and master programmes, and some of these defended within the last decade are briefly summarised in Table 2.3. There are conference papers also describing similar topics, but theses are found to be to be more comprehensive as they are written in an academic context.

Publicly available research on the structural design and analysis of CubeSats carrying hyperspectral imaging payloads for Earth observation is extremely limited, not just among educational CubeSats, but also across the general realm of CubeSats. Nevertheless, all the discussed theses followed similar methodologies, such as first developing a CAD model of the CubeSat, setting up the FE analyses by making simplifications to the model, applying appropriate loads and constraints based on the selected dispenser and launch vehicle, and finally interpreting the results. The present work intends to follow a similar reporting format and efficiently apply what has been learned from previous theses to accomplish the mission at hand.

**Table 2.3:** Past theses on CubeSat structural design and analysis

| CubeSat | Research summary | Reference |
|---|---|---|
| AlAinSat-1 | • This was a 3U CubeSat carrying two Earth observation payloads for monitoring cloud cover through images, and using radiometric readings to determine soil moisture content and ice thickness.<br>• The lowest natural frequency was 163.23 Hz, which was above the minimum allowable of 90 Hz, while quasi-static loads and random vibrations analyses showed positive margins of safety.<br>• Experimental validation was conducted using a shaker system for vibration tests on the CDHS hardware module, and the results matched within a 5% error with the simulations. | [50] |

| | | |
|---|---|---|
| MIST | • This was a 3U CubeSat carrying five technical and scientific experiments developed by university students and two companies.<br>• The lowest natural frequency was above the minimum allowable of 130 Hz for different dispenser boundary conditions, despite being highly dependent on them.<br>• The quasi-static loads and random vibrations analyses showed positive margins of safety, but certain regions of high stresses were attributed to singularities.<br>• The shock loads analysis was inconclusive due to extremely high stresses, and conducting experimental shock testing was recommended. | [51] |
| ISTsat-1 | • This was a 1U CubeSat demonstrating Automatic Dependent Surveillance-Broadcast (ADS-B) technology for tracking aircraft in flight.<br>• The lowest natural frequency was 192.41 Hz, which was above the minimum allowable of 100 Hz, while quasi-static loads and random vibrations analyses showed positive margins of safety.<br>• Thermal analyses were conducted for cold, nominal, and hot cases, and all components except the UHF antenna were within their operational temperature ranges. | [52] |
| TeideSat | • This was a 1U CubeSat intended to establish optical communication with the Earth through Light Emitting Diode (LED) technology.<br>• The rails and frames of the CubeSat structure were manufactured using CNC machining, but certain dimensional measurements were not in compliance with the requirements due to a lack of precision in the manufacturing process.<br>• The lowest natural frequency was 574.15 Hz, which was above the minimum allowable of 100 Hz, while quasi-static loads, sinusoidal vibrations, random vibrations, and shock loads analyses showed positive margins of safety. | [53] |
| SphinX-NG | • This was a 3U CubeSat capable of performing solar and extraterrestrial X-ray spectroscopy.<br>• The lowest natural frequency was 400 Hz, which was above the minimum allowable of 100 Hz, while a random vibration analysis showed positive margins of safety.<br>• As the PCB stack was simplified as a rigid body in the analyses of the complete CubeSat, standalone modal and random vibrations analyses were carried out on this stack by treating the components as flexible bodies. | [54] |
| SEAM | • This was a 3U CubeSat with sensors on deployable booms that aimed to acquire high-resolution data about the ionosphere magnetic field.<br>• The lowest natural frequency was 232.94 Hz, which was above the minimum allowable of 40 Hz, while the quasi-static loads and random vibrations analyses showed positive margins of safety.<br>• The shock loads analysis resulted in high stresses in certain regions, which were likely to cause plastic deformation.<br>• Separate detailed structural analyses were conducted on the star tracker and the boom plate assembly. | [55] |

# 3

# Research Conceptualisation

## 3.1. Research Questions

From the information in Chapter 2, it is evident that structural design and analysis are an essential part of the CubeSat development process. Hence, the following main research question is formulated:

*To what extent can the structural subsystem of an Earth observation 3U CubeSat be developed to comply with requirements from a hyperspectral imaging payload, the bus subsystems, the dispenser, the launch vehicle, and the space environment?*

In order to answer this research question and devise a proper plan of tasks, it is preferable to define a few sub-questions as follows:

- *What is an efficient arrangement of all hardware components within the 3U form factor to comply with mass and CG requirements?*
- *Which of the five types of launch vehicle loads are relevant for performing vibrational analyses on the CubeSat, and what are their possible combinations?*
- *What are the specific input parameters of the vibrational analyses, whose variations have the greatest influence on the results?*
- *What is the thermoelastic behaviour of the CubeSat under the thermal loads encountered during its orbit?*

These sub-questions address the structural design, the vibrational analysis, the sensitivity analysis, and the thermoelastic analysis, respectively.

## 3.2. Research Plan

The first step of this plan is to design a CAD model of the complete CubeSat using the educational license of Autodesk Fusion. This CAD software is chosen for its good collaborative features, ease of use in parametric modelling, and capabilities of performing virtual checks, such as measuring masses and dimensions and identifying interference between components. During this design process, it is important to consider not only the modelling of the primary structure itself, but also what hardware components fit within the limited space available and the arrangement of those components that satisfy requirements from the dispenser. A list of all components present in the CAD model is created along with a mass breakdown, and they are categorised according to their subsystems.

Once a particular design version is complete, structural FE analyses are performed on that design using the academic research licence of ANSYS Workbench 2024 R2, which has a variety of modules depending on the type of load being analysed. The loads specified by the launch vehicle provider will be used in vibrational analyses, while the temperatures of various components due to thermal loads in orbit are used as inputs for thermoelastic analyses. As the CAD model is complex due to the large number of components and certain geometric features, it needs to be simplified before being used in the FE

analyses to reduce the computational effort. After meshing the geometry of the model, and applying appropriate loads and constraints, the analyses are run using 12 cores of an Intel Core i7-13700H processor. The results are used to calculate margins of safety, which indicate whether the CubeSat can withstand the loads or not.

When the margins of safety are acceptable, the design of the CubeSat is finalised, but certain parameters used for the FE analyses have some uncertainty. Hence, sensitivity analyses on those parameters are carried out using optiSLang, which is included in the ANSYS license. The results of the sensitivity analysis would prove to be useful for the validation of the FE analyses, which will be carried out by future team members in the next phase of the project.

# 4

# Structural Design

## 4.1. Components

### 4.1.1. Payload

The payload of the CubeSat is a hyperspectral camera developed by HYSPIM, as shown in Figure 4.1, and some of its specifications are mentioned in Table 4.1. It includes all necessary optical components as well as data ports on one of its sides to interface with the bus subsystems. This camera would capture data using the pushbroom method and cover a swath width of 20 km. It should be noted that this camera is not space-grade, and the company is in the process of customising it to withstand the launch vehicle loads and the space environment [56]. Although a few other companies did offer space-grade hyperspectral cameras specifically meant to be used on CubeSats, the costs of these were beyond the budget of the mission.


**Figure 4.1:** HYSPIM Hyperspectral Camera [56]

**Table 4.1:** Payload specifications [56]

| Parameter | Value |
|---|---|
| Dimensions | 60 mm × 60 mm × 220 mm |
| Mass | 1.035 kg |
| Spectral range | 400 nm – 950 nm |
| Spectral resolution | 2.5 nm |
| Spatial resolution | 50 m |
| Bit depth | 12 |

Despite the fact that the actual CAD model for the camera was unavailable, a datasheet from the company containing technical drawings was used to create a reasonably accurate CAD model within Fusion. The external features of the camera were modelled, as only these were visible from the drawings. As a result, the camera was modelled as a solid block with a uniform density assigned to it. The numerical value of this density was determined using the known mass of the camera and its volume calculated from Fusion. This assumption, while modelling, would not result in the actual CG and MOI properties of the camera. However, this was seen as the best approach given the fact that no information was provided on the internal components and their material properties.

### 4.1.2. Primary Structure

As a starting point for modelling the complete CubeSat, it was decided to utilise a COTS 3U CubeSat structure, specifically the one developed by EnduroSat. The main reason behind doing so was to avoid modelling a generic primary structure according to the CDS document and instead make use of the advantages of an already flight-proven design.

Unsurprisingly, an NDA was required by the company to obtain the actual CAD model of the structure, but it was not possible to sign it because of the usage of Fusion, which is a collaborative cloud-based platform. Moreover, even if the NDA was signed, the CAD model from the company was likely to contain numerous unnecessary components and geometric features that would need to be removed before performing the FE analyses. Nevertheless, the company provided a datasheet containing technical drawings, which served as a guide for creating CAD models of the structural components. A few modifications to these components from their original designs are described in Appendix A.

The CubeSat structure is of modular construction and hence, compatible with a large number of subsystem components developed within the same company as well as others. It is designed to be minimalistic and consists of two major types of elements, namely, end frames and side frames, each having a nominal thickness of 1.6 mm. The two end frames are located on the $\pm Z$ sides of the CubeSat, whereas the two side frames are located on the $\pm X$ sides of the CubeSat. A large number of holes on the side frames, as well as a few more on the end frames, ensure an adequate number of mounting points for different arrangements of subsystem components that can support diverse CubeSat missions.

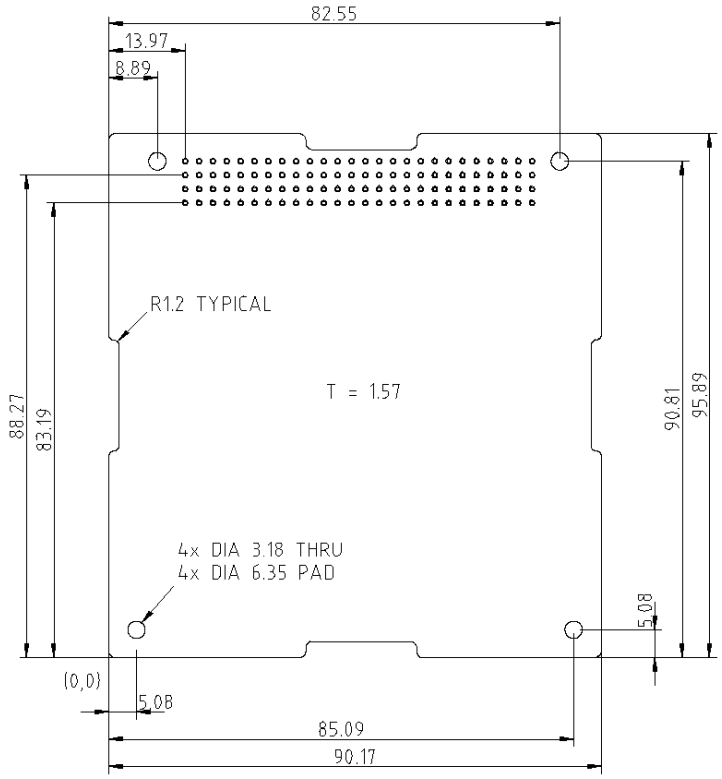


**Figure 4.2:** PC104 dimensions [57]

Along the longer length of the CubeSat are four guide rods, each having a diameter of 3 mm, where the bus subsystem components are slid and stacked upon each other. There are two M3 washers per guide rod, each having a thickness of 0.5 mm and an outer diameter of 8 mm, resulting in a total of eight washers. The ends of the guide rods are connected to holes on the two end frames and are arranged in such a way that they follow the PC104 configuration shown in Figure 4.2. As the payload did not have mounting points according to this configuration, a mount was designed to attach the payload to the side frames. Finally, a total of 32 M3 screws bring the whole assembly together: 8 connecting each end frame to both side frames, and 16 connecting the payload mount to the side frames. Figure 4.3 depicts the various components present in the primary structure except for the screws and washers.

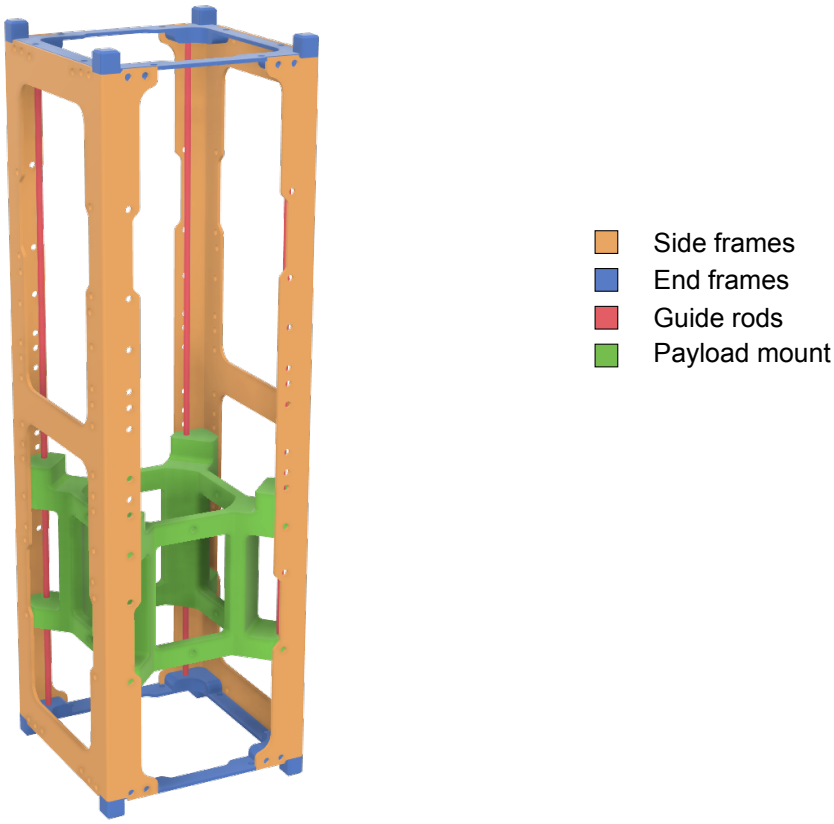


**Figure 4.3:** Components in primary structure

Though the actual material used for the end frames and side frames in the flight-proven version was Aluminium 6082-T6 alloy, it was proposed to manufacture these using the stronger Aluminium 7075-T6 alloy, with all external surfaces being hard anodised. It was also decided to utilise the same material for the payload mount. Although the material used for the screws, washers, and guide rods was unknown, they were assumed to be 304 Stainless Steel. The relevant mechanical properties of these materials are shown in Table 4.2.

**Table 4.2:** Mechanical properties of materials

| Material | $\rho$ [kg/m$^3$] | $E$ [GPa] | $\nu$ | $\sigma_Y$ [MPa] | $\sigma_U$ [MPa] | $\alpha$ [1/K] | Reference |
|---|---|---|---|---|---|---|---|
| Aluminium 7075-T6 | 2,810 | 70 | 0.32 | 480 | 560 | $23 \times 10^{-6}$ | [58] |
| Stainless Steel AISI 304 | 7,930 | 200 | 0.28 | 230 | 580 | $17 \times 10^{-6}$ | [59] |

### 4.1.3. Bus Subsystems

All the components shown in Figure 4.4 were found to satisfy the requirements of the payload and the mission as a result of trade-offs performed by fellow team members working on the bus subsystems. Upon consultation with a coordinator from the Fly Your Satellite program, it was found that past CubeSat teams faced difficulties in integrating the software of subsystem components that were from different companies. To avoid this issue in the later stages of the mission, the present CubeSat makes use of as many components as possible from EnduroSat itself.

The S-band (2 GHz to 4 GHz) components would be used to receive commands from the ground station and transmit tracking data back to it. The S-band components alone have a slow data transfer rate of 10 Mbps, and hence, the X-band (8 GHz to 12 GHz) components, having a data transfer rate of 100 Mbps, would be used for downlinking the hyperspectral data from the payload. The onboard computer is built on an ARM Cortex M7 processor with a frequency rate up to 480 MHz, providing robust computing capabilities required for data processing, and also features an integrated GNSS receiver. The battery is an 8-cell variant having a capacity of 84 Wh and consists of a power distribution and management system. The configuration of the body-mounted solar panel and the double deployable solar arrays was found to be the most effective in generating the power required by all other subsystems for various modes of operation.

Just like the structure, NDAs were once again required to obtain the actual CAD models for all components, but their datasheets proved to be useful as they had technical drawings, which were then used to create the CAD models. In a similar methodology to that of the payload, only the external features of all components were modelled, and they were solid blocks with uniform densities assigned to each of them based on their known masses.

As EnduroSat did not offer AOCS components in their catalogue, these were selected from another company, AAC Clyde Space. The integrated ADCS module offered a pointing accuracy significantly less than 1°, which was suitable for hyperspectral imaging applications. This component consisted of a number of individual subcomponents, such as magnetorquers, reaction wheels, and a star tracker, arranged within a compact volume, but as expected, a CAD model for this required an NDA. Hence, by using the known external dimensions mentioned in its datasheet, this component was also approximated as a solid block.

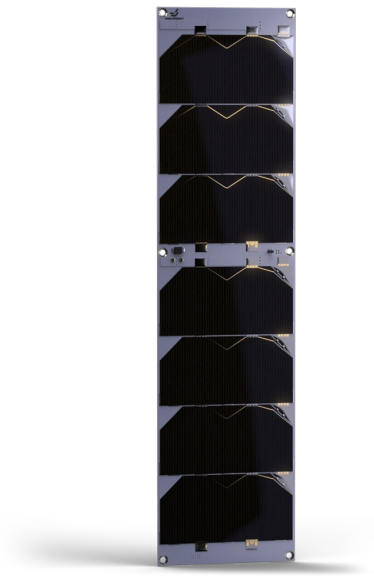

**(a)** EnduroSat 3U Solar Panel [60]

**(b)** EnduroSat 3U Double Deployable Solar Array [61]

**(c)** EnduroSat EPS II + Battery Pack [62]

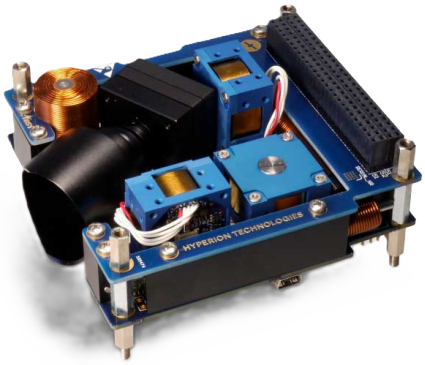


**(d)** AAC Clyde Space iADCS200 [63]

**(e)** EnduroSat Onboard Computer with GNSS [64]

**(f)** EnduroSat S-Band Transceiver [65]

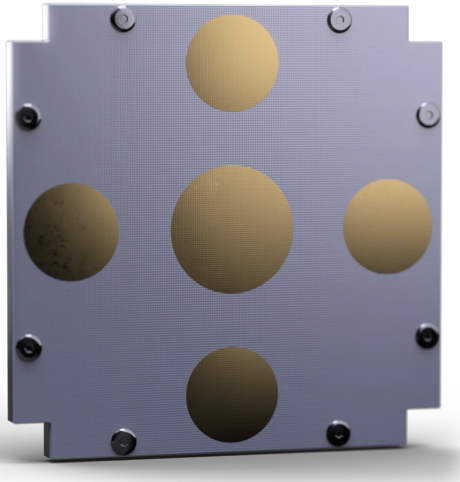

**(g)** EnduroSat S-Band Antenna Wideband [66]

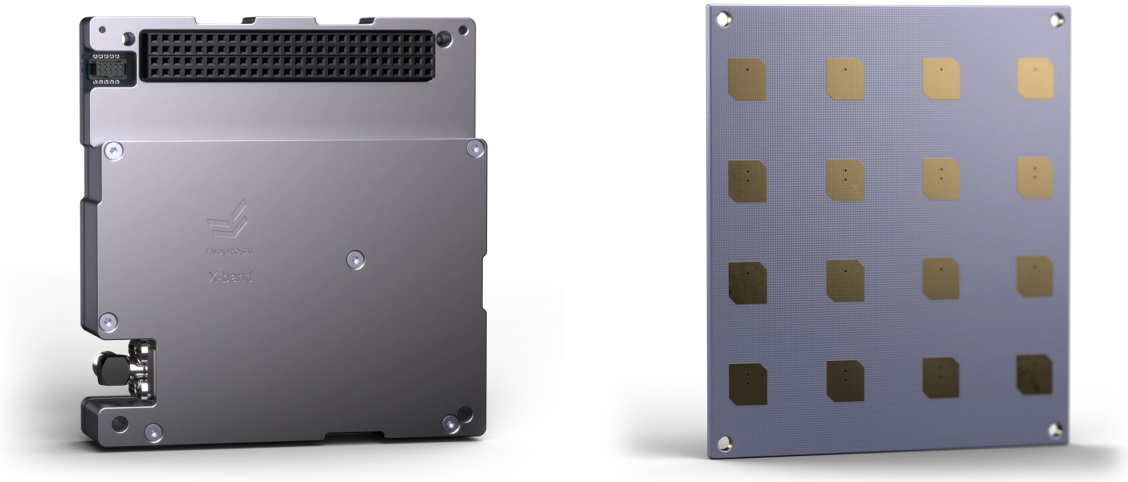

**(h)** EnduroSat X-Band Transmitter [67] **(i)** EnduroSat X-Band 4×4 Patch Array [68]

**Figure 4.4:** Selected subsystem components

## 4.2. Dispenser Compatibility

A major challenge initially was to determine whether the extremely bulky payload could fit within the 3U form factor while ensuring sufficient remaining volume for the bus subsystems. Using the extra tuna-can volume to accommodate a portion of the payload was seen as a possible solution, but even this volume specified in the CDS document was found to be inadequate. The other option of shifting the platform to that of a 6U CubeSat would defeat the purpose of the main research question. In addition to the payload, the protrusions due to the deployable solar panels in their stowed configurations would most likely exceed the allowable limits mentioned in the CDS document. Hence, various dispensers that could be compatible with the CubeSat were searched, and among all of them, the EXOpod Nova dispenser shown in Figure 4.5 developed by Exolaunch stood out. Some of the specifications of this dispenser were far greater than those of the CDS document, as shown in Table 4.3, but the CubeSat CG requirements were the same for both.


**Figure 4.5:** Exolaunch EXOpod Nova dispenser [24]

Apart from the extra volume, this dispenser has other notable advantages. Since 2017, it has deployed more than 300 CubeSats on various launch vehicles, such as Falcon 9, Electron, and Ariane 6, among many others [69]. The Ariane 6 case was particularly interesting as this dispenser carried two

**Table 4.3:** Specifications of EXOpod Nova dispenser

| Parameter | CDS document [39] | EXOpod Nova user manual [24] |
|---|---|---|
| Tuna-can diameter [mm] | 64 | 93 |
| Tuna-can length [mm] | 36 | 78 |
| Maximum side protrusion from rail [mm] | 6.5 | 25 |
| Maximum width of side protrusion [mm] | 83 | 87.2 |
| Maximum 3U CubeSat mass [kg] | 6 | 7 |

educational CubeSats (ISTsat-1 and 3Cat-4), similar to the present one, which were developed through the Fly Your Satellite program. This dispenser has also been designed to provide significant isolation from shock loads, particularly at higher frequencies. As shown in Figure 4.6, the acceleration SRS experienced by the CubeSat is much lower compared to the original acceleration SRS from the Falcon 9. Keeping the requirements from this dispenser in mind, the CAD model of the complete CubeSat was created.

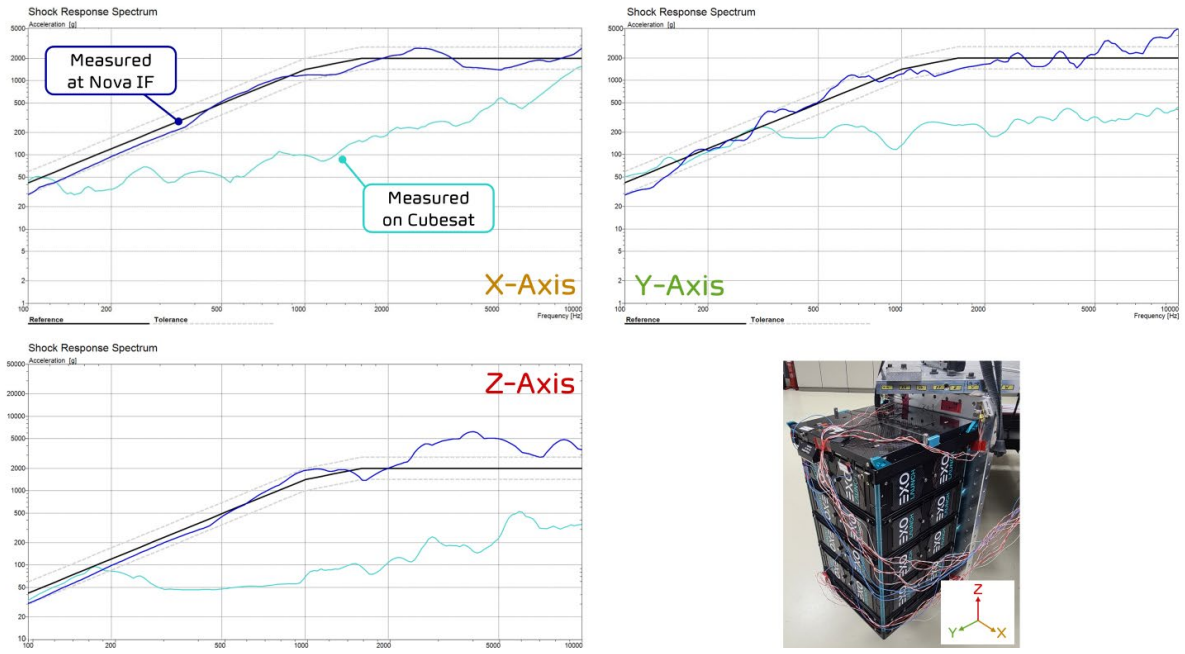


**Figure 4.6:** Shock loads reduction from dispenser [24]

## 4.3. CAD Model Description

Various views of the finalised CubeSat CAD model are shown in Figure 4.7, while a summary of all the components present in this CAD model is shown in Table 4.4. All previous design iterations on this CAD model are elaborated in Appendix A. With the exception of the structure and the payload mount, the masses of all components were exactly what the companies quoted in their datasheets, according to specific configurations. After applying a 20% margin at the system level, usually chosen for preliminary designs [70], the total mass of the CubeSat was 6.482 kg, which was more than the maximum allowable of the CDS document but still less than that of the EXOpod Nova user manual. Furthermore, as the payload was still under development, it was proposed that the final mass of this does not exceed 1.466 kg so that the total mass of the CubeSat does not exceed 7 kg after considering margins.

While the solar panels and the patch antennae are attached externally on the side frames, all the other components are internal. Each deployable solar array consists of two panels having seven cells per panel and a third panel without cells, which is attached to the structure. As they are present on the $\pm X$ sides of the CubeSat, when the panels swing in opposite directions to each other during deployment, any torques arising would cancel each other out. More importantly, the maximum side protrusion of

these panels in the stowed configuration is 8.17 mm, while their width is 87.02 mm, and both of these are within the limits specified in the EXOpod Nova user manual. The body-mounted solar panel, also having seven cells, is placed on the $+Y$ side of the CubeSat so that once fully deployed, five panels with cells would directly face the sun.

As three of the larger sides of the CubeSat are occupied by the solar panels, the fourth side, that is, the $-Y$ side, is kept free to attach both the patch antennae. It should be noted that the star tracker of the AOCS module is also pointed towards the $-Y$ side and requires unobstructed access to the exterior of the CubeSat. Hence, there is a space between the two patch antennae, where no other components are present. The mounting points for the solar panels and the patch antennae perfectly matched the holes on the side frames due to the fact that all these components were from EnduroSat. Moreover, care was taken to ensure that a particular hole on the side frame was connected to exactly one other component, to avoid undesirable load paths.

**Table 4.4:** CubeSat mass breakdown

| Component | Subsystem | Mass [g] | Location | Reference |
|---|---|---|---|---|
| EnduroSat<br>Modified 3U CubeSat Structure<br>(including screws and washers) | Primary structure | 360 | - | [44] |
| Custom-made<br>Payload mount | Primary structure | 328 | Internal | - |
| HYSPIM<br>Hyperspectral Camera | Payload | 1,035 | Internal | [56] |
| EnduroSat<br>3U Solar Panel | EPS | 146 | External | [60] |
| EnduroSat<br>3U Double Deployable Solar Array | EPS | 2 × 438 | External | [61] |
| EnduroSat<br>EPS II + Battery Pack | EPS | 1,373 | Internal | [62] |
| AAC Clyde Space<br>iADCS200 | AOCS | 470 | Internal | [63] |
| EnduroSat<br>Onboard Computer with GNSS | CDHS + AOCS | 130 + 50 | Internal | [64] |
| EnduroSat<br>S-Band Transceiver | TTCS | 191 | Internal | [65] |
| EnduroSat<br>S-Band Antenna Wideband | TTCS | 115 | External | [66] |
| EnduroSat<br>X-Band Transmitter | TTCS | 275 | Internal | [67] |
| EnduroSat<br>X-Band 4×4 Patch Array | TTCS | 53 | External | [68] |
| Total mass<br>Total mass including margin | | 5,402<br>6,482 | | |

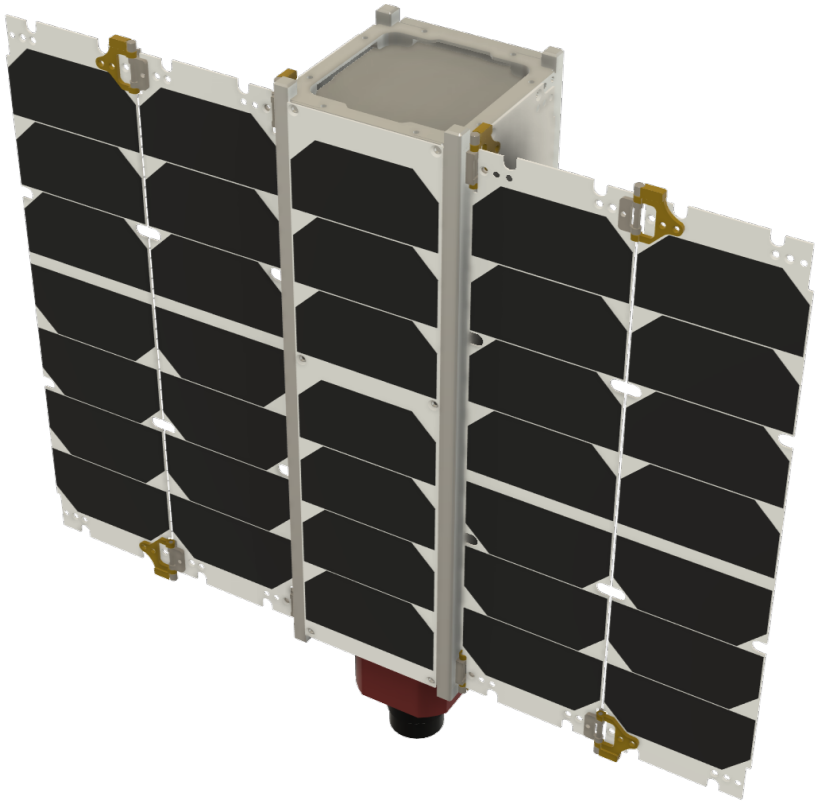

**(a)** Solar panels deployed

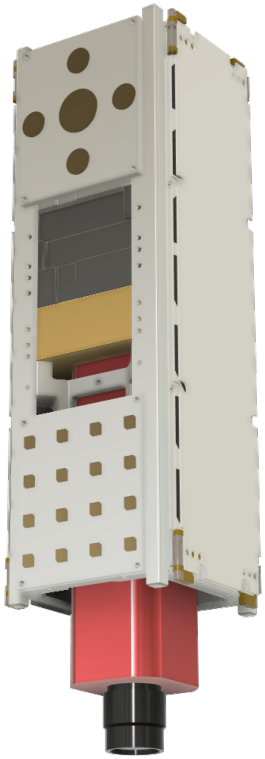

**(b)** Solar panels stowed

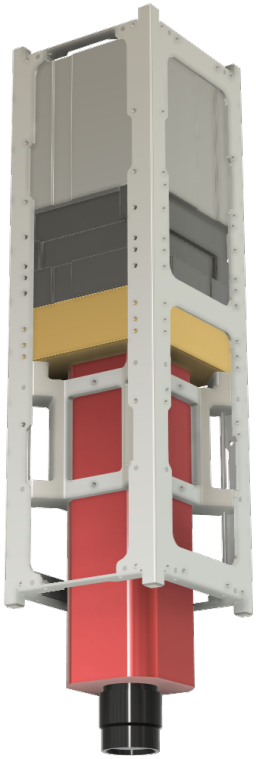

**(c)** Internal components visible

**Figure 4.7:** CAD model views

The payload is placed such that it protrudes out from the -$Z$ end of the CubeSat, as this is where the extra tuna-can volume is located. The diameter of the bounding cylinder around the payload is 70.28 mm, while it protrudes 77.25 mm from the end of the CubeSat rail, both of which satisfy the requirements from the EXOpod Nova user manual. The internal bus subsystem components are stacked along the guide rods in the following order, starting from the +$Z$ end of the CubeSat: The EPS II + Battery Pack, the Onboard Computer with GNSS, the S-Band Transceiver, the X-Band Transmitter, and the iADCS200. As they all follow the PC104 configuration, they are interconnected through dual interface points and are collectively held together by washers between the payload mount and the +$Z$ end frame.

The coordinates of the CubeSat CG are -0.10 mm, -0.68 mm, and 2.81 mm when the solar panels are stowed, while they change to -0.10 mm, 4.42 mm, and 2.81 mm when the solar panels are deployed, and both of these are well within the limits specified in the CDS document. This could be attributed to the fact that both the heaviest components, which are the EPS II + Battery Pack and the payload, are placed on opposite sides of the CubeSat, thereby cancelling each other's influence. From Figure 4.8, it is clear that the EPS occupies nearly half the mass of the CubeSat, and this was expected from an energy-intensive hyperspectral imaging payload. It should be noted that components of the TCS are not included here, as most of the other subsystem components have built-in temperature control elements within them.

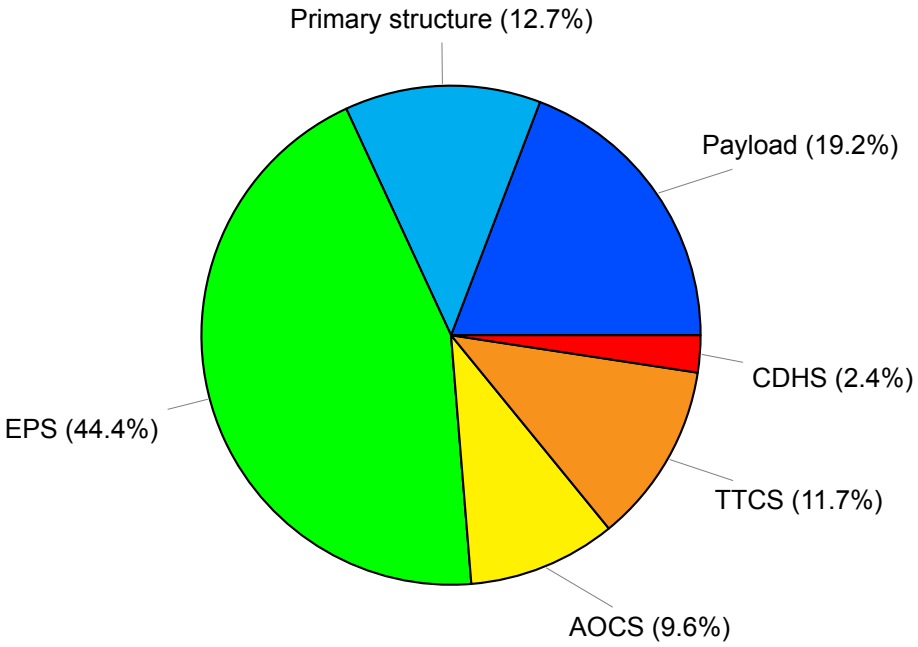


**Figure 4.8:** CubeSat subsystem mass distribution

## 4.4. Mock-Up Model

As shown in Figure 4.9, a mock-up model of the CubeSat was created using 3D printed plastic, in order to get an idea of the sizes of its various components. This model would later serve as a platform to be integrated with a chassis and wheels for a mock-up model of the EMEC-2 CubeSat-based rover. The internal bus components, the payload mount, and the guide rods were printed with PLA by a fellow team member using the Prusa 3D printers available at the Delft Aerospace Structures and Materials Laboratory. However, those printers had a limited build volume and were incapable of printing components with thicknesses below 2 mm. Hence, the end frames and side frames were printed with PETG by the Delft-based company MTB3D [71]. Similar to the flight version, the components of the mock-up model were also assembled together using M3 screws.

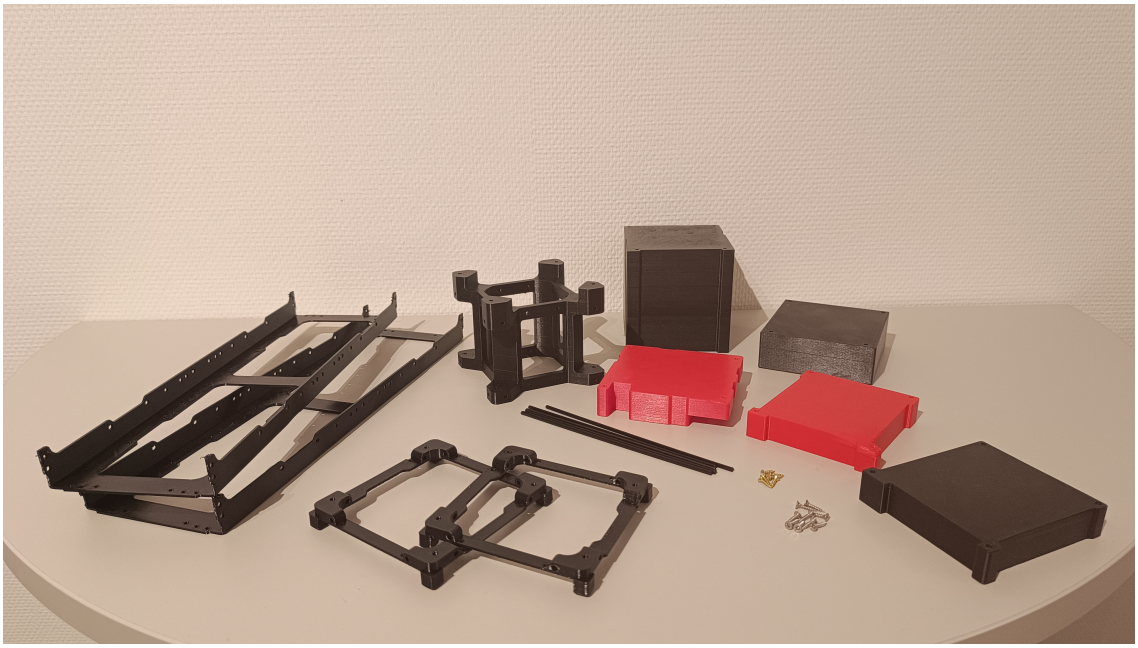

**(a)** Disassembled

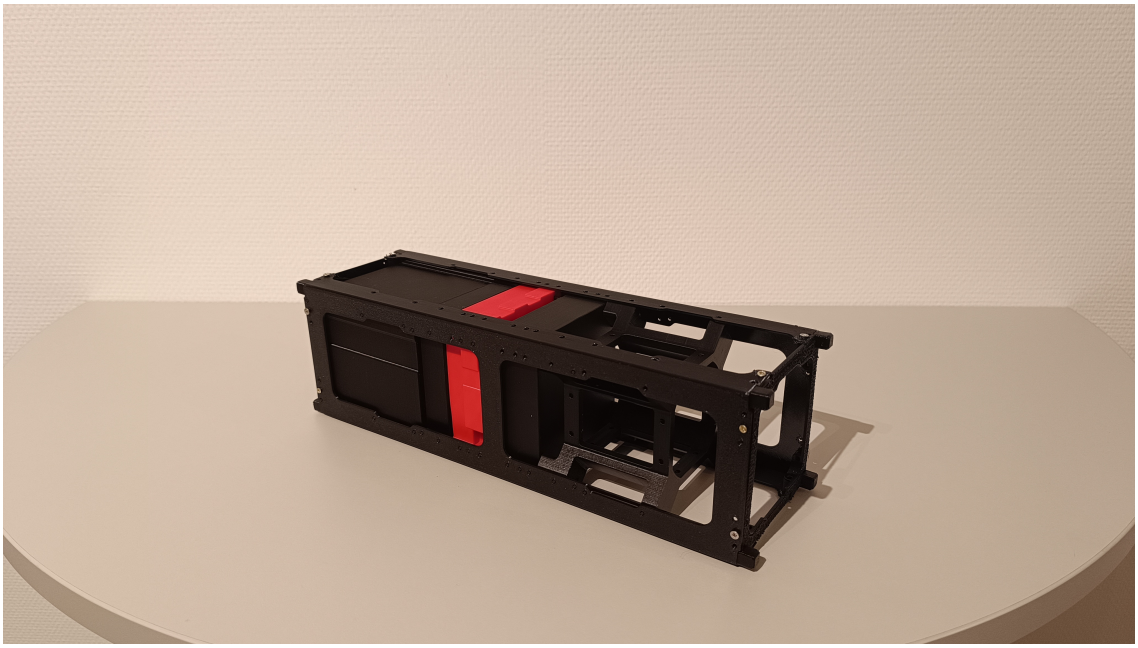

**(b)** Assembled

**Figure 4.9:** CubeSat mock-up model

# 5

# Vibrational Analysis

## 5.1. Theory Notes

### 5.1.1. Modal Analysis

The modal analysis is performed to determine the natural frequencies and mode shapes of the CubeSat. It is also a prerequisite for any other structural dynamic analyses, such as those of sinusoidal vibrations, random vibrations, and shock loads [72].

The general MDOF equation of motion derived from Hamilton's principle, which relates inertial forces, damping forces, elastic forces, and external forces, is given by:

$$\boldsymbol{M}\ddot{\boldsymbol{u}} + \boldsymbol{C}\dot{\boldsymbol{u}} + \boldsymbol{K}\boldsymbol{u} = \boldsymbol{F}$$

In this, $\boldsymbol{M}$, $\boldsymbol{C}$, and $\boldsymbol{K}$ are the mass, damping, and stiffness matrices, while $\boldsymbol{u}$, $\dot{\boldsymbol{u}}$, $\ddot{\boldsymbol{u}}$, and $\boldsymbol{F}$ are the displacement, velocity, acceleration, and force vectors corresponding with $N$ degrees of freedom. For a modal analysis, a free undamped system is considered, and the equation is rewritten as:

$$\boldsymbol{M}\ddot{\boldsymbol{u}} + \boldsymbol{K}\boldsymbol{u} = \boldsymbol{0}$$

Upon considering a general solution of the form $\boldsymbol{u}(t) = \boldsymbol{U}e^{\iota\omega_n t}$, where $\boldsymbol{U}$ gives the displacement shape and $e^{\iota\omega_n t}$ is a harmonic function, the equation is further rewritten as:

$$\left(-{\omega_n}^2\boldsymbol{M} + \boldsymbol{K}\right)\boldsymbol{U}e^{\iota\omega_n t} = \boldsymbol{0}$$

As $e^{\iota\omega_n t} \neq 0$, the equation is simplified and takes the form of the generalised eigenvalue problem:

$$\left(-{\omega_n}^2\boldsymbol{M} + \boldsymbol{K}\right)\boldsymbol{U} = \boldsymbol{0}$$

As the trivial solution $\boldsymbol{U} = \boldsymbol{0}$ is neglected, the condition $\det(-{\omega_n}^2\boldsymbol{M} + \boldsymbol{K}) = 0$ must be satisfied for the above equation to hold true for any other vector $\boldsymbol{U}$. This can be solved for many pairs of eigenvalues $(-{\omega_n}^{(I)^2})$ and their corresponding eigenvectors $\boldsymbol{U}^{(I)}$. In other words, $\boldsymbol{U}^{(I)}$ represents the mode shape corresponding to the natural frequency ${\omega_n}^{(I)}$.

After replacing $\boldsymbol{U}$ with $\boldsymbol{U}^{(I)}$, and premultiplying by ${\boldsymbol{U}^{(I)}}^\top$, the equation known as Rayleigh's equation is obtained. From this, it can be inferred that the natural frequencies of the system are lower when there is less stiffness and more mass.

$$\frac{{\boldsymbol{U}^{(I)}}^\top\boldsymbol{K}\boldsymbol{U}^{(I)}}{{\boldsymbol{U}^{(I)}}^\top\boldsymbol{M}\boldsymbol{U}^{(I)}} = {\omega_n}^{(I)^2}$$

### 5.1.2. Random Vibrations

A random process cannot be represented with certainty as a function of time, and a statistical approach is followed to analyse them [73]. In the scope of the present work, these processes are assumed to be stationary, ergodic, and follow a Gaussian distribution.

A process $x(t)$ is stationary when its statistical properties from a sample of this process, such as the mean value $E(x)$, the mean square value $E(x^2)$, and the variance $V(x)$, are not affected by the initial time chosen to extract the sample. A stationary process is ergodic when its statistical properties can be deduced from a single, sufficiently long sample of the process. For a stationary and ergodic random process $x(t)$ which follows a Gaussian probability density function $f(x)$, the following equations hold true:

$$E(x) = \int_{-\infty}^{\infty} x f(x)\, dx = \lim_{T\to\infty} \frac{1}{T} \int_0^T x(t)\, dt$$

$$E(x^2) = \int_{-\infty}^{\infty} x^2 f(x)\, dx = \lim_{T\to\infty} \frac{1}{T} \int_0^T x^2(t)\, dt = [E(x)]^2 + V(x)$$

The autocorrelation function $R_{xx}(\tau)$ of such a random process $x(t)$ represents the correlation of this process with itself at points separated by various times $\tau$ and is defined as:

$$R_{xx}(\tau) = E\{x(t)\, x(t+\tau)\} = \lim_{T\to\infty} \frac{1}{T} \int_0^T x(t)\, x(t+\tau)\, dt$$

Upon taking the Fourier transform of this autocorrelation function, the Power Spectral Density (PSD) function $S_{xx}(\omega)$ is obtained:

$$S_{xx}(\omega) = \int_{-\infty}^{\infty} R_{xx}(\tau)\, e^{-\iota\omega\tau}\, d\tau = 2\int_0^{\infty} R_{xx}(\tau)\cos(\omega\tau)\, d\tau$$

The PSD function can represent different quantities depending on the unit of the random process being considered. In the case of random vibrations from the launch vehicle, the acceleration PSD is usually specified and has the units of ${g_{rms}}^2$/Hz, which is simply written as $g^2$/Hz. For these vibrations, the $g_{rms}$ is the root mean square value of the acceleration amplitude at a particular frequency. Furthermore, as these vibrations have zero mean, the $g_{rms}$ is equivalent to the standard deviation of the acceleration amplitude at that frequency.

For most MDOF systems, a transfer function $H(\omega)$ can be derived based on the frequency response of a unit load. Hence, the output response $S_{out}(\omega)$ to the input random vibration load $S_{in}(\omega)$ also takes the form of a PSD function as shown below:

$$S_{out}(\omega) = |H(\omega)|^2 S_{in}(\omega)$$

For an SDOF system, the equivalent root mean square acceleration response to a constant acceleration PSD is given by Miles' equation, where $S_{in}(\omega_n)$ is the value of the input acceleration PSD at resonance, $f_n$ is the resonance frequency in Hz, and $Q$ is the quality factor or transmissibility at resonance.

$$g_{rms,out} = \sqrt{\frac{\pi}{2}\, f_n\, Q\, S_{in}(\omega_n)}$$

### 5.1.3. Shock Loads

The shock loads from the launch vehicle are usually represented by an acceleration Shock Response Spectrum (SRS). The SRS is generated by calculating the maximum acceleration response of a hypothetical SDOF system, such as a mass on a spring, to an enforced base acceleration. By varying the natural frequency of the SDOF system for the same excitation, the peak response as a function of

frequency is obtained. It is important to note that the damping of the SDOF system is kept constant for all cases and is typically taken as a quality factor of 10, or a $\zeta$ of 0.05 [74].

For an SDOF system consisting of a mass on a spring with an enforced base acceleration $\ddot{u}(t)$, the absolute acceleration $\ddot{x}(t)$ of the mass can be determined. This process is repeated for every value of $\omega_n$ to generate the SRS.

$$\ddot{x}(t) = 2\zeta\omega_n \int_0^t e^{-\zeta\omega_n(t-\tau)} \cos(\omega_d(t-\tau))\ddot{u}(\tau)\, d\tau + \omega_n(2\zeta^2 - 1)[x(t) - u(t)]$$

### 5.1.4. Margin of Safety

The Margin of Safety ($MOS$) is a parameter used in many engineering fields to determine whether a system can withstand mechanical loads after accounting for various uncertainties. The methodology for calculating $MOS$ in the scope of the present work is specific to that of spacecraft design [75]. For any particular load case being analysed, the value of $MOS$ calculated in the following equation shall always be positive:

$$MOS = \frac{DA}{DLL \times FOS} - 1$$

The Design Allowable ($DA$) is the statistically based strength capability of the material with respect to a failure mode. In other words, it can be either the yield strength ($\sigma_Y$) or the ultimate strength ($\sigma_U$) of the material. The former is chosen if permanent deformations in CubeSat structures are to be avoided, and this is followed for most cases. However, if the material is brittle, then $\sigma_U$ is used instead of $\sigma_Y$.

The Limit Load ($LL$) is the maximum load that CubeSat structures are expected to experience with a given probability during a specified loading environment, such as those specified by the launch vehicle MPE. The maximum von-Mises stress ($\sigma_{vm,max}$) observed in an FE analysis for a particular load case is usually taken as the $LL$.

The Design Factor ($DF$) is a combination of three factors as follows:

- The qualification test factor ($KQ$) is applied specifically for satellite development. This is because the qualification loads, which are slightly higher than the MPE, are later used in the test campaign of the physical model. A typical value of 1.25 is used, and this is also mentioned in the manuals for the launch vehicles.
- The project factor ($K_P$) is applied to account for the maturity of the program with respect to stable mass and cost budgets, as well as a well-identified design. The present CubeSat utilises a standardised form factor and numerous COTS components, which have flight heritage. However, it is in the early stage of development, and some of these components are bound to change. Hence, a moderately conservative value of 1.1 is selected.
- The model factor ($K_M$) is applied to account for uncertainties in mathematical models, such as those used in FE analyses when predicting dynamic responses and evaluating load paths. As all FE analyses are conducted for the first time for this CubeSat, a highly conservative value of 1.2 is used.

The $DF$ is multiplied with the $LL$ to get the Design Limit Load ($DLL$) as shown in the following equation:

$$DLL = LL \times DF = LL \times KQ \times K_P \times K_M$$

The Factor of Safety ($FOS$) is multiplied with the $DLL$ to account for uncertainties in the verification methods, manufacturing process, and material properties. It can either be a yield design factor of safety ($FOSY$) or an ultimate design factor of safety ($FOSU$), depending on whether $DA$ is chosen to be $\sigma_Y$ or $\sigma_U$. The values of $FOSY$ and $FOSU$ for different materials are shown in Table 5.1. The present CubeSat will also undergo a test campaign, but when the verification of the design is carried out just by analysis to cut costs, a higher value of $FOS$ is naturally used to account for additional uncertainties. The present CubeSat consists of a majority of metal components, and hence a value of 1.1 is taken.

**Table 5.1:** $FOS$ for different materials and verification scenarios [75]

| Material | Verification by analysis and testing | | Verification by analysis only | |
|---|---|---|---|---|
| | $FOSY$ | $FOSU$ | $FOSY$ | $FOSU$ |
| Metals | 1.1 | 1.25 | 1.25 | 2 |
| Composites | Unspecified | 1.25 | Unspecified | 2 |
| Ceramics | Unspecified | 2.5 | Unspecified | 5 |

In some cases, a local design factor ($K_{LD}$) having a value of 1.2 is also included in the $DLL$ to account for specific uncertainties in areas where significant stress gradients occur, such as near holes, corners, etc. Upon multiplying all the factors together, as shown in the following equation, the Design Yield Load ($DYL$) or the Design Ultimate Load ($DUL$) is obtained:

$$DYL = DLL \times FOSY = LL \times KQ \times K_P \times K_M \times K_{LD} \times FOSY$$

Hence, the $MOS$ against yielding is shown in the following equation:

$$MOS = \frac{\sigma_Y}{DYL} - 1 = \frac{\sigma_Y}{\sigma_{vm,max} \times KQ \times K_P \times K_M \times K_{LD} \times FOSY} - 1$$

The numerical values used for the different factors are carefully selected to ensure an accurate calculation of $MOS$ and that the design is neither over-engineered for the loads nor weak enough that it fails. Some of these values for previous educational CubeSats are shown in Table 5.2.

**Table 5.2:** Values of factors in previous educational CubeSats

| | $KQ$ | $K_P$ | $K_M$ | $K_{LD}$ | $FOS$ | Reference |
|---|---|---|---|---|---|---|
| AlAinSat-1 | 1.25 | 1 | 1 | 1 | 1.25 | [50] |
| MIST | 1.25 | 1 | 1.25 | 1 | 1.25 | [51] |
| ISTsat-1 | 1.25 | 1 | 1.1 | 1 | 1.5 | [52] |
| TeideSat | 1.25 | 1.2 | 1.2 | 1 | 1.25 | [53] |

## 5.2. Launch Vehicle Loads

### 5.2.1. Comparison

As discussed in Chapter 2, the CubeSat within the dispenser must withstand the flight-level MPE during launch. The user manuals for launch vehicles provide essential information on the MPE so that CubeSat developers can perform structural analyses on their designs. The manuals for Falcon 9, Electron, Ariane 6, and Vega-C were publicly available online, and hence, it was decided to investigate the loads for each of these launch vehicles further. As they are European vehicles, Ariane 6 and Vega-C were given particular preference, and there was an intention to use one of these eventually. Moreover, by doing so, there would be better chances of the CubeSat being selected for the Fly Your Satellite program. However, Falcon 9 and Electron have impressive reliability, with approximately 500 launches and 70 launches, respectively, and these two vehicles would be kept as backups.

The quasi-static load envelopes are shown in Figure 5.1 for the four vehicles, where positive and negative values represent accelerations along the corresponding directions of the axes. The axial direction is along the $Z$ axis, while the lateral directions are along the $X$ and $Y$ axes, according to the CubeSat coordinate system. The envelope of Electron is the smallest among the four, and Falcon 9 produces a maximum acceleration of ±17 $g$ in the lateral direction. It is interesting to note that both Ariane 6 and Vega-C have identical envelopes of ±10 $g$ in the axial and lateral directions.

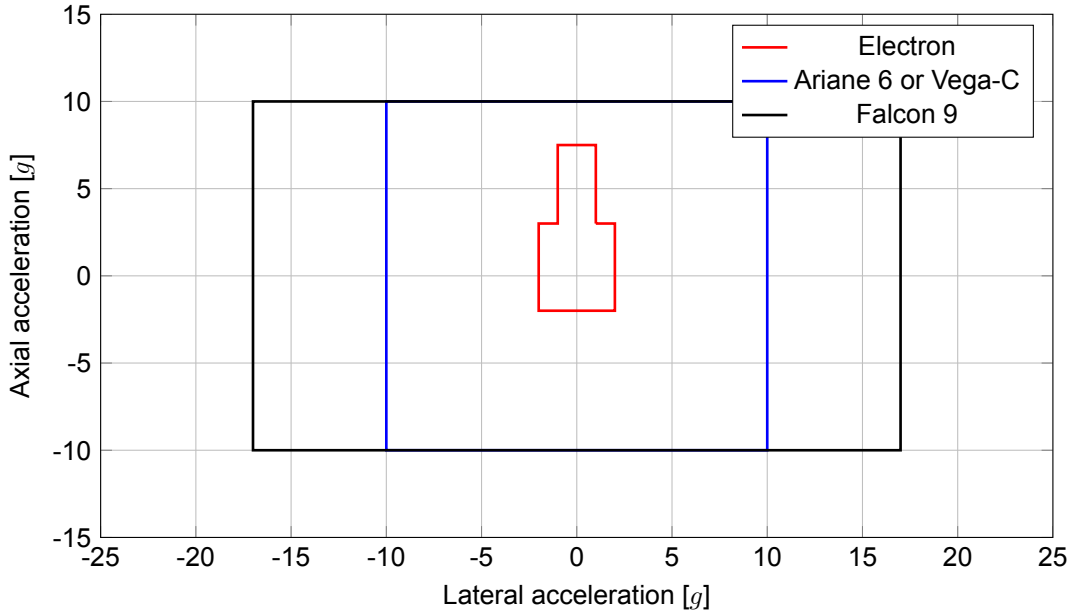


**Figure 5.1:** Quasi-static loads comparison [76][77][78][79]

The sinusoidal vibrations for three of the launch vehicles are in the frequency range of 5 Hz to 125 Hz. The manual for Electron did not specify these loads, but mentioned that they had already been taken into account in the quasi-static load envelope. There is also a requirement for the minimum natural frequency of the CubeSat to be above a certain threshold to prevent dynamic coupling between the vibration modes of the launch vehicle and the CubeSat. For Falcon 9, the minimum frequency is 40 Hz, but for Ariane 6 and Vega-C, the minimum frequency is much higher at 115 Hz. Surprisingly, Electron did not specify any requirements regarding the minimum natural frequency.

The acceleration PSD curves over the frequency range of 20 Hz to 2,000 Hz are shown in Figure 5.2 for the four vehicles. When comparing PSD curves, the parameter of importance is not their maximum values but instead the square root of the area under each curve, which turns out to be $g_{rms}$. The values of $g_{rms}$ are 4.14 $g$, 5.40 $g$, 7.04 $g$, and 5.57 $g$ for Electron, Vega-C, Ariane 6, and Falcon 9, respectively. Hence, Ariane 6 has the most conservative random vibration loads.

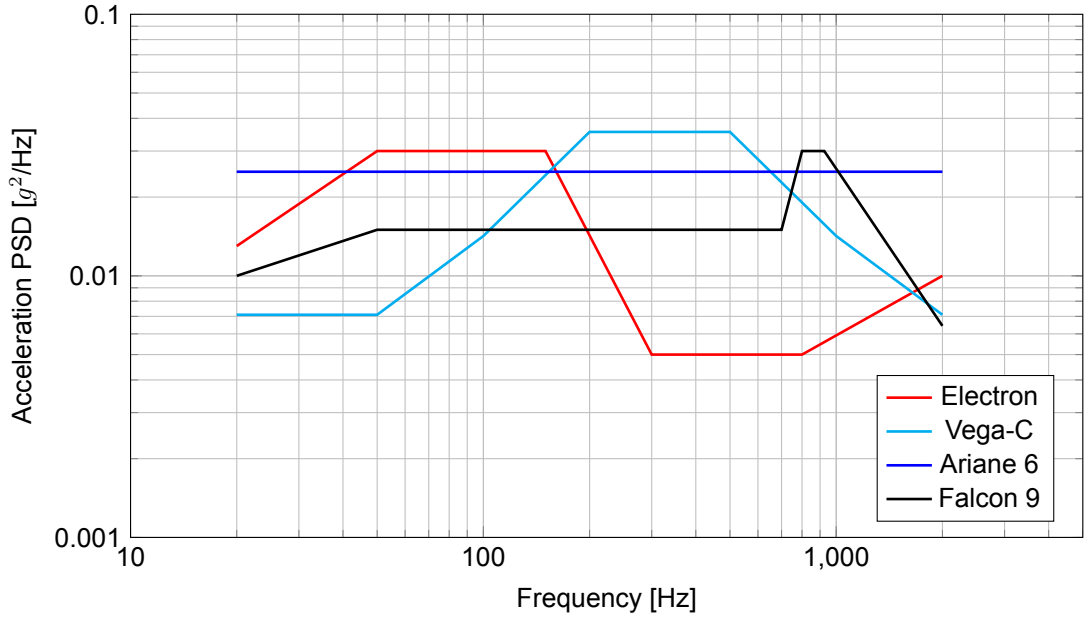


**Figure 5.2:** Random vibrations comparison [76][77][78][79]

The acceleration SRS curves over the frequency range of 100 Hz to 10,000 Hz are shown in Figure 5.3 for the four vehicles. As expected, all these curves were defined assuming $\zeta$ to be 0.05. The shock loads for Falcon 9 are identical to those of Ariane 6. While Electron has the highest loads at frequencies below 500 Hz, the loads of Vega-C dominate at higher frequencies.

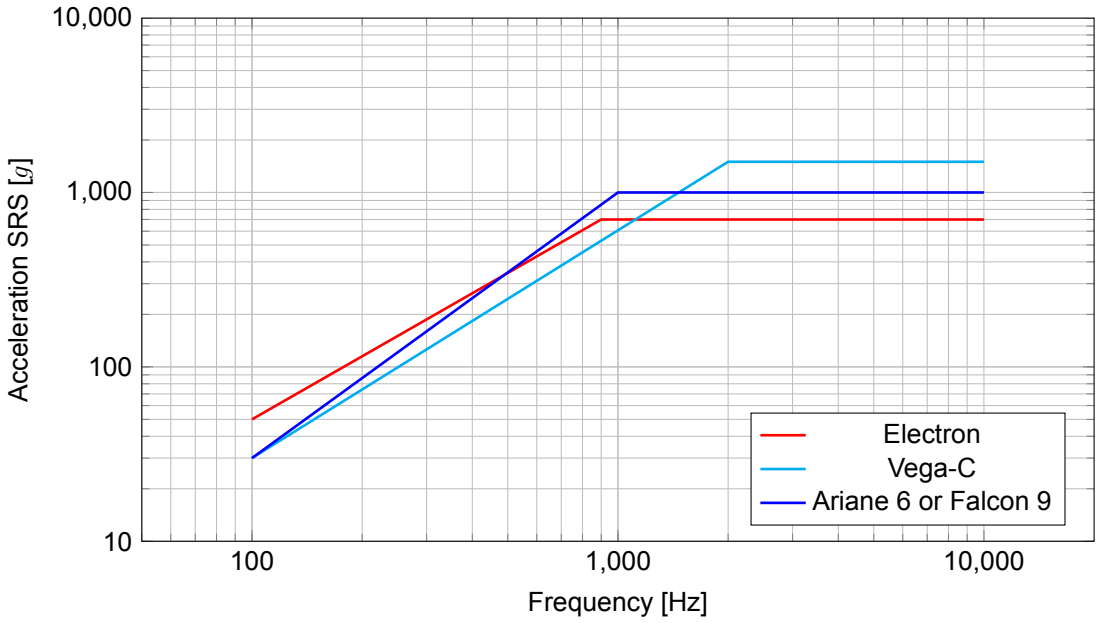


**Figure 5.3:** Shock loads comparison [76][77][78][79]

### 5.2.2. Load Cases

In order to simplify the analysis effort, it is preferable to identify only those load types which are relevant based on certain reasoning. For instance, if the minimum natural frequency of the CubeSat lies outside the frequency range of the sinusoidal vibrations, then resonance is unlikely to be observed, and the FE analyses of these loads can be ignored. As mentioned earlier, acoustic loads can cause

significant responses in large panel-like structures, which are usually present in larger satellites but not in CubeSats, and the FE analyses of these loads are also disregarded. Hence, the focus is only on quasi-static loads, random vibrations, and shock loads.

As both quasi-static loads and random vibrations co-occur while the engines are running, the CubeSat will experience a combination of these two loads to some extent, and it seems logical to assess the combined effect. However, as quasi-static loads are deterministic while random vibrations are not, ANSYS does not allow the application of their combination as an input within a single analysis. Although it is possible to convert the random vibrations to an equivalent quasi-static load using Miles' equation and superimpose it with the other quasi-static loads, such an approach would not yield accurate results for an MDOF system. Moreover, test equipment is incapable of applying combinations of different load types. Based on these arguments, the FE analyses of quasi-static loads and random vibrations were performed separately. Nevertheless, the effects of the pre-stress of the quasi-static loads on the modal analysis and random vibrations analysis are described in Appendix C. The quasi-static loads used for the analysis are shown in Table 5.3 and correspond to the load envelope of Falcon 9. There are a total of 8 cases covering every possible direction of acceleration that the CubeSat would experience. For the random vibrations, the loads corresponding to Ariane 6 are considered, where an acceleration PSD of 0.025 $g^2$/Hz over the frequency range of 20 Hz to 2,000 Hz is applied along all three axes simultaneously.

**Table 5.3:** Input quasi-static loads

| Case | $X$ acceleration [$g$] | $Y$ acceleration [$g$] | $Z$ acceleration [$g$] |
|---|---|---|---|
| 1 | 17 | 17 | 10 |
| 2 | -17 | 17 | 10 |
| 3 | 17 | -17 | 10 |
| 4 | -17 | -17 | 10 |
| 5 | 17 | 17 | -10 |
| 6 | -17 | 17 | -10 |
| 7 | 17 | -17 | -10 |
| 8 | -17 | -17 | -10 |

Shock loads are not combined with other loads since these generally occur at times when the launch vehicle is 'coasting', that is, when there is little to no engine thrust. The acceleration SRS shown in Table 5.4a combines the loads from Electron at low frequencies and Vega-C at high frequencies, and these loads are applied along all three axes simultaneously. However, using this acceleration SRS resulted in extremely high stresses, as discussed further in Appendix A. It was not clear whether these input loads were too conservative when used in the analysis, and testing of a physical model would be necessary in the future. A workaround was needed, and as mentioned earlier in Chapter 4, the EXOpod Nova dispenser could significantly reduce the input shock loads on the CubeSat. Hence, the acceleration SRS from Figure 4.6 was approximated to give the values shown in 5.4b, and these were used instead.

## 5.3. Setup

### 5.3.1. Geometry Idealisation

The CAD model developed in Chapter 4 could not simply be imported into ANSYS. This was because of the presence of the subsystem components within the model, which would increase the complexity of the FE model and require more computational resources. Moreover, as these components were non-structural, the stresses within them were not of interest in the study. Hence, it was sufficient to represent the influence of these components using point mass elements (MASS21), and each of them had three translational and three rotational degrees of freedom. As the five internal bus components were connected to each other, it was decided to group them together as a single component to avoid defining too many point masses. As shown in Table 5.5, a total of seven properties are required for each component, namely, the mass, the three coordinates of its CG with respect to the origin, and the three mass MOI with respect to axes passing through the origin.

**Table 5.4:** Input shock loads

**(a)** Original

| Frequency [Hz] | Acceleration SRS [$g$] |
|---|---|
| 100 | 50 |
| 1,000 | 1,500 |
| 10,000 | 1,500 |

**(b)** Reduced

| Frequency [Hz] | $X$ acceleration SRS [$g$] |
|---|---|
| 100 | 50 |
| 10,000 | 1,500 |
| **Frequency [Hz]** | **$Y$ acceleration SRS [$g$]** |
| 100 | 50 |
| 300 | 200 |
| 10,000 | 500 |
| **Frequency [Hz]** | **$Z$ acceleration SRS [$g$]** |
| 100 | 50 |
| 200 | 100 |
| 10,000 | 500 |

An important assumption to consider is how the point masses are connected to the rest of the geometry. In ANSYS, such connections were created using MPC elements (MPC184), which allow relationships to be defined between several nodes simultaneously. Depending on the behaviour of independent and dependent nodes as shown in Figure 5.4, MPCs are classified into two types, namely, RBE2 and RBE3, which have infinite stiffness and zero stiffness, respectively. As the solar panels and patch antennae were relatively thin structures which would deform easily, their MPCs with the holes of the side frames were set as RBE3. However, the payload was so stiff that it was unlikely to deform significantly, which is why its MPCs with the payload mount were set as RBE2. Similarly, the internal bus was also stiff, and its MPCs with the guide rods were set as RBE2.

**Table 5.5:** Point mass properties

| Component | Mass [kg] | CG [mm] | | | Mass MOI [kg mm$^2$] | | |
|---|---|---|---|---|---|---|---|
| | | $X$ | $Y$ | $Z$ | $I_X$ | $I_Y$ | $I_Z$ |
| Payload | 1.035 | 0 | 0 | -126.51 | 20,077.21 | 20,077.21 | 545.22 |
| Internal Bus | 2.489 | -0.21 | -0.93 | 65.37 | 19,987.22 | 19,825.59 | 3,419.44 |
| Solar Panel | 0.146 | 0.01 | 50.75 | -0.75 | 1,623.44 | 1,327.50 | 456.25 |
| Solar Array (+$X$) | 0.438 | 54.35 | 0.02 | -0.05 | 4,162.32 | 5,215.61 | 1,540.78 |
| Solar Array (-$X$) | 0.438 | -54.35 | 0.02 | 0.05 | 4,162.32 | 5,215.61 | 1,540.78 |
| S-Band Antenna | 0.115 | 0 | -52.65 | 113.50 | 1,891.04 | 1,636.57 | 383.54 |
| X-Band Antenna | 0.053 | 0 | -51.53 | -113.50 | 865.53 | 754.77 | 170.79 |

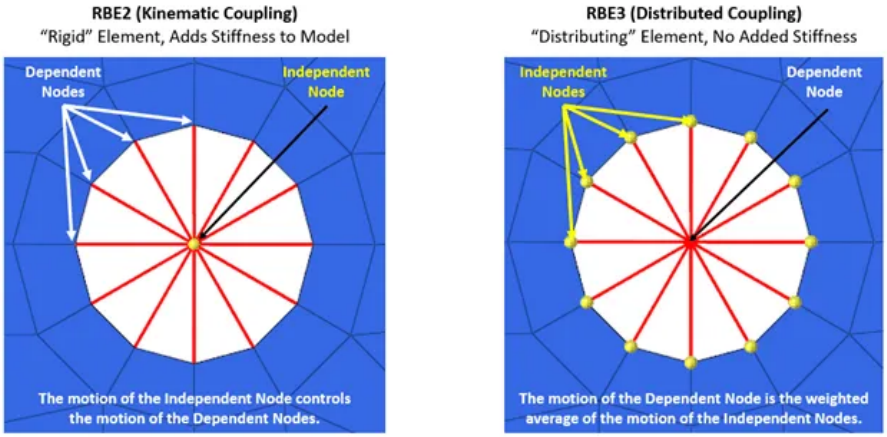


**Figure 5.4:** Types of MPCs [80]

Another simplification was made to the screws and the guide rods to further reduce the complexity of the model. These components were converted to line bodies and discretised using Timoshenko beam elements (BEAM189) having circular cross-sections with a diameter of 3 mm. These elements have quadratic displacement behaviour and consist of three nodes, with three translational and three rotational degrees of freedom at each node. While the element size of the guide rods was 1 mm, the screws had a much smaller value of 0.2 mm, given their short lengths. The guide rods were split into multiple sections corresponding to where they would be attached to the end frames and in contact with the payload mount. These sections were then connected using fixed joints to the holes of the end frames, and cylindrical joints to the holes of the payload mount. As each screw head has a diameter of 6 mm, its area was projected on the surfaces of the side frames, and all nodes of this were connected using fixed joints to the node representing the screw head. The node corresponding to the other end of the screw was connected using fixed joints to the circular edge of the hole. The washers themselves were not modelled, but their areas were projected on the surfaces of the $+Z$ end frame and the payload mount. Just like the point masses, MPCs were once again used for all these joints and were set as RBE3 so that the circular holes could stretch and deform, just as they would in reality.

ANSYS allows five types of contact formulations shown in Table 5.6, which can be applied as contact elements (CONTA174 and TARGE170) between the surfaces of different components. Among these, only the first two are linear contacts and solve within one iteration, as the contact area remains constant during the analysis. The remaining three are non-linear contacts and require multiple iterations to solve, along with higher chances of non-convergence errors occurring. While the bonded contact is the least computationally expensive, it also constrains the surfaces unrealistically due to the absence of sliding. The no separation contact, despite allowing sliding, would still constrain the surfaces when they need to separate, thus resulting in unnecessary stresses. Hence, for the present analyses, all contacts were set to be frictionless, and these were applied to the surfaces where the side frames were in contact with the end frames and the payload mount.

**Table 5.6:** Types of contacts

| Type | Normal behaviour (Separation) | Tangential behaviour (Sliding) |
|---|---|---|
| Bonded | No | No |
| No separation | No | Yes ($\mu$ = 0) |
| Frictionless | Yes | Yes ($\mu$ = 0) |
| Rough | Yes | No ($\mu$ = ∞) |
| Frictional | Yes | Yes (0 < $\mu$ < ∞) |

Apart from the screws and the guide rods, the geometries of the remaining primary structure components were meshed with solid tetrahedral elements (SOLID187) to discretise their complex shape effectively, as shown in Figure 5.5. These elements have quadratic displacement behaviour and consist of ten nodes, with three translational degrees of freedom at each node. The end frames, the side frames, and the payload mount were each assigned different element sizes of 1.2 mm, 1.6 mm, and 1.6 mm, respectively. Certain regions of the mesh, such as those around load-bearing holes and at the boundaries between different components, were refined locally to further improve accuracy. The total number of nodes and elements in the mesh was 1,036,129 and 621,928, respectively, and a mesh convergence study was performed as described in Appendix B. ANSYS also provided an option to check the average quality of the elements, taking into consideration various parameters such as skewness, aspect ratio, and orthogonal quality. A value close to 1 indicates a high-quality mesh, while a value close to 0 indicates that the mesh needs to be significantly improved before proceeding further. The present mesh yielded a result of 0.79, indicating that it was of sufficient quality. Finally, the material properties in Table 4.1 were assigned to all the components of the primary structure, and their behaviour was assumed to be isotropic.

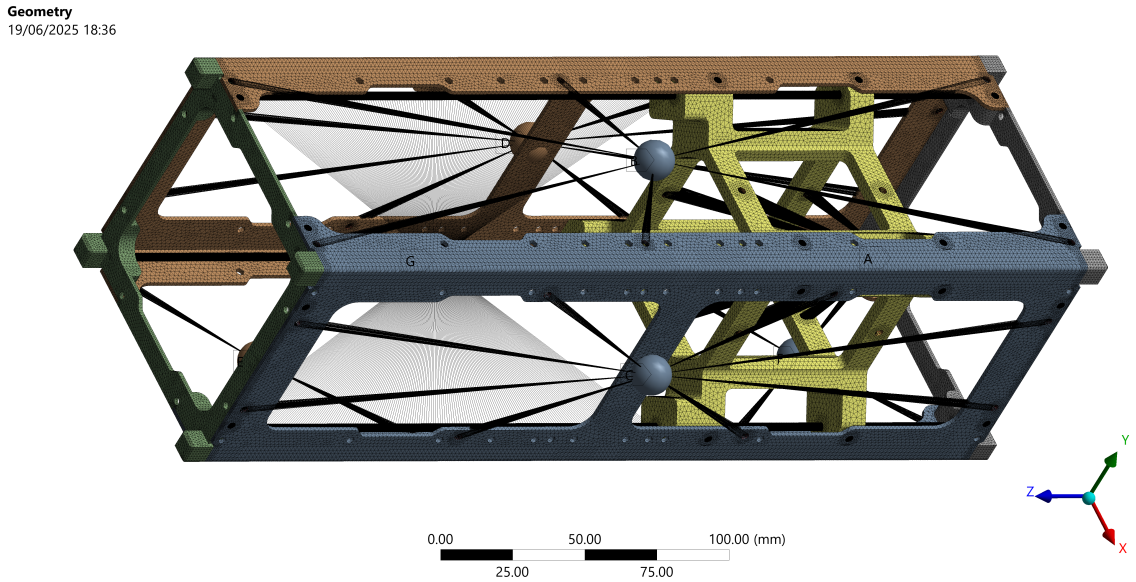


**(a)** View from $+X$, $+Y$, $+Z$

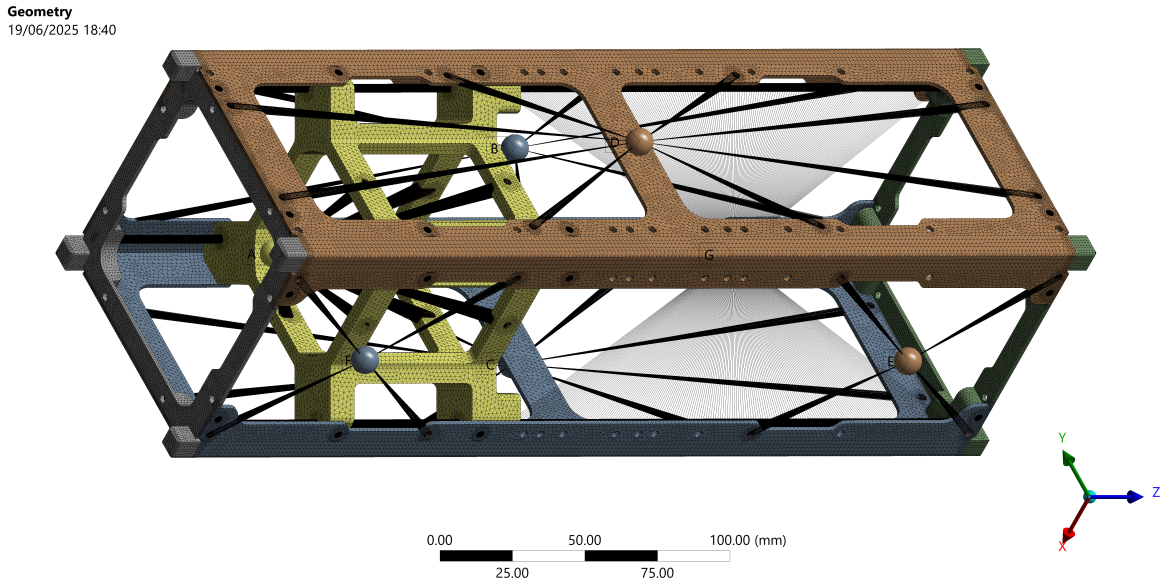


**(b)** View from $-X$, $-Y$, $-Z$

**Figure 5.5:** Point masses and meshed geometry

### 5.3.2. Boundary Conditions

All of the load cases described earlier involve the CubeSat placed within the closed EXOpod Nova dispenser, and the boundary conditions applied to the FE model are determined by how the dispenser constrains the CubeSat. Although it is a rail-type dispenser, it makes use of a unique clamping mechanism that grips the CubeSat and prevents its movement along all three axes. As shown in Figure 5.6, certain external surfaces of the side frames and end frames that would be in contact with the interior of the dispenser were locked in their respective normal directions but still free to move in their tangential directions. Despite being simpler, fully fixed supports were not used on those surfaces to avoid over-constraining the model and also because no such joint between the CubeSat and the dispenser interior exists in reality.

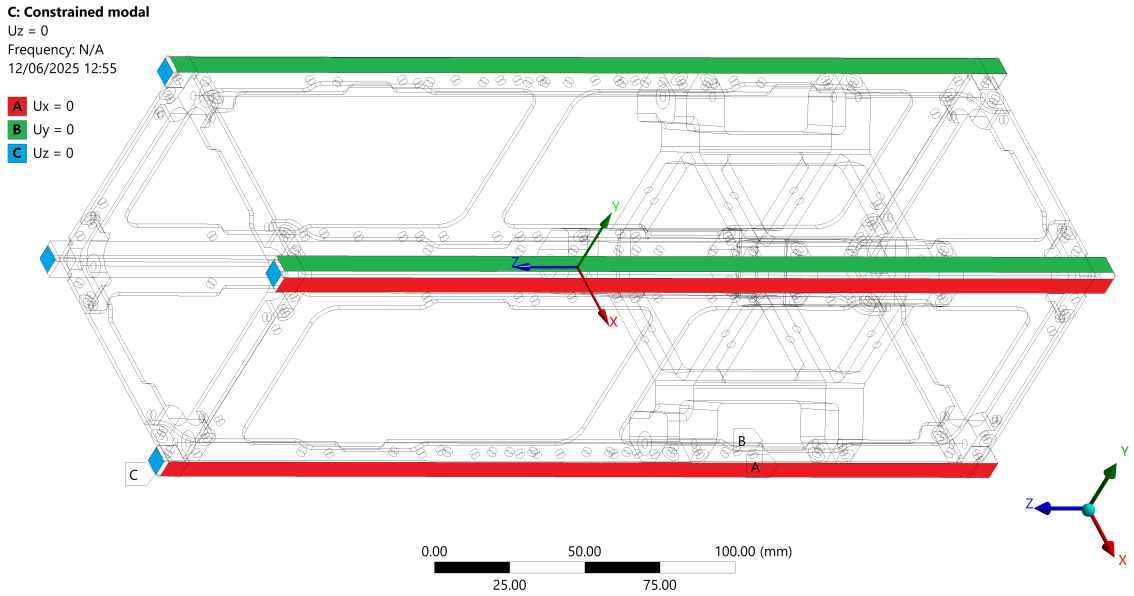


**Figure 5.6:** Dispenser boundary conditions

Before performing the analyses for each load type, it is important to check the FE model to ensure that the results obtained later on will be trustworthy. In the context of the present work, only the most important checks are carried out, which are specific to spacecraft structural design [81] and are elaborated in Appendix D.

## 5.4. Results and Discussion

### 5.4.1. Quasi-Static Loads

The accelerations of each of the eight load cases described in Table 5.3 were applied to all components in the model. Upon doing so, the maximum von-Mises stress obtained in each case is shown in Table 5.7, and they all have values between 18 MPa and 21 MPa. The corresponding $MOS$ values for these stresses were also calculated, and these were all found to be positive, indicating that the CubeSat withstands the quasi-static loads. As shown in Figure 5.7, the maximum stresses were seen around the screw holes where the $\pm X$ faces of the side frame are connected to the end frames. The main reason behind this could be attributed to the presence of the deployable solar arrays on the $\pm X$ faces of the side frames. As they have a relatively high mass, they pulled on the side frames under the acceleration loads, causing the large deformations.

**Table 5.7:** Quasi-static loads results

| Case | $\sigma_{vm,max}$ [MPa] | $MOS$ |
|---|---|---|
| 1 | 19.10 | 10.54 |
| 2 | 20.06 | 9.99 |
| 3 | 20.08 | 9.97 |
| 4 | 19.95 | 10.05 |
| 5 | 18.62 | 10.83 |
| 6 | 18.31 | 11.04 |
| 7 | 20.12 | 9.95 |
| 8 | 19.73 | 10.17 |

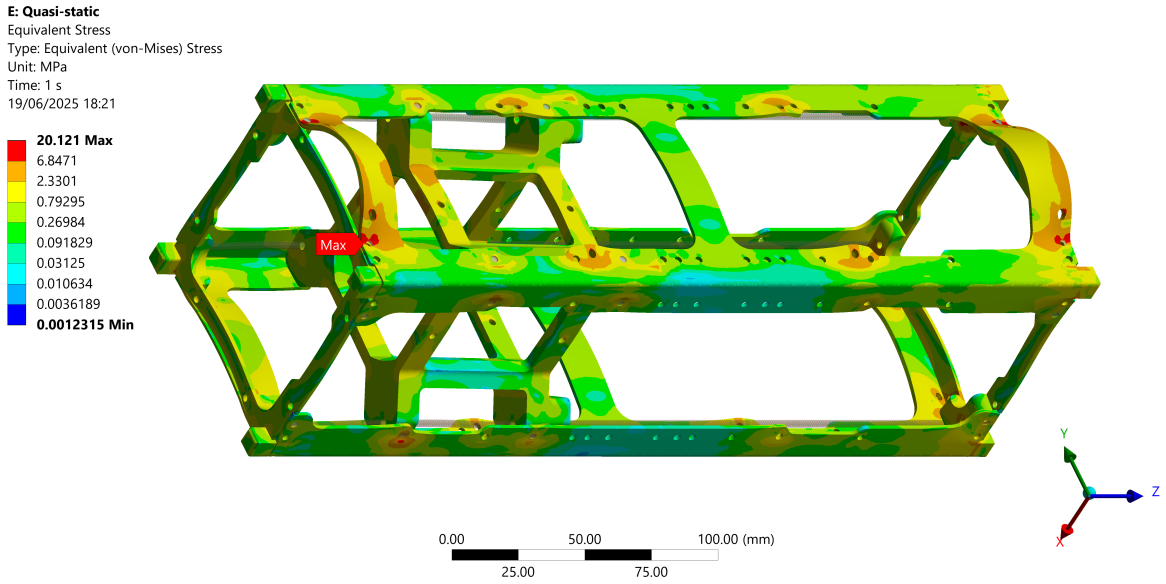


**(a)** Stress

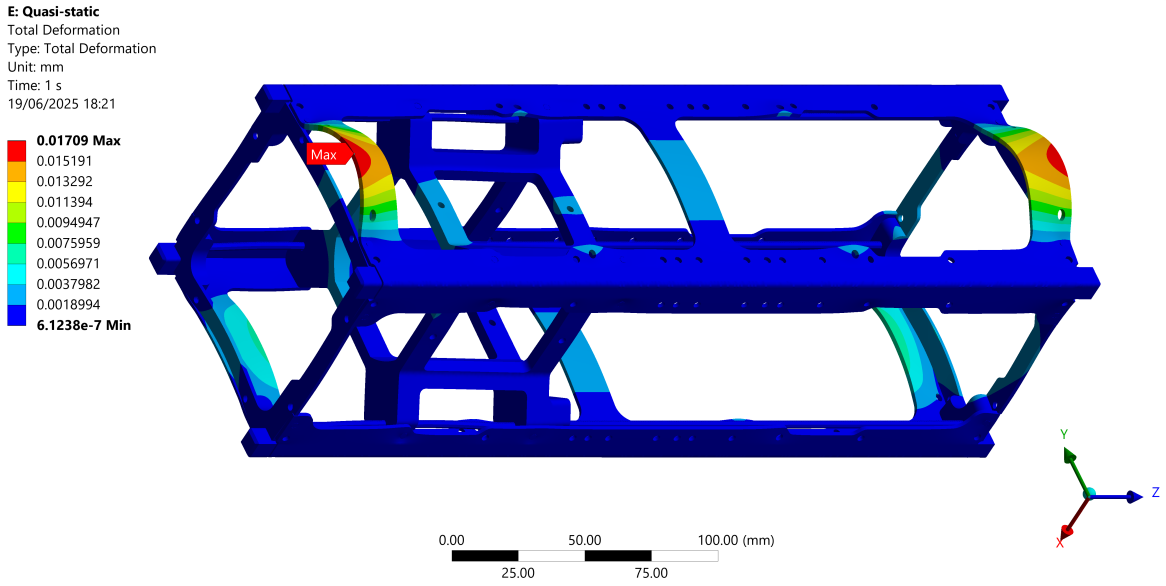


**(b)** Total deformation

**Figure 5.7:** Quasi-static loads results of maximum stress case

### 5.4.2. Modal Analysis

ANSYS is incapable of performing a modal analysis when there are non-linear contacts, and hence, all the frictionless contacts were automatically changed to no separation. The first ten natural frequencies of the CubeSat are shown in Table 5.8, while Figure 5.8 showcases some of the first few mode shapes. Clearly, these were all above the minimum requirement of 115 Hz, implying that resonance between the CubeSat and the launch vehicle is unlikely. These frequencies were also significantly higher than those of the six educational CubeSats discussed in Chapter 2. From the first two mode shapes having effective mass fractions of 36.83% and 35.50%, respectively, it can be seen that these are primarily due to the deformation of the payload mount, and this was expected because of the high mass of the payload. The fourth mode shape had an effective mass fraction of 27.21%, showed deformations on the $\pm X$ faces of the side frames, and this was due to the deployable solar arrays. A total of 99 modes were obtained from the range of 0 Hz to 10,000 Hz, and all these were used as input for the random vibration and shock loads analyses.

**Table 5.8:** CubeSat natural frequencies

| Mode | Frequency [Hz] |
|---|---|
| 1 | 822.69 |
| 2 | 830.02 |
| 3 | 901.29 |
| 4 | 906.85 |
| 5 | 1,361.55 |
| 6 | 1,361.60 |
| 7 | 1,518.25 |
| 8 | 1,541.10 |
| 9 | 1,562.22 |
| 10 | 1,605.62 |

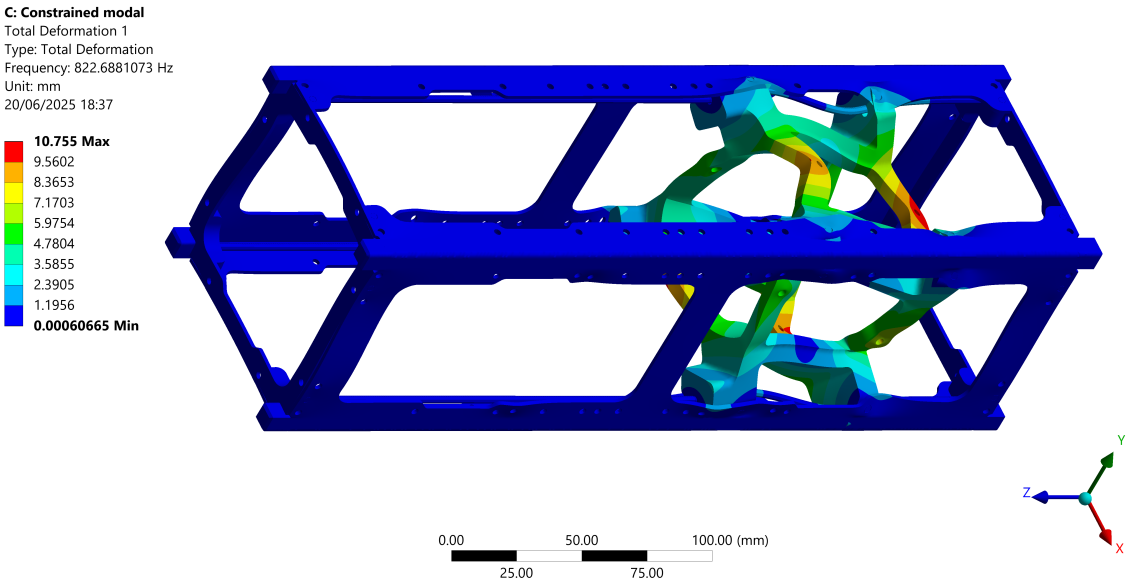


**(a)** First mode

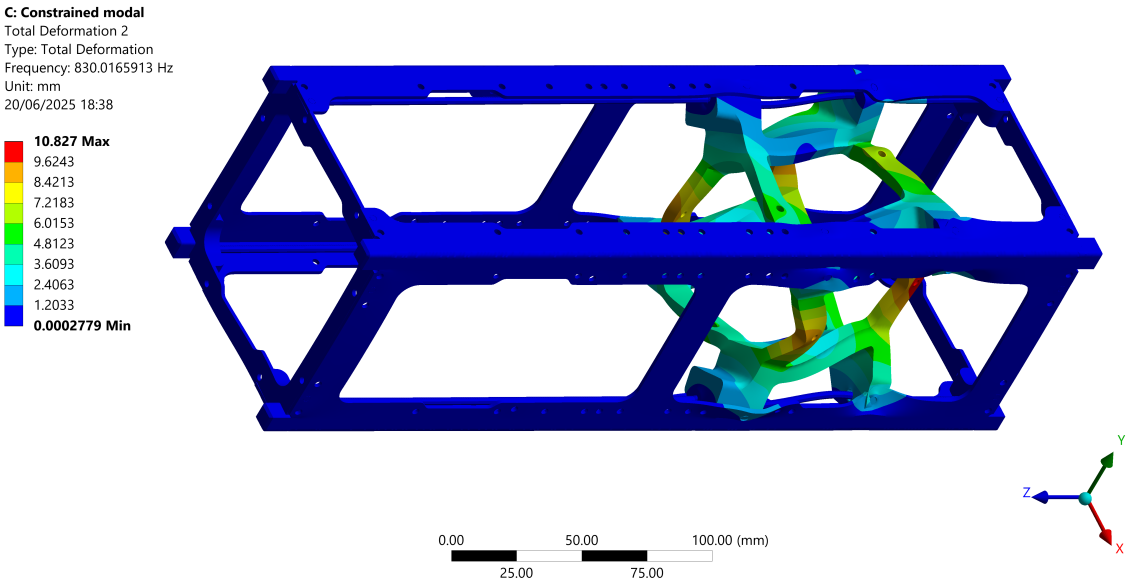


**(b)** Second mode

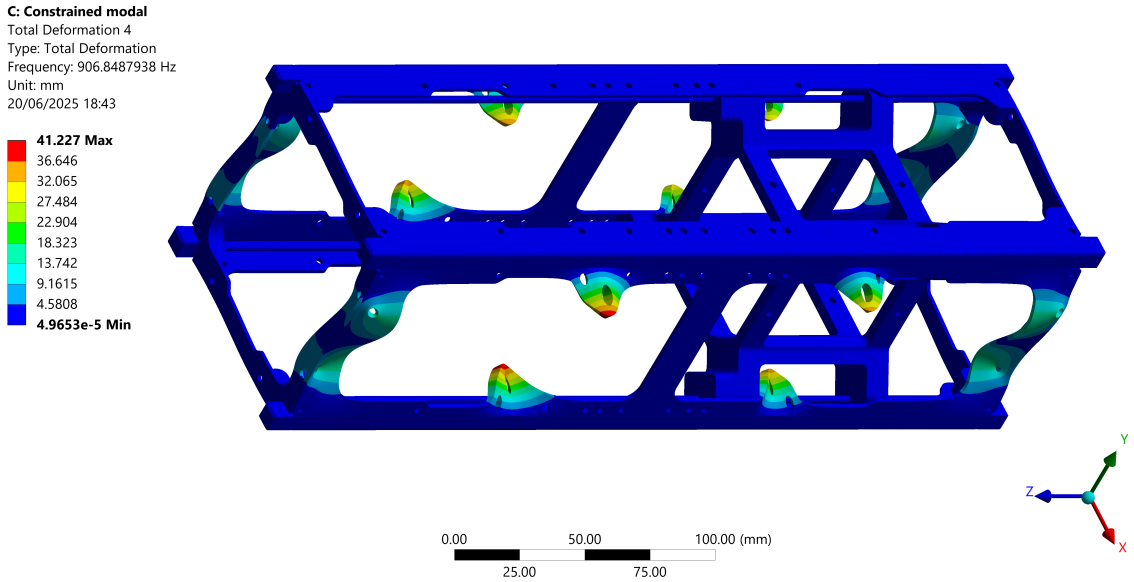


**(c)** Fourth mode

**Figure 5.8:** Mode shapes

### 5.4.3. Random Vibrations

The acceleration PSD of Ariane 6 was applied along all three axes simultaneously, and a $\zeta$ of 0.05 was assumed. As the input loads are defined in terms of a Gaussian distribution, the results would also be according to this distribution. While interpreting these results, it is necessary to specify the standard deviation level. A 1-sigma level represents a 68.27% probability, a 2-sigma level represents a 95.45% probability, and a 3-sigma level represents a 99.73% probability that the stresses or deformations in reality will be below the values observed in the FE analysis. In the case of spacecraft design, the 3-sigma level of the results is found to be sufficient, as shown in Figure 5.9. The highest stresses were seen at the four attachment points of the guide rods with the $+Z$ end frame, and the maximum von-Mises stress among these four regions was 53.84 MPa. These stresses could be attributed to the load transfer from the internal bus, which had a significant mass, to the guide rods. The value of $MOS$ was calculated as 3.09, indicating that the CubeSat withstands the random vibrations.

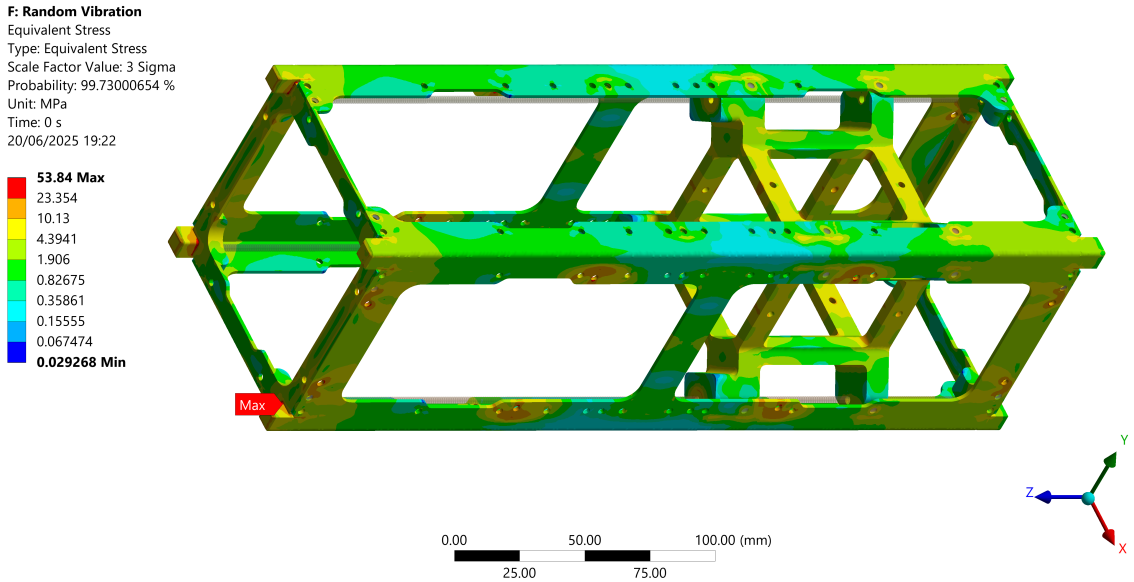


**(a)** Stress

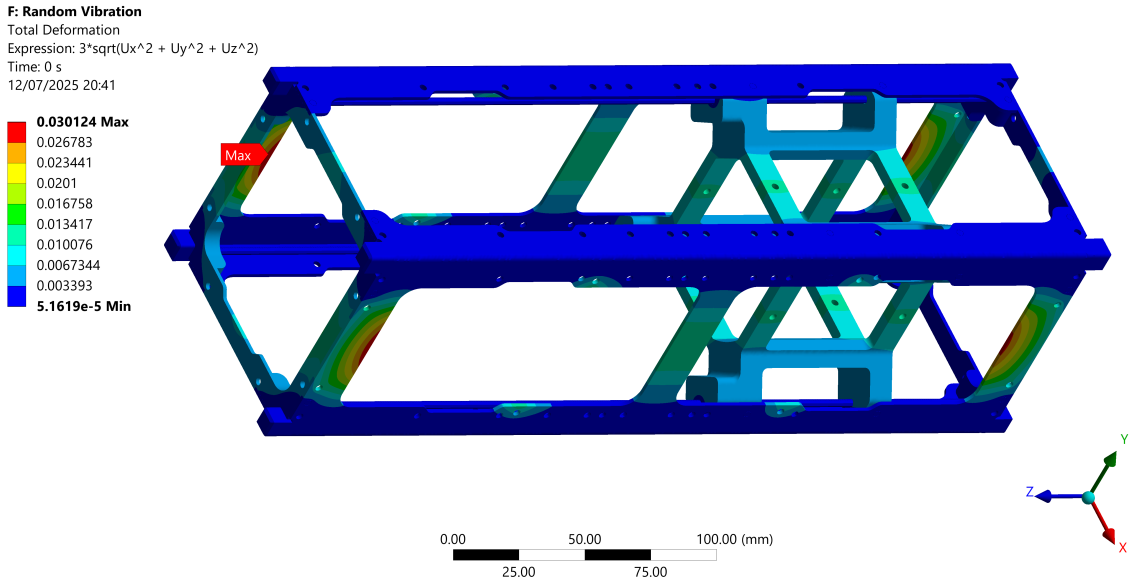


**(b)** Total deformation

**Figure 5.9:** Random vibrations results

### 5.4.4. Shock Loads

The reduced acceleration SRS described in Table 5.4b was applied along all three axes simultaneously, and a $\zeta$ of 0.05 was assumed once again. As shown in Figure 5.10, the highest stresses were seen on the portions of the side frames where they were in contact with the $+Z$ end frame. Similar to the case of the random vibrations, there was a load transfer from the internal bus to the guide rods, and then to the $+Z$ end frame. As a result, there were eight regions where the side frames were compressed by the $+Z$ end frame on one side and the dispenser boundary conditions on the other. The maximum von-Mises stress among these eight regions was 194.96 MPa, and the corresponding $MOS$ was calculated as 0.13. Hence, while the CubeSat does withstand the shock loads, it is evident that these loads are the most damaging.

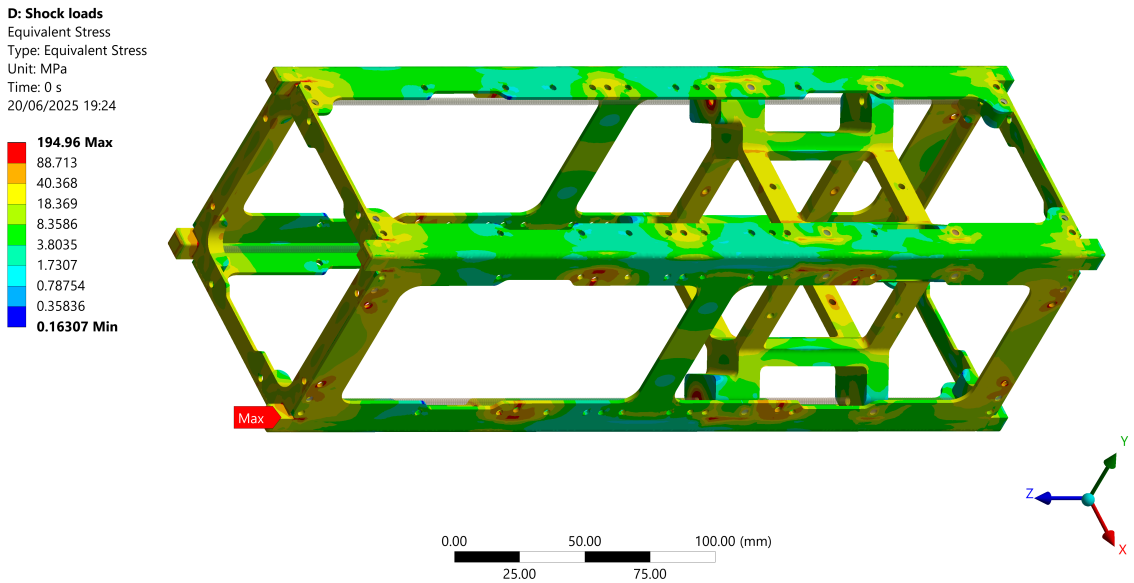


**(a)** Stress

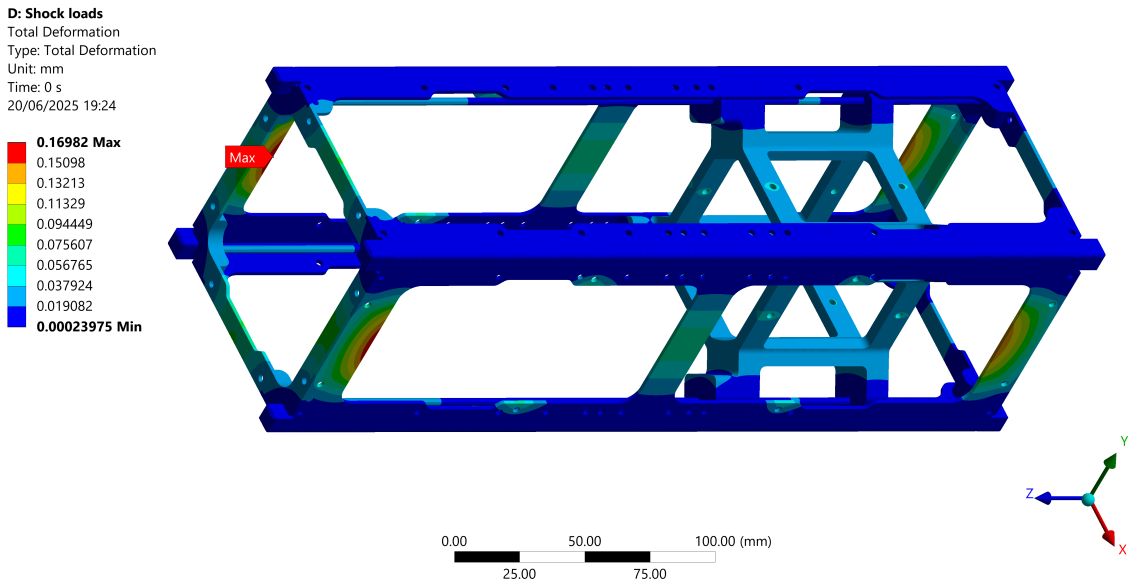


**(b)** Total deformation

**Figure 5.10:** Shock loads results

## 5.5. Sensitivity Analysis

### 5.5.1. Preliminary Information

A sensitivity analysis is the study of how the uncertainty in the output of a model can be attributed to different sources of variation in the input of a model. To accomplish this, variance-based methods are commonly used, which quantify the proportion of the output variance caused by a random input variable [82]. A model with an output variable $Y$ is assumed to be a function of a given set of $m$ random input variables $X_i$, defined as:

$$Y = f(X_1, X_2, X_3, \ldots, X_m)$$

The first order sensitivity indices $S_i$ are defined as follows, where $V(Y)$ is the unconditional variance of $Y$, and $V(Y|X_i)$ is the variance of $Y$ caused by a variation of $X_i$ only:

$$S_i = \frac{V(Y|X_i)}{V(Y)}$$

As the first order sensitivity indices measure only the decoupled influence of each variable, the total effect sensitivity indices $S_{Ti}$ were introduced. These are defined as follows, where $V(Y|X_{\sim i})$ is the variance of $Y$ caused by all the input variables excluding $X_i$:

$$S_{Ti} = 1 - \frac{V(Y|X_{\sim i})}{V(Y)}$$

The first step in performing a sensitivity analysis in optiSLang is setting up the design of experiments, where sets of input variables are sampled across the design space. Deterministic design exploration approaches, such as Full Factorial Sampling and Central Composite Sampling, are based on a regular arrangement of values of the input variables, but have the disadvantage of requiring an increasing number of samples as the number of variables increases. In contrast to these, stochastic design exploration approaches such as Monte Carlo Sampling and Latin Hypercube Sampling assume variables that follow a continuous distribution between given upper and lower bounds. However, Monte Carlo Sampling, being completely random, can lead to clusters or holes in the sampling set, resulting

in undesired correlations between the input variables. To overcome these issues, Latin Hypercube Sampling, with input variables following a uniform distribution, was used for the sensitivity analyses in the present work.

The values of the output variable are then determined for each sample of input variables using the FE analyses in ANSYS. Once complete, a metamodel is created that approximates the output variable as a function of the input variables, based on techniques such as Moving Least Squares. The metamodel with the highest forecast quality, characterised by a Coefficient of Prognosis ($CoP$) value close to 100%, is known as the Metamodel of Optimal Prognosis (MOP). In other words, the MOP represents the best possible description of the behaviour between the input variables and the output variable [82]. It is important to note that interactions between the input variables are automatically taken into account in the MOP. In this way, the variance contribution of a single input variable is given by the product of the $CoP$ from the MOP and the total effect sensitivity index of that particular variable estimated from the MOP:

$$CoP(X_i) = CoP \times S_{Ti}$$

### 5.5.2. Full Model

Due to the importance of the first natural frequency of the CubeSat, this was chosen as an output parameter of the sensitivity analysis. Given the uncertainty in the material properties, which are $E$, $\nu$, and $\rho$ of Aluminium and Steel, these were chosen as input parameters. As mentioned earlier, the first natural frequency was mainly due to the motion of the payload and the payload mount. As the payload was still being developed, its mass was also not finalised, and this was also taken as an input parameter. Assuming the payload has a uniform density while its mass changes, it was observed that the CG remains the same, while the three MOI properties change by the same proportion. This was because of the shape of the payload that made it symmetric about the $XZ$ and $YZ$ planes, and its specific location within the CubeSat that resulted in its CG on the $Z$ axis. A variation of ±10% from their baseline values was considered for all these parameters as shown in Table 5.9, and a total of 100 samples were taken.

**Table 5.9:** Parameters variation for full model

| Parameter | Baseline value | Range considered |
|---|---|---|
| Aluminium $E$ [GPa] | 70 | 63 – 77 |
| Aluminium $\nu$ | 0.32 | 0.288 – 0.352 |
| Aluminium $\rho$ [kg/m$^3$] | 2,810 | 2,529 – 3,091 |
| Steel $E$ [GPa] | 200 | 180 – 220 |
| Steel $\nu$ | 0.28 | 0.252 – 0.308 |
| Steel $\rho$ [kg/m$^3$] | 7,930 | 7,137 – 8,723 |
| Payload mass [kg] | 1.035 | 0.9315 – 1.1385 |

The statistics of the first frequency values from this sensitivity analysis are shown in Table 5.10, while its sensitivities with respect to the seven parameters are shown in Figure 5.11. It can be observed that only the Aluminium $E$ and the payload mass have a significant influence on the first frequency, while the other five parameters have almost negligible influence. Furthermore, both the Aluminium $E$ and the payload mass have almost the same relative contribution to the variance of the first frequency.

**Table 5.10:** Statistics of first frequency for full model

| Parameter | Frequency [Hz] |
|---|---|
| Baseline value | 822.69 |
| Range obtained | 753.06 – 893.25 |
| Mean value | 823.37 |
| Standard deviation | 33.30 |

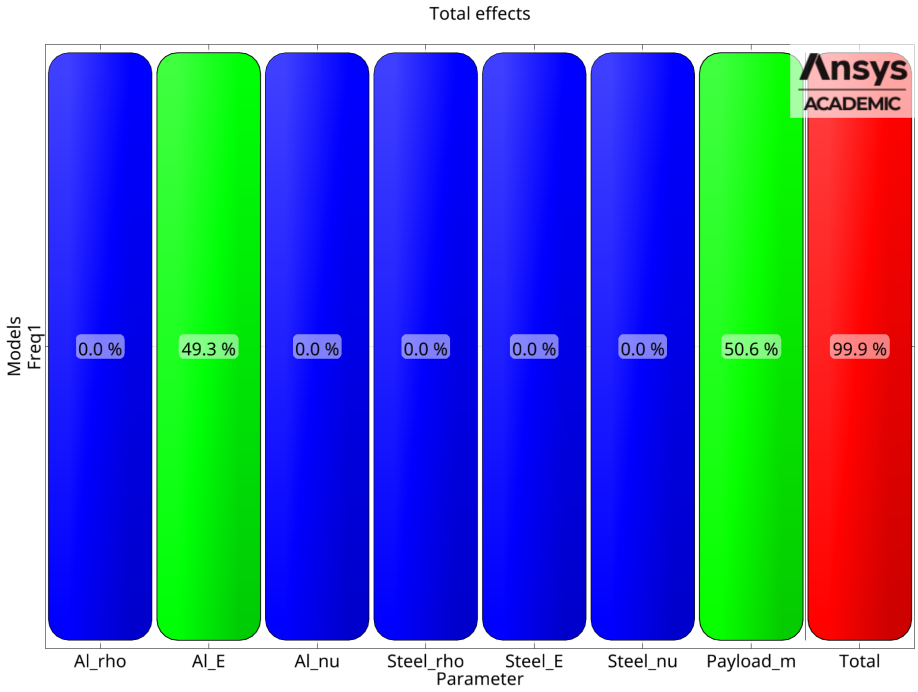


**Figure 5.11:** $CoP$ matrix of first frequency for full model

The response surface approximation of the first frequency with respect to the Aluminium $E$ and payload mass values is shown in Figure 5.12. It can be seen that there is a strong linear relationship between the first frequency with both the Aluminium $E$ and the payload mass. Furthermore, the frequency increases when the Aluminium $E$ increases or when the payload mass decreases. This trend was expected as natural frequencies are usually directly proportional to stiffness but inversely proportional to mass.

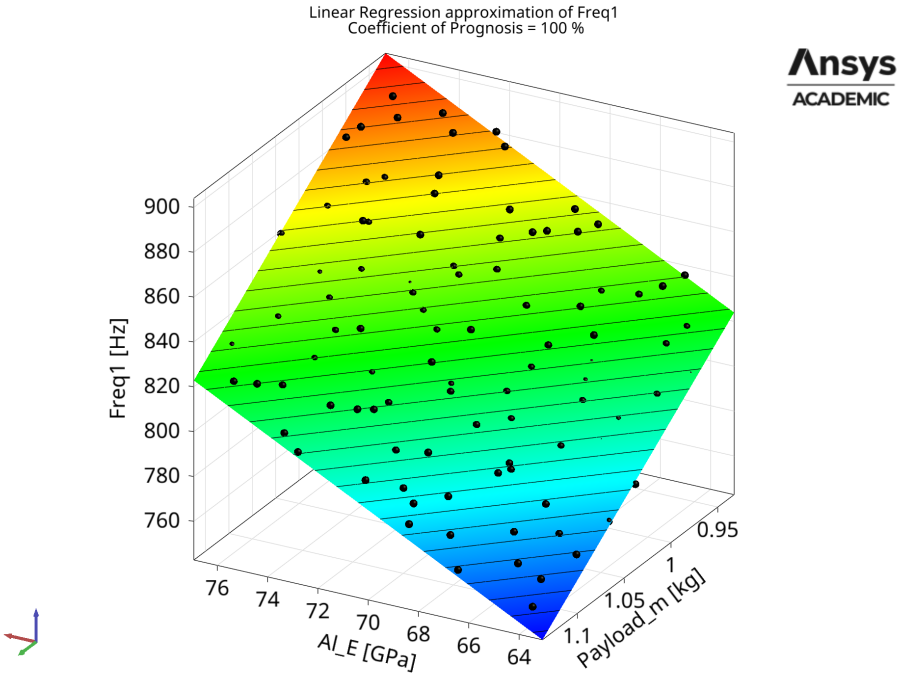


**Figure 5.12:** Response surface of first frequency for full model

### 5.5.3. Standalone End Frame

Apart from just the first natural frequency, the von-Mises stress from the shock loads was also important, as this type of load was the most damaging. However, as the shock load analysis required the modal analysis as a prerequisite, performing the sensitivity analysis for the full model was not feasible. This was because, even for a single sample, performing the modal analysis from 0 Hz to 10,000 Hz and then the shock loads analysis took approximately half an hour to complete and also required a large amount of memory storage.

Hence, it was decided to consider a standalone component for performing the modal analysis and the shock load analysis. Although not completely representative of the full model, such an analysis would still be useful for understanding trends in the results. Among the different components of the primary structure, it was decided to proceed with the end frame for a few reasons. Firstly, the boundary conditions of the dispenser could be applied to the external surfaces of the corner regions of the end frame. Secondly, this component was smaller compared to the side frames and the payload mount, and its mesh uses fewer nodes and elements. Thirdly, the maximum stress in this component from the shock loads was 186.23 MPa, which was only slightly lower than that of the side frame.

The input parameters being considered were the three material properties of Aluminium, along with the thickness of the end frame and the damping ratio $\zeta$ used for the shock loads analysis. A variation of 10% was assumed for the material properties, similar to the case of the full model, but the thickness and $\zeta$ were varied by 12.5% and 20%, respectively. The ranges of all these parameters are shown in Table 5.11, and a total of 100 samples were taken once again. The first frequency and the average von-Mises stress in the model were taken as output parameters. The maximum von-Mises stress was not considered, as these might arise due to a stress singularity or local effects in the mesh, which would reduce the accuracy of the metamodel. For the baseline parameters case, a total of 16 modes were obtained in the frequency range of 0 Hz to 10,000 Hz, and these were used for the shock loads analysis where the reduced acceleration SRS in Table 5.4b was applied.

**Table 5.11:** Parameters variation for standalone end frame

| Parameter | Baseline value | Range considered |
|---|---|---|
| Aluminium $E$ [GPa] | 70 | 63 – 77 |
| Aluminium $\nu$ | 0.32 | 0.288 – 0.352 |
| Aluminium $\rho$ [kg/m$^3$] | 2,810 | 2,529 – 3,091 |
| Thickness [mm] | 1.6 | 1.4 – 1.8 |
| Damping ratio $\zeta$ | 0.05 | 0.04 – 0.06 |

The statistics of the first frequency and average von-Mises stress from this sensitivity analysis are shown in Table 5.12, while their sensitivities with respect to the five parameters are shown in Figure 5.13. The thickness of the end frame has the highest influence on the first frequency, while the Aluminium $E$ and $\rho$ have moderately high but nearly equal contributions. Just like in the case of the full model, the Aluminium $\nu$ had very little contribution, while $\zeta$ had zero contribution as the modal analysis was undamped. For the average von-Mises stress, the Aluminium $\rho$ showed the highest influence, followed by the Aluminium $E$ and the thickness.

**Table 5.12:** Statistics of first frequency and average stress for standalone end frame

| Parameter | Frequency [Hz] | $\sigma_{vm,avg}$ [MPa] |
|---|---|---|
| Baseline value | 2,327.58 | 1.6708 |
| Range obtained | 1,970.47 – 2,684.45 | 1.5031 – 1.8323 |
| Mean value | 2,319.58 | 1.6699 |
| Standard deviation | 165.81 | 0.0805 |

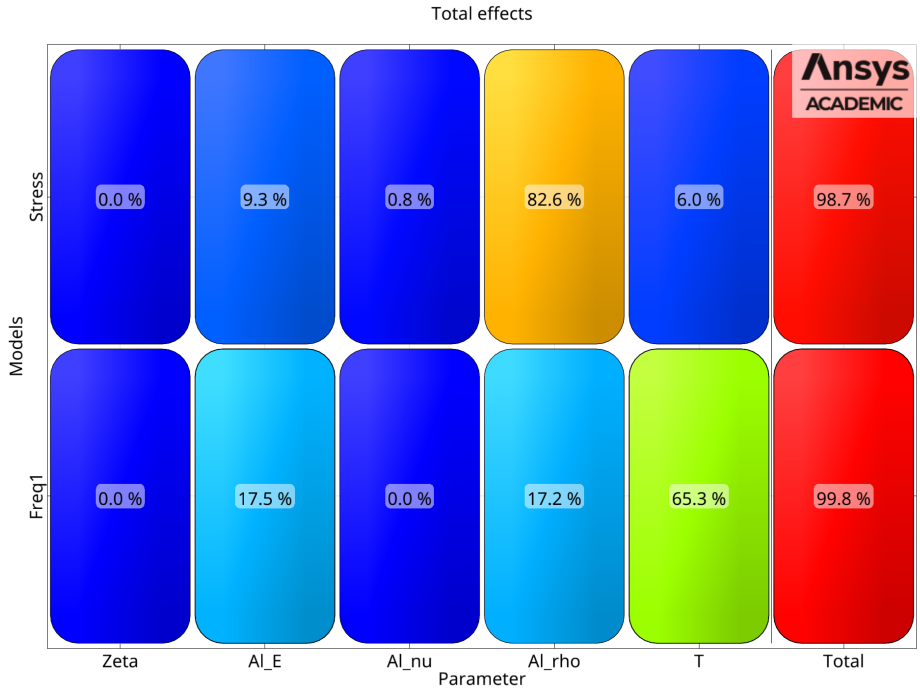


**Figure 5.13:** $CoP$ matrix of first frequency and average stress for standalone end frame

The response plot approximation of the first frequency with respect to the thickness, the Aluminium $E$ and $\rho$ are shown in Figure 5.14. It can be observed that the first frequency increases when either the thickness or the Aluminium $E$ increases, or when the Aluminium $\rho$ decreases. An increase in thickness leads to both an increase in stiffness and mass, but the increase in stiffness dominates, thus leading to an increase in the frequency. Similarly, an increase in the Aluminium $E$ causes an increase in stiffness, while a decrease in the Aluminium $\rho$ causes a decrease in the mass, and both lead to an increase in the frequency.

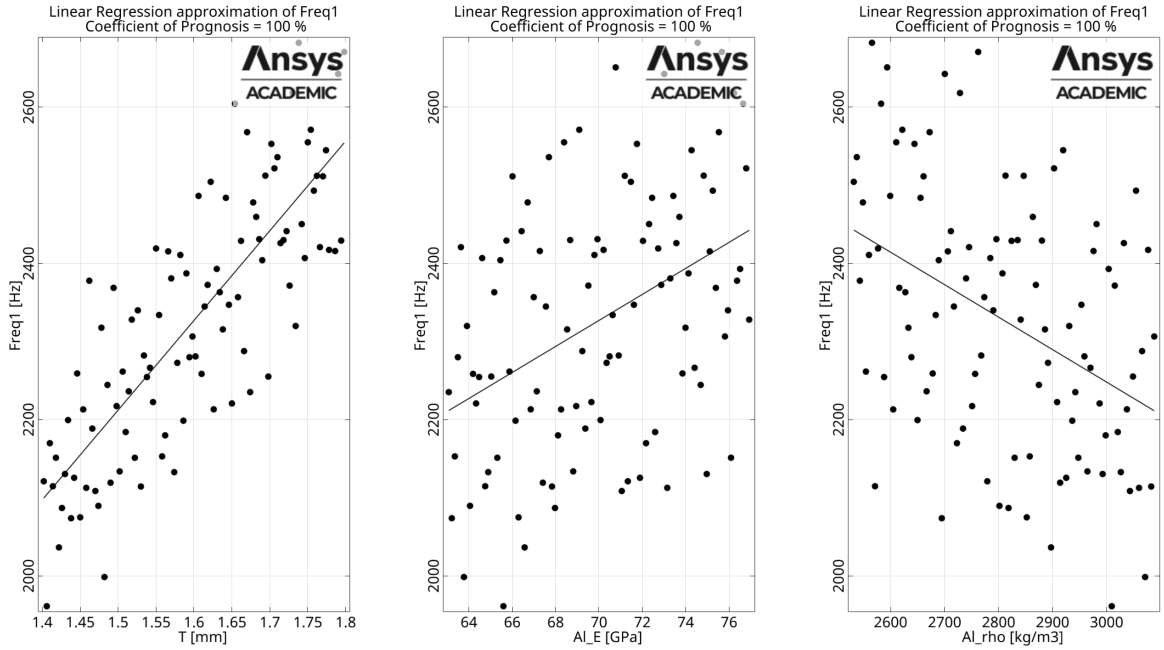


**(a)** Thickness **(b)** Young's modulus **(c)** Density

**Figure 5.14:** Response plots of first frequency for standalone end frame

The response plot approximation of the average von-Mises stress with respect to the thickness, the Aluminium $E$ and $\rho$ are shown in Figure 5.15. It can be observed that the stress increases when an increase is made to each of these three parameters. Furthermore, a common trend among these three parameters was that as the first frequency increased, the total number of modes in the frequency range of 0 Hz to 10,000 Hz decreased, and vice versa.

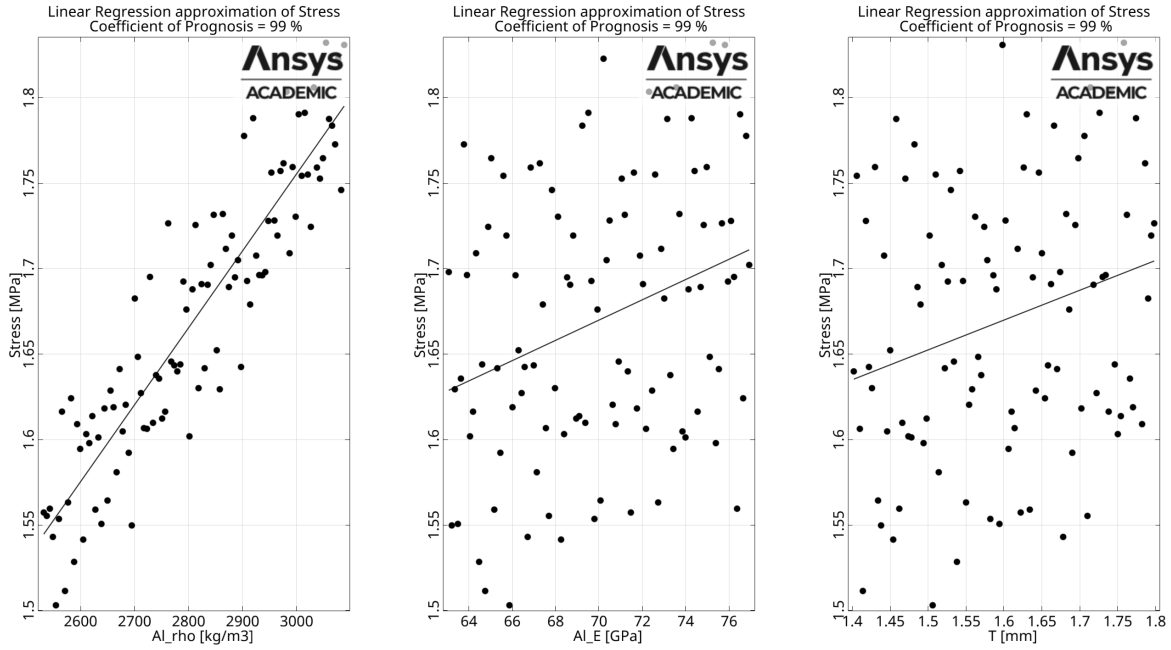


**(a)** Density **(b)** Young's modulus **(c)** Thickness

**Figure 5.15:** Response plots of average stress for standalone end frame

## 5.6. Model Calibration

The costs involved in the development or procurement of a physical model of the CubeSat primary structure and the time required to do so were not found to be in agreement with the research timeline. As a result, validation of the FE analyses in an experimental setup could not be performed. Hence, it was decided to create synthetic experimental data through a separate FE analysis and use those results to perform a calibration study.

The full model of the CubeSat was considered along with the input parameters in Table 5.9. Just like before, a variation of 10% was considered in their baseline values, and a random value within that range for each of them was determined. These are referred to as oracle input parameters and would be used to generate the synthetic experimental data. After all, this would be representative of an actual experiment, where the input parameters would be unknown and slightly differing from their baseline values. A modal analysis determining the first six natural frequencies using the oracle input parameters was performed, and these values are compared with the baseline frequencies in Table 5.13.

In order to quantify the difference between the FE analysis frequencies with the oracle frequencies, an objective function $F$ was formulated. In this, $f_{i,num}$ is the frequency of the $i^{\text{th}}$ mode from the FE analysis, while $f_{i,exp}$ is the frequency of the $i^{\text{th}}$ mode from the synthetic experimental data. The initial value of $F$ obtained when comparing the baseline frequencies with the oracle frequencies was 0.2117.

$$F = \sum_{i=1}^{6} \frac{|f_{i,num} - f_{i,exp}|}{f_{i,exp}}$$

There exists a set of input parameters in the FE analysis which results in a value of $F$ close to zero, implying that the value of $F$ needs to be minimised in an optimisation setup. In optiSLang, the One-Click

Optimisation (OCO) method was used, which automatically and iteratively selects the most suitable optimisation algorithms. It performs this by exploring the design space to study the statistical features of the different values of $F$. This dynamic selection helps avoid local minima in $F$ that might occur with manual selection. The main setting to be input while using the OCO method was the maximum number of evaluations, and this was set as 125. The optimal parameters shown in Table 5.13 correspond to a minimum value of $F$ of 0.0224.

**Table 5.13:** Baseline, oracle, and optimal values comparison

| Parameter | Baseline value | Oracle value | Optimal value |
|---|---|---|---|
| Aluminium $E$ [GPa] | 70 | 72.18 | 72.60 (0.58%) |
| Aluminium $\nu$ | 0.32 | 0.3332 | 0.2992 (10.76%) |
| Aluminium $\rho$ [kg/m$^3$] | 2,810 | 2,625.21 | 2,679.76 (2.06%) |
| Steel $E$ [GPa] | 200 | 191.27 | 196.40 (2.64%) |
| Steel $\nu$ | 0.28 | 0.2946 | 0.2839 (3.71%) |
| Steel $\rho$ [kg/m$^3$] | 7,930 | 7,576.19 | 7,885 (3.99%) |
| Payload mass [kg] | 1.035 | 0.9816 | 0.9833 (0.17%) |
| First frequency $f_1$ [Hz] | 822.69 | 857.46 | 858.72 (0.15%) |
| Second frequency $f_2$ [Hz] | 830.02 | 864.98 | 866.36 (0.16%) |
| Third frequency $f_3$ [Hz] | 901.29 | 916.26 | 916.18 (0.01%) |
| Fourth frequency $f_4$ [Hz] | 906.85 | 921.90 | 921.82 (0.01%) |
| Fifth frequency $f_5$ [Hz] | 1,361.55 | 1,431.75 | 1,418.06 (0.96%) |
| Sixth frequency $f_6$ [Hz] | 1,361.60 | 1,431.80 | 1,418.11 (0.96%) |

It can be observed that all the resulting frequencies had a difference of less than 1% from the oracle frequencies. Among the input parameters, the Aluminium $E$ and the payload mass had the least difference with their oracle values, and this could be attributed to these parameters having a high influence on the value of $F$. The other five parameters showed much greater differences with their oracle values, especially the Aluminium $\nu$, but these could be because of their low influence on $F$.

As a further check, the seventh, eighth, ninth, and tenth frequencies using the optimal input parameters were also calculated as shown in Table 5.14. Upon comparing them with the corresponding oracle frequencies, the resulting difference between them was less than 1%, implying that the calibration approach was successful.

**Table 5.14:** Calibration check

| Parameter | Oracle value | Optimal value |
|---|---|---|
| Seventh frequency $f_7$ [Hz] | 1,544.43 | 1,542.58 (0.12%) |
| Eighth frequency $f_8$ [Hz] | 1,569.69 | 1,570.76 (0.07%) |
| Ninth frequency $f_9$ [Hz] | 1,590.96 | 1,592.03 (0.07%) |
| Tenth frequency $f_{10}$ [Hz] | 1,635.39 | 1,637.29 (0.12%) |

# 6

# Thermoelastic Analysis

## 6.1. Theory Notes

### 6.1.1. Thermoelastic Phenomenon

As mentioned earlier in Chapter 2, the CubeSat in orbit would experience thermal loads from a variety of sources. The input thermal loads due to solar radiation ($\dot{Q}_{solar}$), albedo from the Earth ($\dot{Q}_{albedo}$), infrared radiation from the Earth ($\dot{Q}_{earth\ infrared}$), and Joule heating from hardware components ($\dot{Q}_{generated}$) are balanced with the dissipation of infrared radiation by the CubeSat to deep space ($\dot{Q}_{deep\ space}$). Due to the thermal capacitance of the CubeSat, some of the heat is stored internally, which is seen as a temperature increase. Assuming the CubeSat to be a lumped model, having a mass $m$, specific heat capacity $c$, and a uniform instantaneous temperature $T$, the heat balance equation is shown below:

$$\begin{aligned} mc\frac{dT}{dt} &= \dot{Q}_{in} - \dot{Q}_{out} \\ &= \dot{Q}_{solar} + \dot{Q}_{albedo} + \dot{Q}_{earth\ infrared} + \dot{Q}_{generated} - \dot{Q}_{deep\ space} \end{aligned}$$

The coefficient of thermal expansion $\alpha$ is a material property relevant for thermoelastic analyses and is defined as the change in engineering strain $\epsilon$ due to a unit increase in temperature. In most cases, as well as in the present work, the value of $\alpha$ is assumed to be constant over the temperature range of interest. For a one-dimensional bar of length $L_{ref}$ at a temperature $T_{ref}$, the increase or decrease in the length of the bar is given by:

$$\Delta L = L_{ref}\ \epsilon = L_{ref}\ \alpha\Delta T = L_{ref}\ \alpha(T - T_{ref})$$

When the bar is free to expand or contract, the axial stress $\sigma_{xx}$ is zero. However, when its ends are constrained so that it cannot expand or contract, then $\sigma_{xx} = E\ \alpha\Delta T$.

### 6.1.2. Margin of Safety

Similar to the approach described in Chapter 5, the uncertainties in the thermoelastic analyses are taken into account using the $MOS$, but the equation is slightly modified [83]. The thermal model factor ($K_{M_T}$) and the structural model factor ($K_{M_S}$) cover uncertainties in the thermal model and structural model, respectively. As these analyses are being conducted for the first time, a highly conservative value of 1.2 is used for both of them. Just like the structural project factor ($K_P$) for the vibrational analyses, a thermal environment factor ($K_E$) is used, which has a moderately conservative value of 1.1 due to the use of flight-grade components. Temperature mapping is the transfer of the calculated temperatures from the thermal model to the structural model so that they are used as temperature loading for the thermoelastic analysis. Due to differences in the methods by which the thermal and structural analyses are carried out, this mapping process involves a source of error and is defined by the mapping factor ($K_{map}$). As the present thermoelastic analyses involve approximating the temperatures from the thermal analyses, a highly conservative value of 1.2 is used.

$$MOS = \frac{\sigma_Y}{\sigma_{vm,max} \times K_{M_T} \times K_{M_S} \times K_E \times K_{map} \times FOSY} - 1$$

## 6.2. Thermal Analysis

A simple thermal FE model of the CubeSat was first developed in NX Simcenter Space Systems Thermal by a fellow team member, as shown in Figure 6.1. The model consisted of a box representing the CubeSat body, four rectangles representing the deployed solar panels, and two thermal nodes inside the box representing the payload and the internal bus. The surfaces of the solar panels facing the sun were assigned the properties of solar cells. Among the external surfaces of the box, the one facing the sun was assigned the properties of solar cells, while the remaining five faces were black anodised aluminium. All the internal surfaces of the box and the surfaces of the solar panels away from the sun were assigned the properties of white paint. The thermo-optical properties of these different surfaces are shown in Table 6.1.

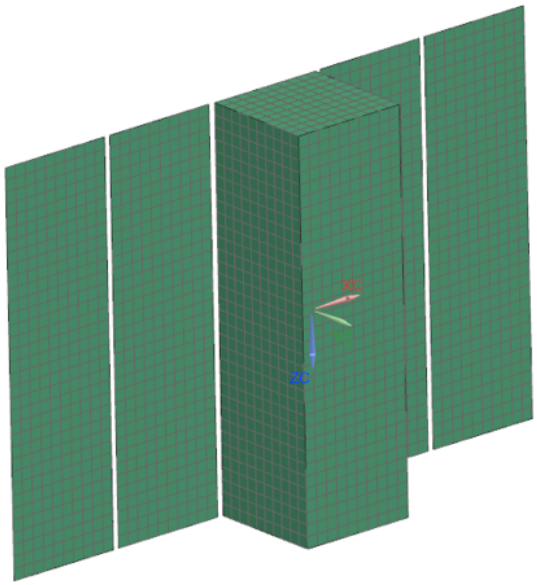

**Figure 6.1:** CubeSat thermal model (credit to another team member)

**Table 6.1:** Thermo-optical properties [84]

| Surface | Absorptivity | Emissivity |
|---|---|---|
| Black anodised aluminium | 0.85 | 0.85 |
| White paint | 0.17 | 0.82 |
| Solar cells | 0.91 | 0.81 |

This model evaluated two different scenarios, namely, a full load condition where all components operate at their maximum power consumption and hence dissipate the maximum amount of power, and an idle load condition where none of the components dissipate power. For the former, the payload and the internal bus were assumed to dissipate 12 W and 10 W, respectively, based on calculations performed by another team member working on the EPS. The orbit of the CubeSat was such that the solar panels face the sun for nearly the entire orbit to maximise the power generated, with minimal time spent in eclipse. Hence, the two thermal load cases were found to be sufficient as the CubeSat did not experience significant variations in the loads due to $\dot{Q}_{solar}$, $\dot{Q}_{albedo}$, and $\dot{Q}_{earth\ infrared}$.

The results of the steady state analyses for the two cases are shown in Figure 6.2, and as expected, the full load case showed comparatively higher temperatures. In order to map all these temperatures

into the structural model in ANSYS, it was decided that each component should be assigned a uniform temperature. As the temperatures of the screws were not directly obtained from the thermal analysis, they were taken as the average of the temperatures of the two components which were connected by them. Similarly, the temperatures of the guide rods were taken as the average of the temperatures of both end frames and the payload mount. Furthermore, the temperature of the payload mount was assumed to be that of the payload. All these approximations in the input temperatures were accounted for by the conservative $K_{map}$ described earlier. Hence, the temperatures of all components to be used for the thermoelastic analyses are shown in Table 6.2.

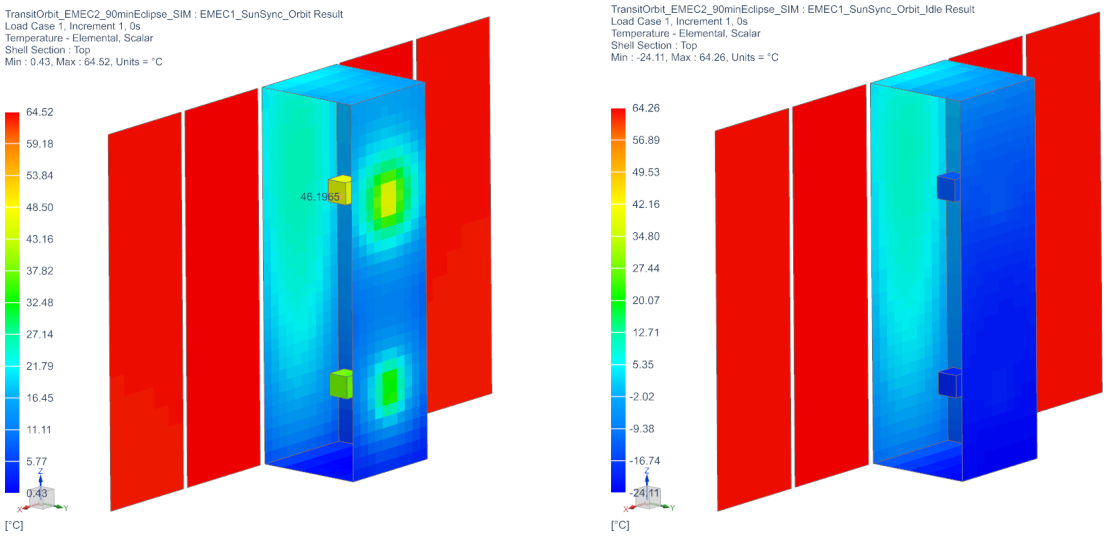


**(a)** Full load case **(b)** Idle load case

**Figure 6.2:** Thermal analysis results (credit to another team member)

**Table 6.2:** Input temperatures of components

| Component | Temperature [°C] | |
|---|---|---|
| | Full load case | Idle load case |
| +$Z$ end frame | 0 | -24 |
| -$Z$ end frame | 18 | 0 |
| Side frames | 12 | -10 |
| Payload mount | 46 | -18 |
| Screws connecting +$Z$ end frame and side frame | 6 | -17 |
| Screws connecting -$Z$ end frame and side frame | 15 | -5 |
| Screws connecting payload mount and side frame | 29 | -14 |
| Guide rods | 21 | -14 |

## 6.3. Setup

### 6.3.1. Geometry Idealisation

The geometry was idealised in almost the same way as that of the vibrational analyses, except for two important changes. First, as the solar arrays would be in their deployed configuration, the CG and MOI properties of their point masses were also modified to represent this case, as shown in Table 6.3. The second change was using RBE3 instead of RBE2 as the MPCs for connecting the point masses of the payload and the internal bus with the payload mount and guide rods, respectively. This can be attributed to the fact that the infinitely stiff RBE2 would prevent the payload mount and guide rods from deforming and cause abnormally high thermoelastic stresses in them.

The thermoelastic analyses require a reference temperature, which serves as the basis for calculating

**Table 6.3:** Solar array point mass properties for deployed configuration

| Component | CG [mm] | | | Mass MOI [kg mm$^2$] | | |
|---|---|---|---|---|---|---|
| | $X$ | $Y$ | $Z$ | $I_X$ | $I_Y$ | $I_Z$ |
| Solar Array (+$X$) | 110.52 | 31.47 | -0.05 | 4,574.48 | 10,578.89 | 7,316.22 |
| Solar Array (-$X$) | -110.52 | 31.47 | 0.05 | 4,574.48 | 10,578.89 | 7,316.22 |

thermal strains and stresses. In the present work, the reference temperature was taken as 22 °C, as this was a typical temperature of the cleanroom where the CubeSat would be assembled and integrated with the launch vehicle [85]. Furthermore, geometric nonlinearity was taken into account by enabling the 'large deflections' option.

### 6.3.2. Boundary Conditions

As the CubeSat in space would not be constrained in any manner, it might seem appropriate at first glance to use no supports on any of the external surfaces of the model. However, doing so is likely to cause extremely long run times, which might even result in non-convergence. In order to resolve this issue, ANSYS provides an option known as 'quasi-static solution' which aids in the convergence of the analysis. Similar to the vibrational analyses, a model check for the thermoelastic analyses was performed to ensure accurate results, and this is discussed in Appendix D.

## 6.4. Results and Discussion

### 6.4.1. Full Load Case

The stress and total deformation for the full load case are shown in Figure 6.3. As only the payload mount had a higher temperature than the reference temperature, it experienced thermal expansion, while the remaining components experienced thermal contraction. It was observed that there were high stresses at the eight screw holes of the +$Z$ end frame, where it was attached to the side frame, and the maximum von-Mises stress among them was 74.96 MPa with a corresponding $MOS$ of 2.06. The main reason for these stresses could be because of the large temperature difference of the +$Z$ end frame from the reference temperature, coupled with its low deformation. Moreover, there were high stresses on the side frames in the regions where they were in contact with the payload mount, and this was because of the thermal expansion of the payload mount pushing the side frames outwards.

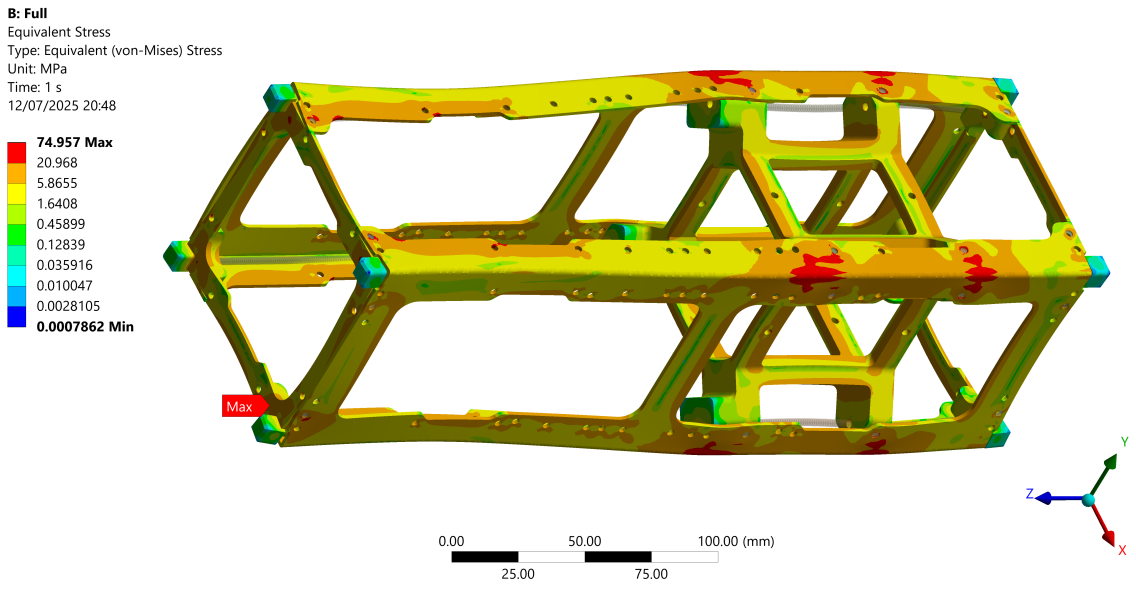


**(a)** Stress

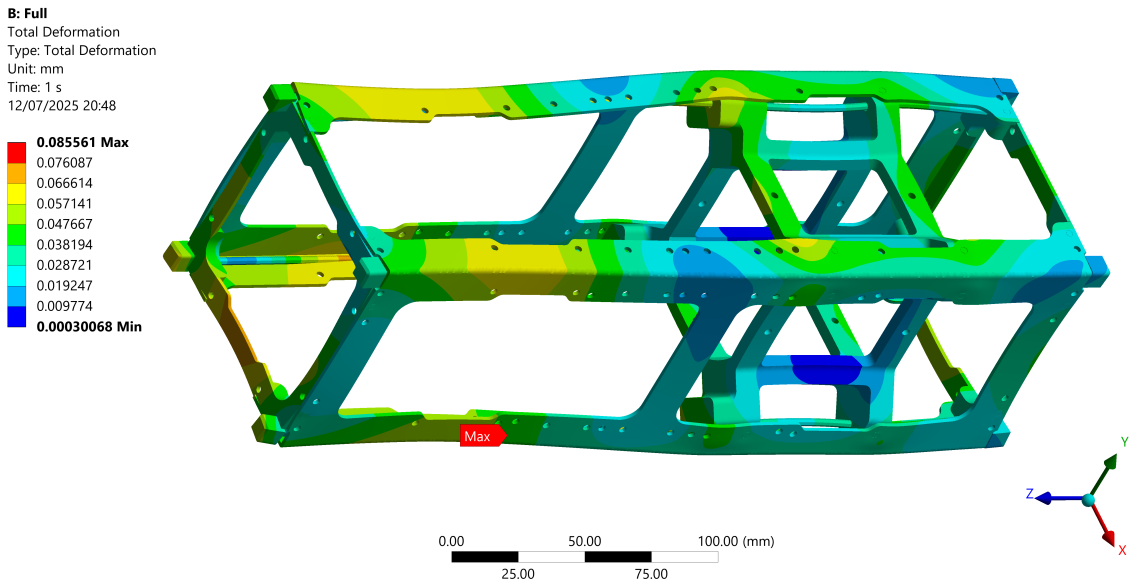


**(b)** Total deformation

**Figure 6.3:** Full load case results

### 6.4.2. Idle Load Case

The stress and total deformation for the idle load case are shown in Figure 6.4. All components experienced thermal contraction as their temperatures were lower than that of the reference temperature. It was observed that the highest stresses occur in the four holes of the -$Z$ end frame, which were attached to the guide rods, and the maximum von-Mises stress among them was 125.18 MPa with a corresponding $MOS$ of 0.83. These high stresses were caused because the -$Z$ end frame had the least temperature difference from the reference temperature, and hence, did not contract along with the rest of the components. The largest deformations were seen at the extremities of both end frames due to the overall thermal contraction of the side frames and the payload mount.

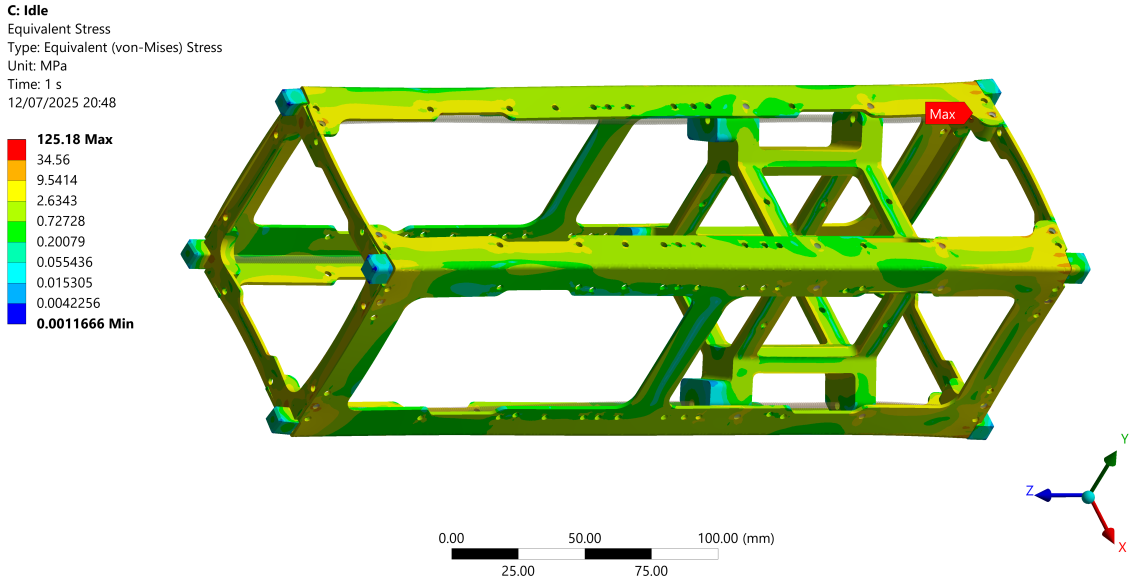


**(a)** Stress

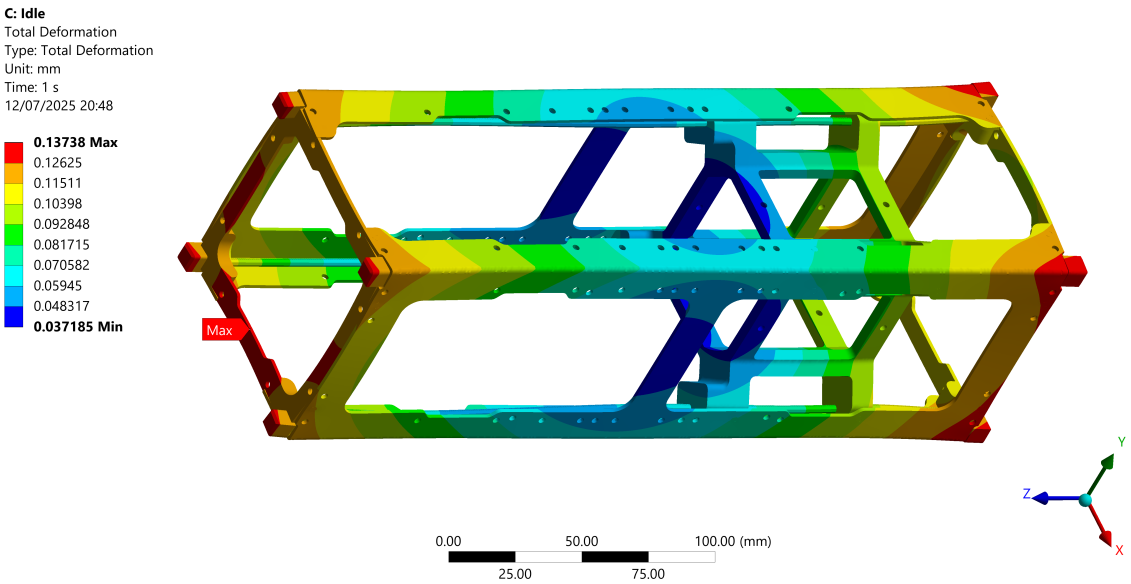


**(b)** Total deformation

**Figure 6.4:** Idle load case results

# 7

# Conclusions

Hyperspectral imaging has a variety of commercially important applications in Earth observation due to its advanced functionalities, but the use of such payloads aboard CubeSats is challenging due to their demanding requirements. This thesis aimed to answer the research question: *To what extent can the structural subsystem of an Earth observation 3U CubeSat be developed to comply with requirements from a hyperspectral imaging payload, the bus subsystems, the dispenser, the launch vehicle, and the space environment?*

A CAD model of the complete CubeSat was designed in Autodesk Fusion based on the requirements from the EXOpod Nova dispenser. The primary structure consisted of the end frames, the side frames, and the payload mount made from Aluminium 7075-T6, and the screws, washers, and guide rods made of Stainless Steel 304. The total mass of the CubeSat was found to be 6.482 kg after including a mass margin of 20%, and this was under the 7 kg limit specified by the dispenser. The maximum side protrusion of the solar panels in their stowed configuration was 8.17 mm, while their width was 87.02 mm, and both of these were within the 25 mm and 87.2 mm limits, respectively. At the tuna-can portion, the diameter of the bounding cylinder around the payload was 70.28 mm, while it protrudes 77.25 mm from the end of the CubeSat rail, both of which were below the 93 mm and 78 mm limits, respectively. The coordinates of the CubeSat CG were -0.10 mm, -0.68 mm, and 2.81 mm when the solar panels were stowed, while they changed to -0.10 mm, 4.42 mm, and 2.81 mm when the solar panels were deployed, and both of these were well within the limits of ±20 mm, ±20 mm, and ±70 mm.

Quasi-static loads, random vibrations, and shock loads were the most relevant types of loads that the CubeSat would need to withstand during the launch phase, and vibrational analyses were conducted in ANSYS Workbench. Among the different launch vehicles, the loads of Falcon 9, Electron, Ariane 6, and Vega-C were compared, and the most conservative values were used as inputs for the analyses, except for the shock loads, where the reduced loads from the dispenser were used. In order to simplify the computational effort, all non-structural components were replaced by point masses, while the screws and guide rods were represented using line bodies. The boundary conditions for all these analyses were according to how the dispenser constrains the external surfaces of the CubeSat along the three axes. After running the analyses on a multi-core processor, the results were used to determine margins of safety, and a positive value of this would indicate that the material does not fail due to yielding. For the quasi-static loads, random vibrations, and shock loads, the margins of safety were respectively found to be 9.95, 3.09, and 0.13, implying that the CubeSat withstands them, despite the shock loads being the most damaging. Furthermore, a modal analysis indicated that the first natural frequency of the CubeSat was 822.69 Hz, which was well above the minimum requirement of 115 Hz, and hence, resonance was unlikely.

Sensitivity analyses, using Latin Hypercube Sampling for the input parameters and the MOP approach to determine their sensitivities, were carried out in optiSLang. From the sensitivity analysis of the full CubeSat model with the first frequency as an output parameter, it was observed that the payload mass and the Young's modulus of Aluminium had the greatest influence. For the standalone end frame with

the first frequency and the average stress from the shock loads as output parameters, the density of Aluminium and the thickness of this component were also found to be important parameters.

A steady-state thermal analysis, based on the orbital parameters, was first performed on a simple model of the CubeSat by another team member. Two different scenarios were analysed, namely, a full load condition where all components dissipate the maximum amount of power, and an idle load condition where none of the components dissipate power. After approximating the results of the thermal analyses to obtain the temperatures of each component, these were used as inputs for the thermoelastic analyses in ANSYS Workbench. As the CubeSat would be free in space, no constraints were applied to the model. Just like the vibrational analyses, the results of the thermoelastic analyses were also used to determine margins of safety, and these values for the full load and idle load cases were 2.06 and 0.83, respectively, implying that the CubeSat withstands the thermoelastic loads.

# 8

# Future Work

## 8.1. Structural Design

The current version of the CAD model neither has cables being modelled between components, nor have these been included in the mass breakdown of Table 4.4. Although the internal bus components are attached to each other with the dual interface ports, the connections between the solar panels, patch antennae, and the payload would need to be made using cables. However, these can only be finalised later in the mission when all the components are already procured. The top of the $+Z$ end frame is also kept free for attaching additional components, such as a 1U solar panel [86] or a deployable antenna [87], in case they are deemed necessary by future studies of the bus subsystem requirements.

Once the design of the payload is finalised by HYSPIM, any modifications to its shape and mass from the current version would need to be updated in the CAD model. Moreover, as the mission progresses further, NDAs would likely need to be signed with EnduroSat and AAC Clyde Space to obtain the actual CAD models. This would be necessary to avoid uncertainties in their CG and MOI properties and to develop a more realistic CAD model of the CubeSat.

## 8.2. Vibrational Analysis

The most important next steps would be testing a model of the CubeSat primary structure in a dedicated apparatus and using the test results to update certain parameters of the FE analyses, such as material properties and dimensions of structural components. This model would also include dummy masses representing the presence of the other subsystem components. A starting point for developing this model would be to purchase the 3U CubeSat structure from EnduroSat, although its design is slightly different from that of the CAD model, and it uses a different aluminium alloy. It includes all components except for the payload mount, which would need to be manufactured separately. The second option involves all the components being manufactured using 3D printing or CNC machining, while the screws would need to be purchased.

The model of the CubeSat would need to be properly attached to a shaker table in order to represent the boundary conditions from the dispenser correctly. The most preferred way of accomplishing this would be using the Exolaunch Nova TestPod, whose main purpose is performing mechanical testing and fit checks on CubeSats [88]. The TestPod design is such that it can be easily mounted to a shaker table, and all its mechanical interfaces with the CubeSat are identical to those of the EXOpod Nova dispenser. If the TestPod cannot be procured easily, the other option involves designing and manufacturing a fixture that would lock the external surfaces of the CubeSat rails in their normal directions.

Among the different results from the FE analyses that can be used, the ones of particular importance are those from the modal analysis. To do so, a modal survey test will be conducted to identify the experimental natural frequencies, mode shapes, damping ratios, and effective mass fractions of the CubeSat [89]. These would be compared with the numerical results from the FE analyses to determine quantities such as the Modal Assurance Criterion (MAC) and Frequency Response Assurance Criterion

(FRAC). An objective function to be minimised can then be defined using these quantities, similar to the one presented in this work, and an optimisation performed on this would result in updated parameters.

Apart from the modal survey test, the tests using the other load types of the launch vehicle would also need to be performed. This is especially relevant for the shock loads case, similar to that of the MIST CubeSat, to verify whether the high stresses from the FE analysis using the original acceleration SRS in Table 5.4a will occur in reality or not. Furthermore, this would verify that the redesign of the original 3U CubeSat structure from EnduroSat was warranted.

## 8.3. Thermoelastic Analysis

The current thermoelastic analyses required many approximations on the input temperatures applied to the components of the primary structure. Moreover, temperature gradients across the same component were not considered. Hence, a thermal analysis involving a more detailed model of the CubeSat will need to be carried out, preferably within ANSYS itself, so that the temperature mapping for the thermoelastic analyses is performed without any approximations. Once this is complete, the linear and angular deformations of the payload and the payload mount would need to be calculated. These can then be used to evaluate the pointing accuracy of the payload based on its finalised design and specifications.

# References


[1] S. Janson, "The concept and history of small satellites," in *Next Generation CubeSats and SmallSats*. Elsevier, Sep. 2023, pp. 9–55, ISBN: 9780128245415. DOI: 10.1016/B978-0-12-824541-5.00017-0. (visited on Jul. 31, 2025).

[2] D. A. Barnhart and R. Rughani, "Comparing platform paradigms: CubeSats versus SmallSats," in *Next Generation CubeSats and SmallSats*. Elsevier, Sep. 2023, pp. 57–78, ISBN: 9780128245415. DOI: 10.1016/B978-0-12-824541-5.00020-0. (visited on Jul. 31, 2025).

[3] "Active Satellite Orbital Data," Orbiting Now. (Jul. 2025), [Online]. Available: https://orbit.ing-now.com (visited on Jul. 31, 2025).

[4] K. Sergieieva. "Types Of Satellites: Different Orbits & Real-World Uses," EOS Data Analytics. (Mar. 2025), [Online]. Available: https://eos.com/blog/types-of-satellites (visited on Jul. 31, 2025).

[5] S. Caldwell. "What are SmallSats and CubeSats?" NASA Ames Research Center, Small Spacecraft Systems Virtual Institute. (Aug. 2024), [Online]. Available: https://www.nasa.gov/what-are-smallsats-and-cubesats (visited on Jul. 31, 2025).

[6] E. Kulu. "Nanosats Database." (Jul. 2025), [Online]. Available: https://www.nanosats.eu (visited on Jul. 31, 2025).

[7] B. Foing, M. Raouf, P. R. Mitra, *et al.*, "Moon Missions, Data, Instruments, Field Work, Astronauts, Habitats, Business: ILEWG EMMESI EuroMoonMars Earth Space Innovation 2023-2024 Highlights," 56th Lunar and Planetary Science Conference, Mar. 2025. [Online]. Available: https://www.hou.usra.edu/meetings/lpsc2025/pdf/1316.pdf (visited on Jul. 31, 2025).

[8] B. Foing, "From SMART1 and recent probes towards Artemis and a human/robotic Moon Village," *Journal of Physics: Conference Series*, vol. 2877, no. 1, p. 012 037, Oct. 2024. DOI: 10.1088/1742-6596/2877/1/012037. (visited on Jul. 31, 2025).

[9] M. Raouf, B. Foing, P. R. Mitra, *et al.*, "Education Cubesats and Payload for Research and Worksforce Development," 56th Lunar and Planetary Science Conference, Mar. 2025. [Online]. Available: https://www.hou.usra.edu/meetings/lpsc2025/pdf/2696.pdf (visited on Jul. 31, 2025).

[10] M. Raouf, B. Foing, P. R. Mitra, *et al.*, "Educational Cubesats: Remote Sensing of Earth and Lunar Surface," European Lunar Symposium, Jun. 2025. DOI: 10.5281/zenodo.15497197. (visited on Jul. 31, 2025).

[11] A. Bhargava, A. Sachdeva, K. Sharma, M. H. Alsharif, P. Uthansakul, and M. Uthansakul, "Hyperspectral imaging and its applications: A review," *Heliyon*, vol. 10, no. 12, e33208, Jun. 2024, ISSN: 2405-8440. DOI: 10.1016/j.heliyon.2024.e33208. (visited on Jul. 31, 2025).

[12] "What is Hyperspectral Imaging," NIREOS. (Jul. 2025), [Online]. Available: https://nireos.com/application/what-is-hyperspectral-imaging (visited on Jul. 31, 2025).

[13] S.-E. Qian, "Hyperspectral Satellites, Evolution, and Development History," *IEEE Journal of Selected Topics in Applied Earth Observations and Remote Sensing*, vol. 14, pp. 7032–7056, Jun. 2021, ISSN: 2151-1535. DOI: 10.1109/jstars.2021.3090256. (visited on Jul. 31, 2025).

[14] "Hyperspectral Imagery," Pixxel. (Jul. 2025), [Online]. Available: https://www.pixxel.space/hyperspectral-imagery (visited on Jul. 31, 2025).

[15] "Why Hyperspectral?" Wyvern. (Jul. 2025), [Online]. Available: https://wyvern.space/why-hyperspectral (visited on Jul. 31, 2025).

[16] "AVIRIS Moffett Field Image Cube," NASA Jet Propulsion Laboratory. (May 2024), [Online]. Available: https://aviris.jpl.nasa.gov/data/image_cube.html (visited on Jul. 31, 2025).

[17] D. Selva and D. Krejci, “A survey and assessment of the capabilities of CubeSats for Earth observation,” *Acta Astronautica*, vol. 74, pp. 50–68, Jun. 2012, ISSN: 0094-5765. DOI: 10.1016/j.actaastro.2011.12.014. (visited on Jul. 31, 2025).

[18] N. D. Fite, “Deployers,” in *CubeSat Handbook*. Academic Press, Oct. 2021, pp. 415–429, ISBN: 9780128178843. DOI: 10.1016/B978-0-12-817884-3.00022-9. (visited on Jul. 31, 2025).

[19] “Poly Picosatellite Orbital Deployer Mk. III Rev. E User Guide,” The CubeSat Program, Cal Poly SLO. (Mar. 2014), [Online]. Available: https://www.cubesat.org/s/P-POD_MkIIIRevE_UserGuide_CP-PPODUG-10-1_Rev1.pdf (visited on Jul. 31, 2025).

[20] S. Caldwell. “Integration, Launch, and Deployment,” NASA Ames Research Center, Small Spacecraft Systems Virtual Institute. (Feb. 2025), [Online]. Available: https://www.nasa.gov/smallsat-institute/sst-soa/integration-launch-and-deployment (visited on Jul. 31, 2025).

[21] “Canisterized Satellite Dispenser,” Rocket Lab. (May 2022), [Online]. Available: https://rocketlabcorp.com/assets/Uploads/2002337G-CSD-Data-Sheet-compressed.pdf (visited on Jul. 31, 2025).

[22] “PicoSatellite Launcher,” ASTROFEIN. (Jul. 2025), [Online]. Available: https://www.astrofein.com/en/cubesat-deployer (visited on Jul. 31, 2025).

[23] “Satellite Orbital Deployers Range,” Dhruva Space. (Jul. 2025), [Online]. Available: https://www.dhruvaspace.com/launch-services#orbital-deployers (visited on Jul. 31, 2025).

[24] “EXOpod Nova User Manual,” Exolaunch. (Jun. 2024), [Online]. Available: https://www.exolaunch.com/documents/EXOpod_Nova_User_Manual_June_2024.pdf (visited on Jul. 31, 2025).

[25] “DuoPack Deployer,” ISISPACE Group. (Jul. 2025), [Online]. Available: https://www.isispace.nl/product/duopack-deployer (visited on Jul. 31, 2025).

[26] “JEM Payload Accommodation Handbook,” Japan Aerospace Exploration Agency. (Apr. 2023), [Online]. Available: https://humans-in-space.jaxa.jp/kibouser/library/item/jx-espc_8e_en.pdf (visited on Jul. 31, 2025).

[27] “Smallsat & Microsat Deployment,” Voyager. (Jul. 2025), [Online]. Available: https://voyagertechnologies.com/space-solutions/smallsat-microsat-deployment (visited on Jul. 31, 2025).

[28] E. Kulu. “Small Satellite Launchers.” (Jul. 2025), [Online]. Available: https://www.newspace.im/launchers (visited on Jul. 31, 2025).

[29] J. Costa. “CubeSat Launch Initiative,” NASA Kennedy Space Center. (May 2024), [Online]. Available: https://www.nasa.gov/kennedy/launch-services-program/cubesat-launch-initiative (visited on Jul. 31, 2025).

[30] “Fly Your Satellite!” ESA. (Jul. 2025), [Online]. Available: https://www.esa.int/Education/CubeSats_-_Fly_Your_Satellite (visited on Jul. 31, 2025).

[31] “Launches,” SpaceX. (Jul. 2025), [Online]. Available: https://www.spacex.com/launches (visited on Jul. 31, 2025).

[32] M. Hader. “Supporting Europe’s microlauncher lift-off,” Roland Berger. (May 2021), [Online]. Available: https://www.rolandberger.com/en/Insights/Publications/Supporting-Europe%27s-microlauncher-lift-off.html (visited on Jul. 31, 2025).

[33] P. L. K. Da Cás, “Launch vehicle overview,” in *CubeSat Handbook*. Academic Press, Oct. 2021, pp. 431–444, ISBN: 9780128178843. DOI: 10.1016/B978-0-12-817884-3.00023-0. (visited on Jul. 31, 2025).

[34] J. Wijker, “Spacecraft Design Loads,” in *Spacecraft Structures*. Springer, Berlin, Heidelberg, Jan. 2008, pp. 27–69, ISBN: 9783540755531. DOI: 10.1007/978-3-540-75553-1_6. (visited on Jul. 31, 2025).

[35] “Spacecraft mechanical loads analysis handbook,” European Cooperation for Space Standardization. (Feb. 2013), [Online]. Available: https://ecss.nl/wp-content/uploads/handbooks/ecss-e-hb/ECSS-E-HB-32-26A19February2013.pdf (visited on Jul. 31, 2025).

[36] S. Caldwell. “Thermal Control,” NASA Ames Research Center, Small Spacecraft Systems Virtual Institute. (Feb. 2025), [Online]. Available: https://www.nasa.gov/smallsat-institute/sst-soa/thermal-control (visited on Jul. 31, 2025).

[37] M. M. Finckenor and K. K. de Groh. “A Researcher’s Guide to: Space Environmental Effects,” NASA ISS Research Integration Office. (Sep. 2020), [Online]. Available: https://www.nasa.gov/wp-content/uploads/2020/10/researchers-guide-space-environment-effects_tagged.pdf (visited on Jul. 31, 2025).

[38] C. Cappelletti, “Structure, new materials, and new manufacturing technologies,” in *CubeSat Handbook*. Academic Press, Oct. 2021, pp. 165–183, ISBN: 9780128178843. DOI: 10.1016/B978-0-12-817884-3.00008-4. (visited on Jul. 31, 2025).

[39] “CubeSat Design Specification Rev. 14.1,” The CubeSat Program, Cal Poly SLO. (Feb. 2022), [Online]. Available: https://www.cubesat.org/s/CDS-REV14_1-2022-02-09.pdf (visited on Jul. 31, 2025).

[40] S. Caldwell. “Structures, Materials, and Mechanisms,” NASA Ames Research Center, Small Spacecraft Systems Virtual Institute. (Feb. 2025), [Online]. Available: https://www.nasa.gov/smallsat-institute/sst-soa/structures-materials-and-mechanisms (visited on Jul. 31, 2025).

[41] “VERSE-03 3U Structure,” 2NDSpace. (Jul. 2025), [Online]. Available: https://www.2ndspace.eu/cubesat-platforms/cubesat-structures-1 (visited on Jul. 31, 2025).

[42] “Cubesat Structures,” AAC Clyde Space. (Jul. 2025), [Online]. Available: https://www.aac-clyde.space/what-we-do/space-products-components/cubesat-structures (visited on Jul. 31, 2025).

[43] “Structures,” C3S. (Jul. 2025), [Online]. Available: https://c3s.hu/structures (visited on Jul. 31, 2025).

[44] “3U CubeSat Structure,” EnduroSat. (Jul. 2025), [Online]. Available: https://www.endurosat.com/products/3u-cubesat-structure (visited on Jul. 31, 2025).

[45] “3U CubeSat Structure,” Gran Systems. (Jul. 2025), [Online]. Available: https://gransystems.com/products/cubesat-structure/3UCubeStructure (visited on Jul. 31, 2025).

[46] “SM03 Cubesat Structure,” NPC Spacemind. (Jul. 2025), [Online]. Available: https://www.npcspacemind.com/product/sm03 (visited on Jul. 31, 2025).

[47] “CubeSat Kit™ Structures,” Pumpkin Space Systems. (Jul. 2025), [Online]. Available: https://www.pumpkinspace.com/store/c4/CubeSat_Kit%E2%84%A2_Structures.html (visited on Jul. 31, 2025).

[48] “Structures,” Serenum Space. (Jul. 2025), [Online]. Available: https://www.serenumspace.com/products/satelite-subsystems/modular-cubesat-structure (visited on Jul. 31, 2025).

[49] T. Kuwahara. “System Integration of CubeSats,” Tohoku University. (Nov. 2021), [Online]. Available: https://www.unoosa.org/documents/pdf/psa/access2space4all/KiboCUBE/AcademySeason2/Live_Session/Live_Session_1/KiboCUBE_Academy_2021_Online_1-2_kuwahara_v4.1_Updated.pdf (visited on Jul. 31, 2025).

[50] A. S. Elshaal, “Design Analysis of the Structural System of AlAinSat-1 CubeSat by Simulation and Experimental Validation,” Master Thesis, United Arab Emirates University, Apr. 2024. [Online]. Available: https://scholarworks.uaeu.ac.ae/all_theses/1218 (visited on Jul. 31, 2025).

[51] C. Järmyr Eriksson, “Finite Element Analysis of Stresses in the MIST CubeSat due to Dynamic Loads During Launch,” Master Thesis, KTH Royal Institute of Technology, Oct. 2021. [Online]. Available: https://urn.kb.se/resolve?urn=urn:nbn:se:kth:diva-309956 (visited on Jul. 31, 2025).

[52] M. B. V. Guedes, “CubeSat Structural and Thermal Analysis Methodology ISTsat-1 Design,” Master Thesis, Instituto Superior Técnico, Jun. 2019. [Online]. Available: https://catalogo-ist.biblioteca.ulisboa.pt/cgi-bin/koha/opac-detail.pl?biblionumber=637170 (visited on Jul. 31, 2025).

[53] L. Feria del Rosario, “Design of the mechanical structure for the CubeSat TeideSat,” Bachelor Thesis, Universidad de La Laguna, Jul. 2018. [Online]. Available: https://riull.ull.es/xmlui/handle/915/9467 (visited on Jul. 31, 2025).

[54] K. M. Slabinski, J. B. Jacobson, W. T. Schlack, and E. A. Curci, “Design and Analysis for the Sphinx-NG CubeSat,” Bachelor Thesis, Worcester Polytechnic Institute, Mar. 2017. [Online]. Available: https://digital.wpi.edu/concern/student_works/2v23vw25z (visited on Jul. 31, 2025).

[55] J. Fagerudd, “Stress simulation of the SEAM CubeSat structure during launch,” Master Thesis, KTH Royal Institute of Technology, Oct. 2015. [Online]. Available: https://urn.kb.se/resolve?urn=urn:nbn:se:kth:diva-176014 (visited on Jul. 31, 2025).

[56] “Hyperspectral Camera,” HYSPIM. (Jul. 2025), [Online]. Available: https://www.hyspim.com (visited on Jul. 31, 2025).

[57] “Board Specification,” LibreCube. (Jul. 2025), [Online]. Available: https://librecube.gitlab.io/standards/board_specification (visited on Jul. 31, 2025).

[58] “7075-T6 Aluminum,” MakeItFrom. (Jul. 2025), [Online]. Available: https://www.makeitfrom.com/material-properties/7075-T6-Aluminum (visited on Jul. 31, 2025).

[59] “Annealed 304 Stainless Steel,” MakeItFrom. (Jul. 2025), [Online]. Available: https://www.makeitfrom.com/material-properties/Annealed-304-Stainless-Steel (visited on Jul. 31, 2025).

[60] “3U Solar Panel,” EnduroSat. (Jul. 2025), [Online]. Available: https://www.endurosat.com/products/3u-solar-panel (visited on Jul. 31, 2025).

[61] “3U Double Deployable Solar Array,” EnduroSat. (Jul. 2025), [Online]. Available: https://www.endurosat.com/products/3u-deployable-solar-array (visited on Jul. 31, 2025).

[62] “EPS II + Battery Pack,” EnduroSat. (Jul. 2025), [Online]. Available: https://www.endurosat.com/products/eps-ii-battery-pack (visited on Jul. 31, 2025).

[63] “iADCS200,” AAC Clyde Space. (Jul. 2025), [Online]. Available: https://www.aac-clyde.space/what-we-do/space-products-components/adcs/iadcs200 (visited on Jul. 31, 2025).

[64] “Onboard Computer with GNSS,” EnduroSat. (Jul. 2025), [Online]. Available: https://www.endurosat.com/products/onboard-computer-with-gnss (visited on Jul. 31, 2025).

[65] “S-Band Transceiver,” EnduroSat. (Jul. 2025), [Online]. Available: https://www.endurosat.com/products/s-band-transceiver (visited on Jul. 31, 2025).

[66] “S-Band Antenna Wideband,” EnduroSat. (Jul. 2025), [Online]. Available: https://www.endurosat.com/products/s-band-antenna-wideband (visited on Jul. 31, 2025).

[67] “X-Band Transmitter,” EnduroSat. (Jul. 2025), [Online]. Available: https://www.endurosat.com/products/x-band-transmitter (visited on Jul. 31, 2025).

[68] “X-Band 4×4 Patch Array,” EnduroSat. (Jul. 2025), [Online]. Available: https://www.endurosat.com/products/x-band-patch-antenna (visited on Jul. 31, 2025).

[69] “Heritage,” Exolaunch. (Jul. 2025), [Online]. Available: https://www.exolaunch.com/heritage (visited on Jul. 31, 2025).

[70] R. Walker. “System Margin Policy for ESA IOD CubeSat Projects,” ESA. (Feb. 2016), [Online]. Available: https://www.ntnu.no/wiki/download/attachments/112275035/IOD_CubeSat_Margin_Policy_iss1_rev_0.pdf (visited on Jul. 31, 2025).

[71] Materials To Build 3D. (Jul. 2025), [Online]. Available: https://www.mtb3d.com/en (visited on Jul. 31, 2025).

[72] J. Wijker, “Modal Analysis,” in *Mechanical Vibrations in Spacecraft Design*. Springer, Berlin, Heidelberg, Apr. 2013, pp. 73–93, ISBN: 9783662085875. DOI: 10.1007/978-3-662-08587-5_5. (visited on Jul. 31, 2025).

[73] J. Wijker, “Random Vibration of Linear Dynamic Systems,” in *Mechanical Vibrations in Spacecraft Design*. Springer, Berlin, Heidelberg, Apr. 2013, pp. 201–246, ISBN: 9783662085875. DOI: 10.1007/978-3-662-08587-5_11. (visited on Jul. 31, 2025).

[74] J. Wijker, “Shock-Response Spectrum,” in *Mechanical Vibrations in Spacecraft Design*. Springer, Berlin, Heidelberg, Apr. 2013, pp. 173–200, ISBN: 9783662085875. DOI: 10.1007/978-3-662-08587-5_10. (visited on Jul. 31, 2025).

[75] “Structural factors of safety for spaceflight hardware,” European Cooperation for Space Standardization. (Aug. 2019), [Online]. Available: https://ecss.nl/wp-content/uploads/2019/09/ECSS-E-ST-32-10C_Rev.2-Corr.1(1August2019).pdf (visited on Jul. 31, 2025).

[76] “Rideshare Payload User’s Guide,” SpaceX. (Sep. 2024), [Online]. Available: https://storage.googleapis.com/rideshare-static/Rideshare_Payload_Users_Guide.pdf (visited on Jul. 31, 2025).

[77] “Electron Payload User’s Guide,” Rocket Lab. (Nov. 2022), [Online]. Available: https://rocketlabcorp.com/assets/Electron-Payload-User-Guide-7.0-v6.pdf (visited on Jul. 31, 2025).

[78] “Ariane 6 User’s Manual for Multi-Launch Service,” Arianespace. (Jul. 2021), [Online]. Available: https://ariane.group/app/uploads/sites/4/2024/10/MLSs-users-manual-ed0.0.pdf (visited on Jul. 31, 2025).

[79] “SSMS Vega-C User’s Manual,” Arianespace. (Sep. 2020), [Online]. Available: https://ariane.group/app/uploads/sites/4/2024/10/SSMS-Vega-C-UsersManual-Issue-1-Rev0-Sept2020.pdf (visited on Jul. 31, 2025).

[80] “What Is The Difference Between A Kinematic (RBE2) And A Distributing (RBE3) Coupling In FEA?” Fidelis. (Jul. 2025), [Online]. Available: https://www.fidelisfea.com/post/what-is-the-difference-between-a-kinematic-rbe2-and-a-distributing-rbe3-coupling-in-fea (visited on Jul. 31, 2025).

[81] “Structural finite element models,” European Cooperation for Space Standardization. (Jul. 2008), [Online]. Available: https://ecss.nl/wp-content/uploads/standards/ecss-e/ECSS-E-ST-32-03C31July2008.pdf (visited on Jul. 31, 2025).

[82] T. Most and J. Will, “Sensitivity analysis using the Metamodel of Optimal Prognosis,” Weimar Optimization and Stochastic Days, Nov. 2011. [Online]. Available: https://library.dynardo.de/fileadmin/Material_Dynardo/bibliothek/WOST_8.0/Paper_Most.pdf (visited on Jul. 31, 2025).

[83] J. Wijker and S. Appel, “Estimating Uncertainties in the Thermoelastic Analysis Process,” in *Simulation of Thermoelastic Behaviour of Spacecraft Structures: Fundamentals and Recommendations*. Springer, Cham, Aug. 2021, pp. 261–307, ISBN: 9783030789992. DOI: 10.1007/978-3-030-78999-2_10. (visited on Jul. 31, 2025).

[84] D. G. Gilmore, *Spacecraft Thermal Control Handbook, Volume 1 - Fundamental Technologies (2nd Edition)*. American Institute of Aeronautics and Astronautics/Aerospace Press (AIAA), Dec. 2002, ISBN: 9781884989117. DOI: 10.2514/4.989117. (visited on Jul. 31, 2025).

[85] K. Smith. “Cleanroom Tech Key to Success in Space,” NASA Office of Strategic Infrastructure. (Sep. 2023), [Online]. Available: https://www.nasa.gov/organizations/osi/setmo/cleanroom-tech-key-to-success-in-space (visited on Jul. 31, 2025).

[86] “1U Solar Panel Z,” EnduroSat. (Jul. 2025), [Online]. Available: https://www.endurosat.com/products/1u-solar-panel-z (visited on Jul. 31, 2025).

[87] “UHF Antenna 1U,” EnduroSat. (Jul. 2025), [Online]. Available: https://www.endurosat.com/products/uhf-antenna-iii (visited on Jul. 31, 2025).

[88] “Nova TestPod User Manual,” Exolaunch. (Jun. 2025), [Online]. Available: https://www.exolaunch.com/documents/EXO_Nova_TestPod_Manual_June_2025.pdf (visited on Jul. 31, 2025).

[89] “Modal survey assessment,” European Cooperation for Space Standardization. (Jul. 2008), [Online]. Available: https://ecss.nl/wp-content/uploads/standards/ecss-e/ECSS-E-ST-32-11C31July2008.pdf (visited on Jul. 31, 2025).

# A

# Version Logs

## A.1. CAD Model

**Table A.1:** CAD model versions

| Version | Description |
|---|---|
| 1.0 | The original end frames and side frames of the 3U Structure were modelled. |
| 1.1 | The guide rods, screws, and washers were added to the model. |
| 2.0 | The Onboard Computer with GNSS, the S-Band Transceiver, and the X-Band Transmitter were modelled. |
| 2.1 | The 4-cell variant of the EPS II + Battery Pack was modelled. |
| 2.2 | The simplified version of the iADCS200 was modelled. |
| 2.3 | The payload and the first concept of the payload mount were modelled. The mass of the latter was attempted to be made as low as possible. |
| 3.0 | The 3U Solar Panel and the Double Deployable Solar Array were modelled, initially with six cells per panel. |
| 3.1 | Motion links were added at the hinges of the solar arrays to visualise their deployment. |
| 3.2 | The number of solar cells per panel was increased to seven. |
| 3.3 | The X-Band 4×4 Patch Array and the S-Band Antenna Commercial were modelled. |
| 4.0 | The EPS II + Battery Pack was changed to the 8-cell variant, which was larger and heavier. |
| 4.1 | The S-Band Antenna Commercial was changed to the heavier S-Band Antenna Wideband, but had the same dimensions. |
| 5.0 | The payload mount was redesigned as shown in Figure A.1 due to the high stresses from the shock loads. |
| 5.1 | The geometries of contact regions between the end frames and the side frames were modified as shown in Figure A.2 to avoid undesirable load paths. |
| 5.2 | The geometry of the end frames where they were attached to the guide rods was modified as shown in Figure A.3. This was the final version discussed in Chapter 4. |

**(a)** Old design (245 g) **(b)** Current design (328 g)

**Figure A.1:** Payload mount redesign

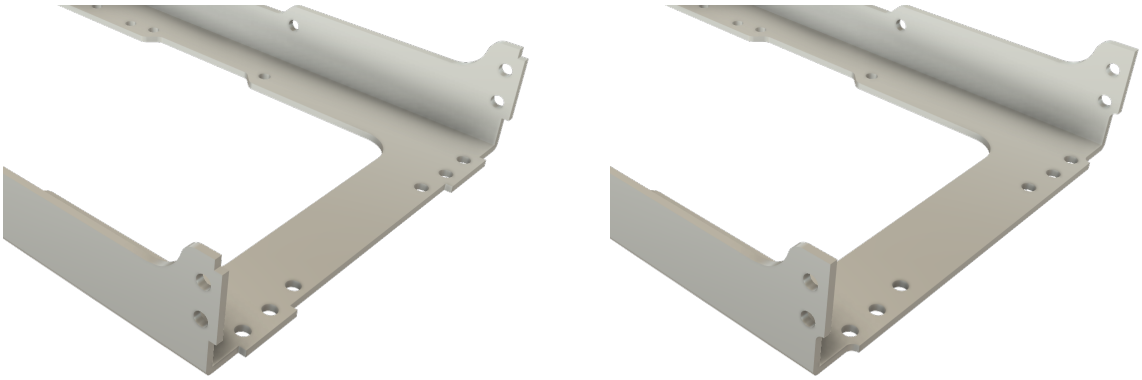

**(a)** Old design (102 g) **(b)** Current design (103 g)

**Figure A.2:** Side frames redesign

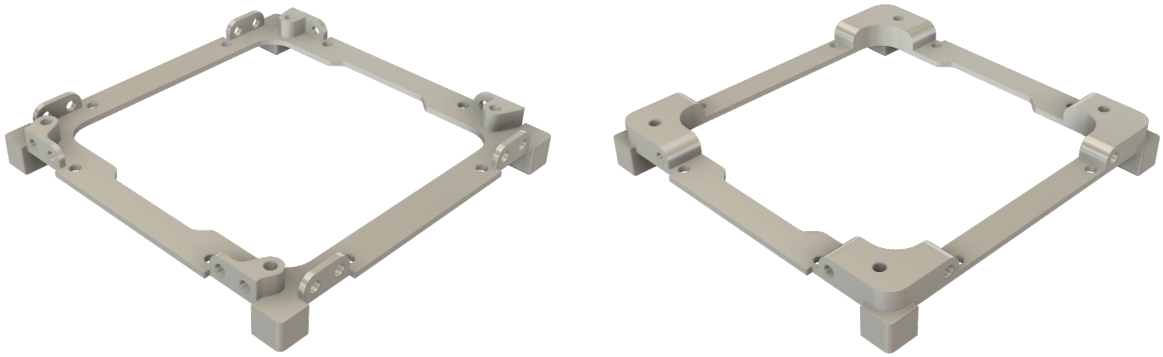

**(a)** Old design (25 g) **(b)** Current design (37 g)

**Figure A.3:** End frames redesign

## A.2. Vibrational Analysis

**Table A.2:** Vibrational analysis versions

| Version | Description |
|---|---|
| 1.0 | The check for rigid body modes was performed on Version 3.3 of the CAD model. Fixed joints were used for connecting line bodies to components, and all contacts were set to no separation. The first mode had a frequency greater than 10 Hz. |
| 1.1 | The joints connecting the payload mount to the guide rods were changed to cylindrical. Six rigid body modes were observed. |
| 2.0 | Vibrational analyses were performed on Version 4.1 of the CAD model using the boundary conditions of the dispenser. The maximum stress from the shock loads was observed to be approximately 3,000 MPa when using the original acceleration SRS in Table 5.4a. |
| 2.1 | All contacts in the model were changed to frictionless. However, the maximum stress from the shock loads did not change. |
| 2.2 | The mesh sizes of the solid elements were reduced from 2.4 mm to 1.2 mm for the end frames, and from 3.2 mm to 1.6 mm for the side frames and the payload mount. As shown in Figure A.4, the maximum stress from the shock loads decreased slightly to 2,850 MPa. |
| 3.0 | Vibrational analyses were performed on Version 5.0 of the CAD model. The maximum stress from the shock loads decreased from 450 MPa to 420 MPa for the payload mount. However, the same high stresses were observed in the end frames and the side frames. |
| 4.0 | The analyses were repeated for Version 5.1 of the CAD model. The maximum stresses from the shock loads decreased to 820 MPa for the side frames but not the end frames. |
| 4.1 | The analyses were repeated for Version 5.2 of the CAD model, as shown in Figure A.5. The maximum stresses from the shock loads decreased to 1,030 MPa for the end frames, but the $MOS$ was clearly negative. |
| 5.0 | The analyses were repeated but using the reduced acceleration SRS in Table 5.4b, and the $MOS$ was positive for the shock loads, as shown in Figure A.6. This model was used for all the vibrational analyses described in Chapter 5. |

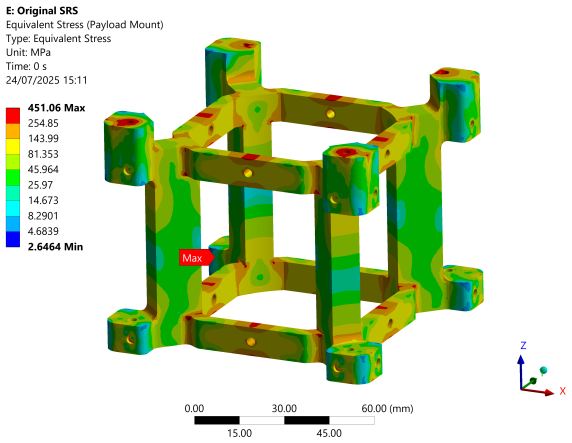


**(a)** Payload mount

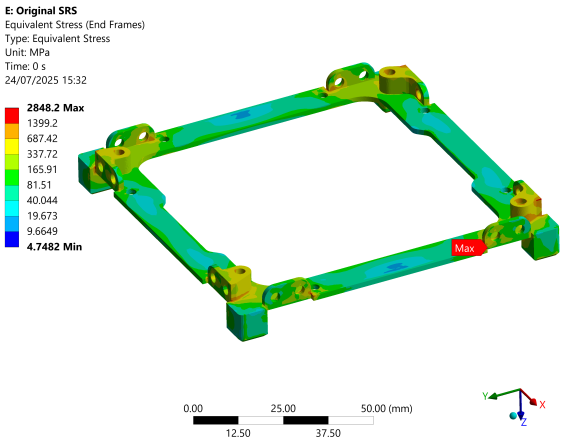


**(b)** End frames

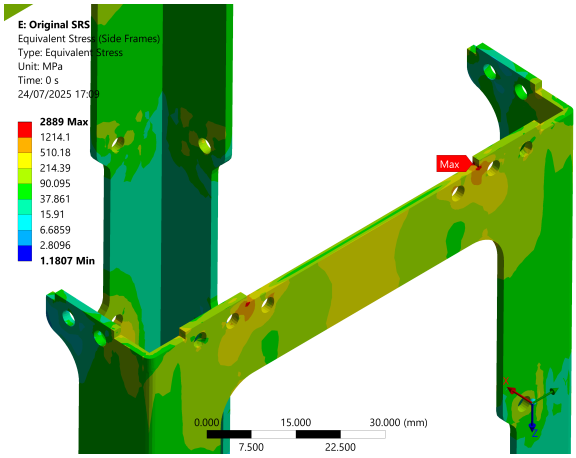


**(c)** Side frames

**Figure A.4:** Old design and original SRS

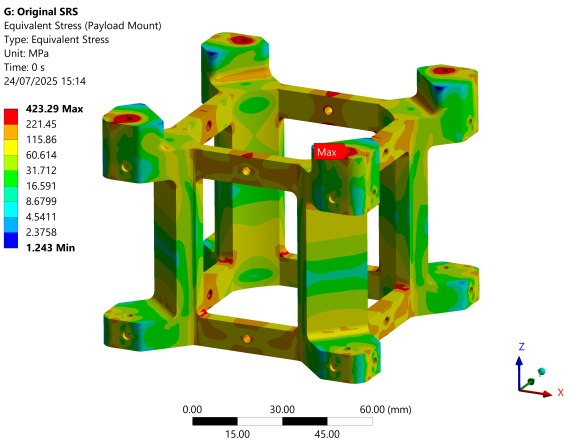


**(a)** Payload mount

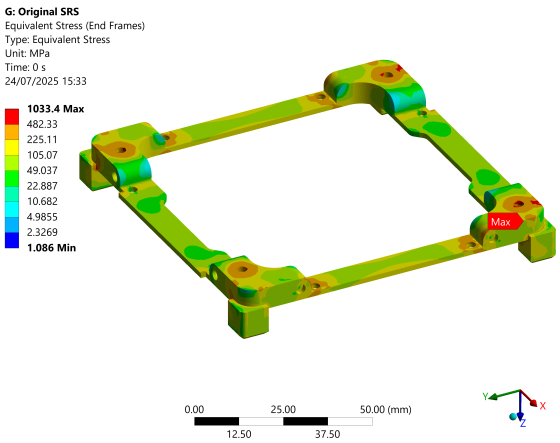


**(b)** End frames

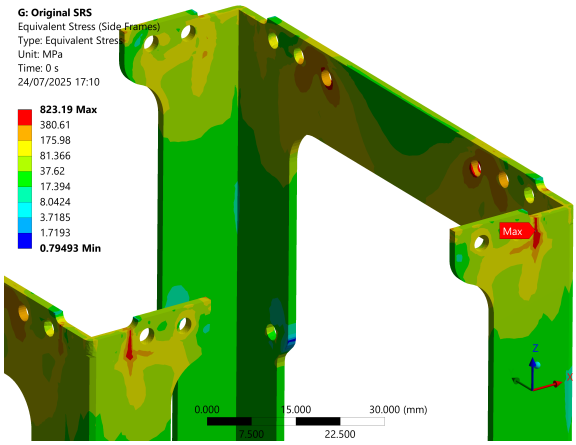


**(c)** Side frames

**Figure A.5:** New design and original SRS

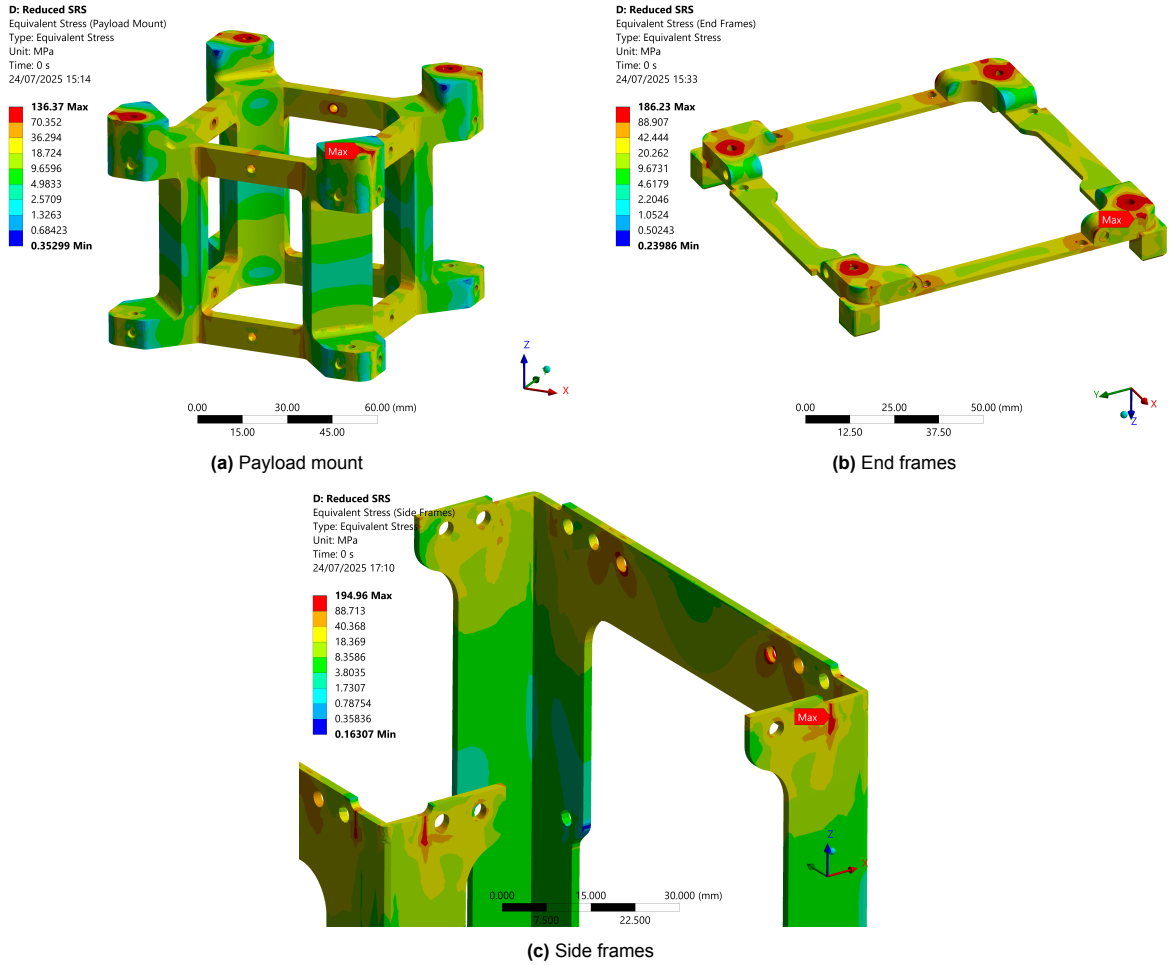


**(a)** Payload mount

**(b)** End frames

**(c)** Side frames

**Figure A.6:** New design and reduced SRS

## A.3. Thermoelastic Analysis

**Table A.3:** Thermoelastic analysis versions

| Version | Description |
|---|---|
| 1.0 | The check for isothermal expansion was performed on Version 2.0 of the vibrational analysis model. No constraints were applied to the model, and the analysis did not converge. |
| 1.1 | The ‘quasi-static solution’ option was enabled, and the analysis converged. However, the model had unusually high stresses of around 500 MPa. |
| 2.0 | The MPCs of RBE2 type were changed to RBE3, and all contacts were changed to frictionless. The stresses were much lower, but the maximum was still 5 MPa. |
| 2.1 | The ‘large deflections’ option was enabled, and the stresses were close to zero. |
| 2.0 | The entire procedure for this check was repeated for Version 5.0 of the vibrational analysis model, and as expected, the maximum stress was close to zero. |
| 3.0 | The actual input temperatures in Table 6.2 were applied to the components of the model, and the thermoelastic analyses described in Chapter 6 were performed. |

# B

# Mesh Convergence

In order to verify that the results of the FE analyses do not depend significantly on the mesh size, a mesh convergence study was performed on the first four natural frequencies and the maximum von-Mises stress from shock loads. The mesh sizes for the end frames, side frames, and payload mount were varied as shown in Table B.1, while the mesh sizes for the guide rods and the screws were constant values of 0.2 mm and 1 mm, respectively. Furthermore, all cases had local refinement applied at the same locations, such as load-bearing holes and the boundaries between components.

**Table B.1:** Mesh convergence cases

| Case | Mesh size [mm] | | | Nodes | Elements | Run time [s] |
|---|---|---|---|---|---|---|
| | End frames | Side frames | Payload mount | | | |
| 1 | 1.8 | 2.4 | 2.4 | 575,372 | 331,374 | 917 |
| 2 | 1.44 | 1.92 | 1.92 | 735,405 | 428,440 | 1,257 |
| 3 | 1.2 | 1.6 | 1.6 | 1,036,129 | 621,928 | 2,044 |
| 4 | 1.08 | 1.44 | 1.44 | 1,370,826 | 834,819 | 2,865 |

All cases produced 99 modes between 0 Hz and 10,000 Hz, and also had the maximum von-Mises stress from shock loads occurring at nearly the same locations on the side frame. As expected, the run time also increased significantly as the mesh size decreased. From Figure B.1, it can be observed that the first, second, third, and fourth natural frequencies show minimal variation of around 0.21%, 0.22%, 1.21%, and 1.22%, respectively. The stresses showed an unusual dip at first, but then showed a variation of only 1.15% between the third and fourth cases. A further decrease in the mesh size beyond that of the fourth case could not be analysed due to insufficient computational power. Hence, the mesh of the third case is considered to be converged, and all other FE analyses utilised this mesh.

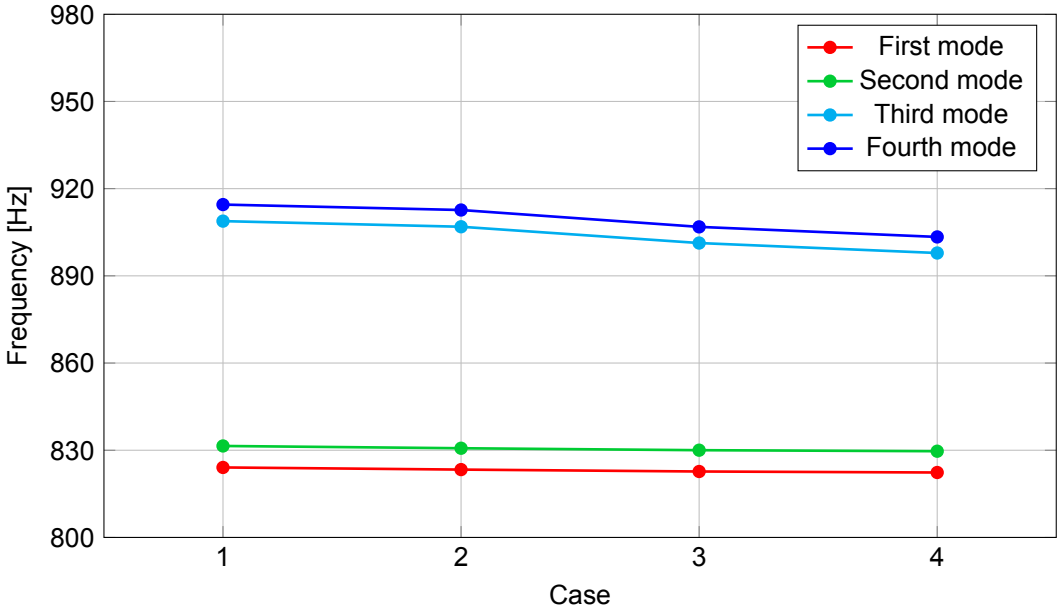


**(a)** Frequency results

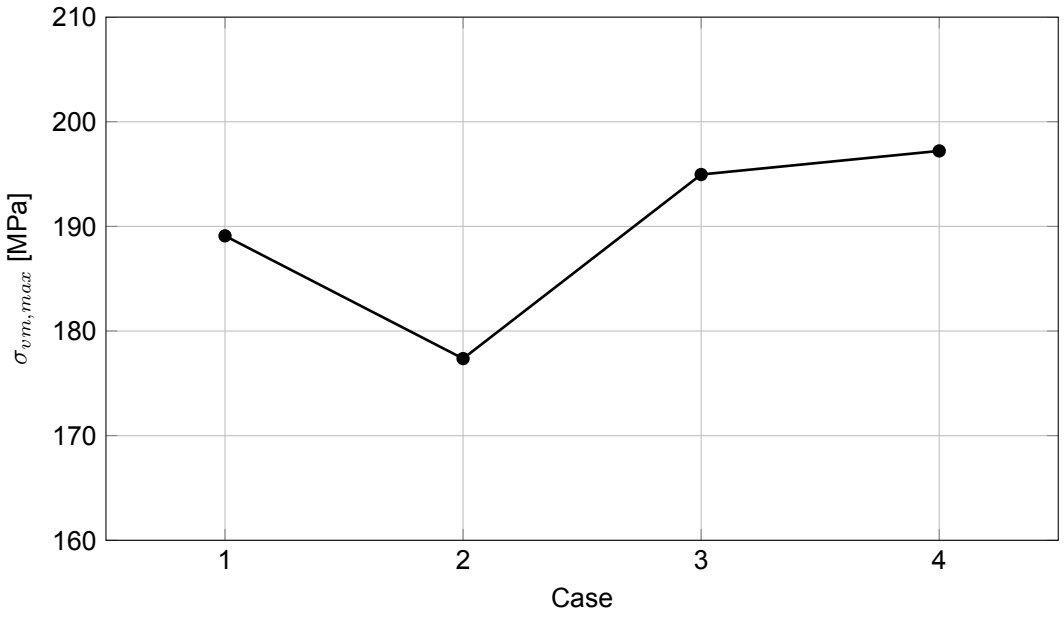


**(b)** Stress results

**Figure B.1:** Mesh convergence results

# C

# Pre-Stressed Analysis

## C.1. Modal Analysis

When there is pre-stress in a system, the change in stiffness is captured by adding a new stress stiffening matrix $\boldsymbol{S}$ to the stiffness matrix $\boldsymbol{K}$. Hence, the generalised eigenvalue problem is modified for a pre-stressed modal analysis as follows:

$$\left(-{\omega_n}^2 \boldsymbol{M} + \{\boldsymbol{K} + \boldsymbol{S}\}\right) \boldsymbol{U} = \boldsymbol{0}$$

The quasi-static load case, which showed the highest von-Mises stress, was considered for the pre-stressed modal analysis, although any of the other seven cases could have also been used, given their similar range of stress values. A total of 108 modes were found between 0 Hz and 10,000 Hz, compared to 99 when there was no pre-stress. Along with some of the first few mode shapes shown in Figure C.1, the first ten natural frequencies are shown in Table C.1. These frequencies were all clearly lower than the values of Table 5.8, but still higher than the minimum requirement of 115 Hz. The first mode shape had an effective mass fraction of 18.66% and was primarily due to the motion of the -$X$ face of the side frame, but also some motion from the payload mount. The third mode shape had an effective mass fraction of 27.20% and showed significant motion of the payload mount compared to the -$X$ face of the side frame. The fourth mode shape had an effective mass fraction of 14.30% and was only due to the motion of the +$X$ face of the side frame.

**Table C.1:** CubeSat natural frequencies after pre-stress

| Mode | Frequency [Hz] |
|---|---|
| 1 | 720.61 |
| 2 | 723.99 |
| 3 | 737.91 |
| 4 | 888.98 |
| 5 | 890.91 |
| 6 | 978.51 |
| 7 | 1,361.28 |
| 8 | 1,361.35 |
| 9 | 1,386.32 |
| 10 | 1,480.03 |

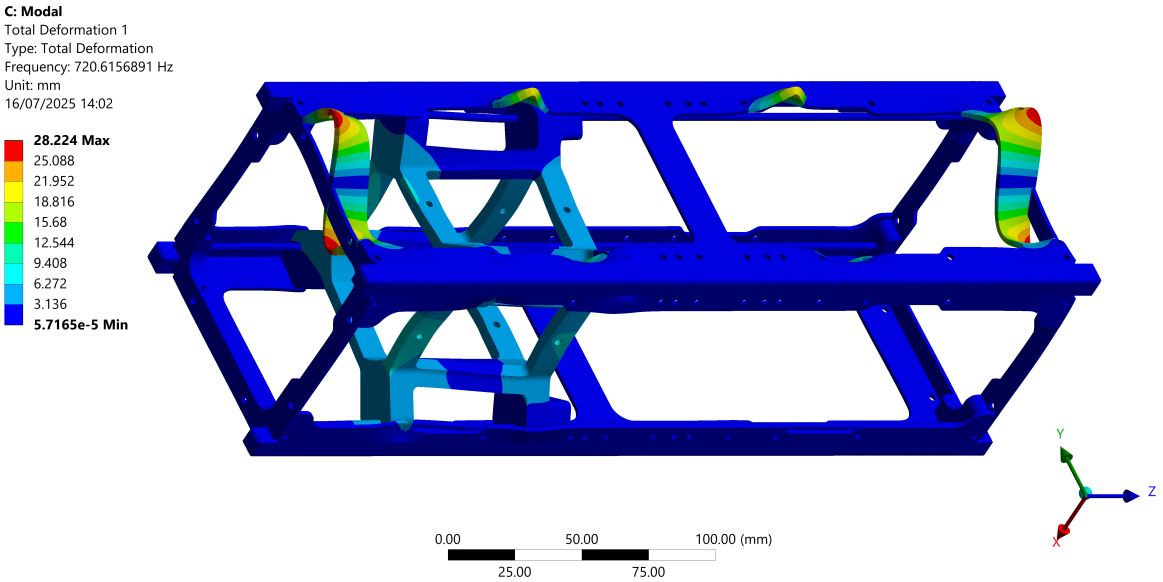


**(a)** First mode

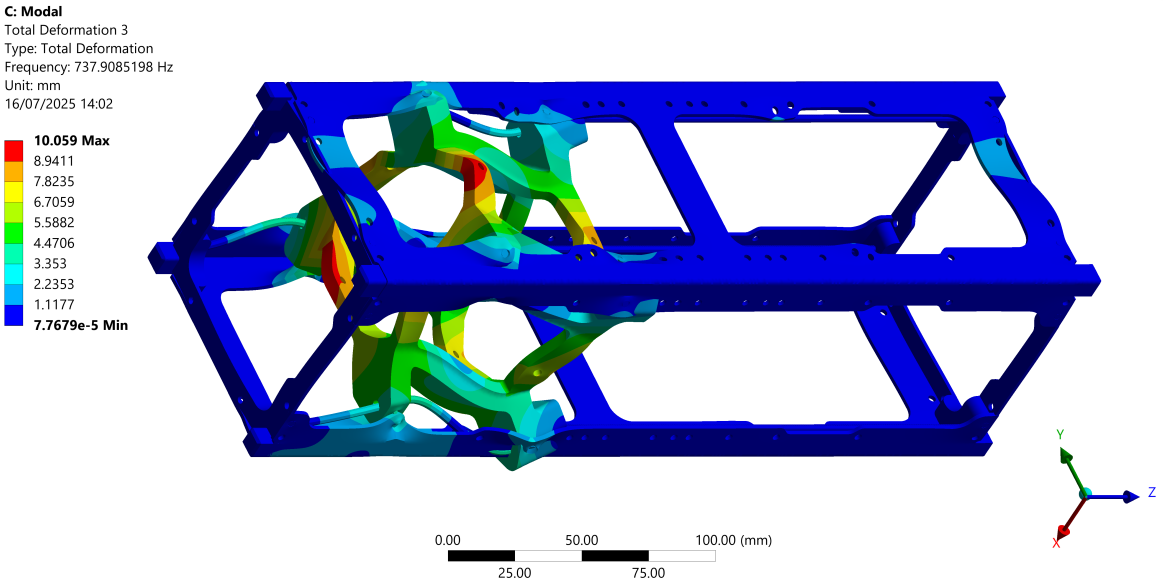


**(b)** Third mode

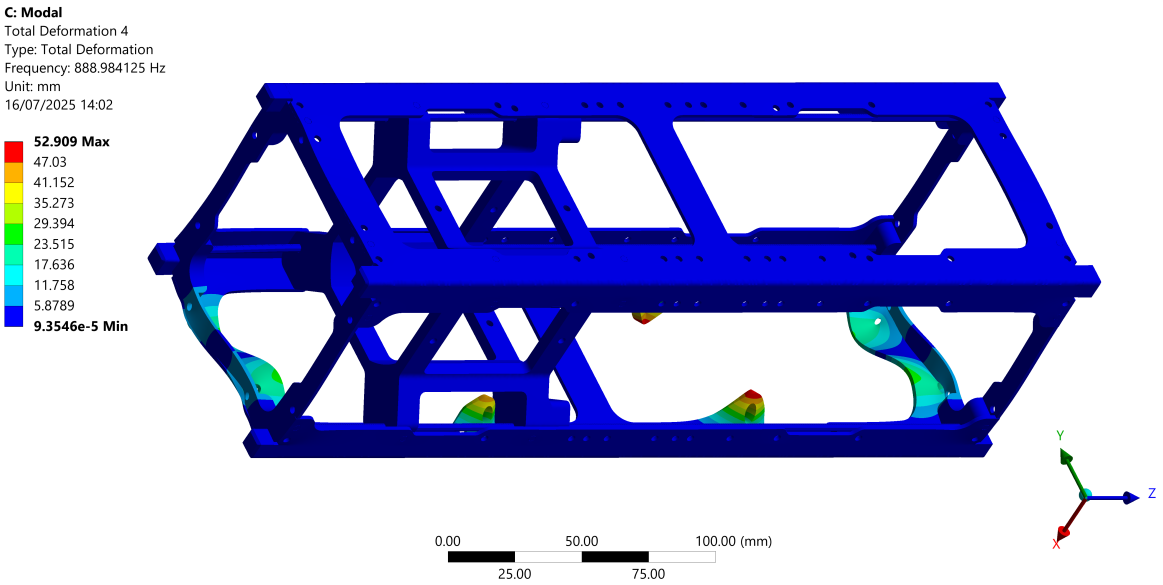


**(c)** Fourth mode

**Figure C.1:** Mode shapes after pre-stress

## C.2. Random Vibrations

A random vibration analysis using the acceleration PSD of Ariane 6 was also conducted on these results. As shown in Figure C.2, the 3-sigma level of the maximum von-Mises stress was found to be 64.22 MPa, which was slightly higher than the corresponding value without pre-stress, and the new $MOS$ was 2.43. Hence, the CubeSat withstands the random vibrations even when there is pre-stress.

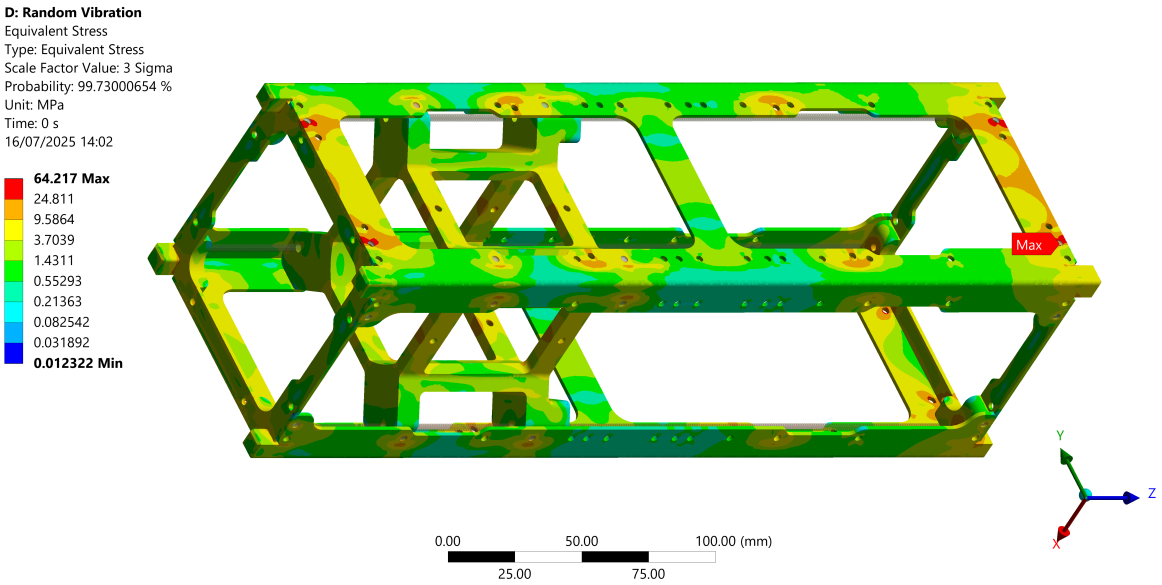


**(a)** Stress

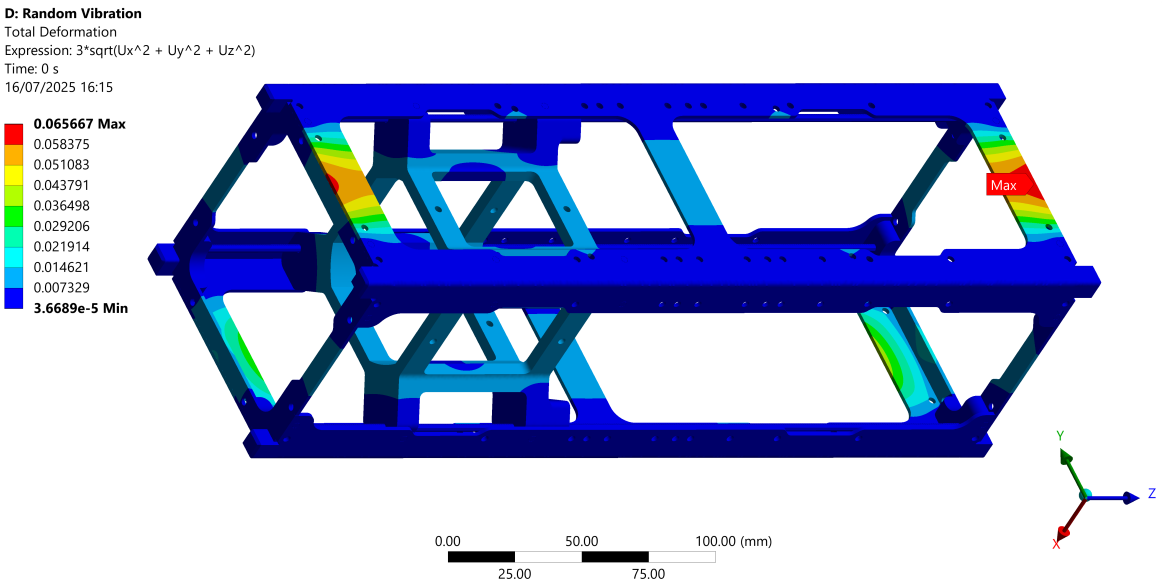


**(b)** Total deformation

**Figure C.2:** Random vibrations results after pre-stress

# D

# Analysis Checks

## D.1. Unit Load Reaction

A unit acceleration (1 $g$) was applied along each of the three axes separately, while fixed supports were applied to the external surfaces of the CubeSat rails opposite to the acceleration. This setup closely represents the different faces of the CubeSat resting on a flat surface under the Earth's gravity. Given that the total mass of the CubeSat was 5.402 kg, the reaction forces experienced by all the fixed supports should theoretically be equal to 5.402 × 9.80665 = 52.9755 N. From the analysis, the reaction forces were found to be 52.9680 N along each of the three axes, which differed by 0.01% from the theoretical value, thus implying that the FE model was free from discretisation errors. Figure D.1 shows the maximum von-Mises stress in the model for all three cases.

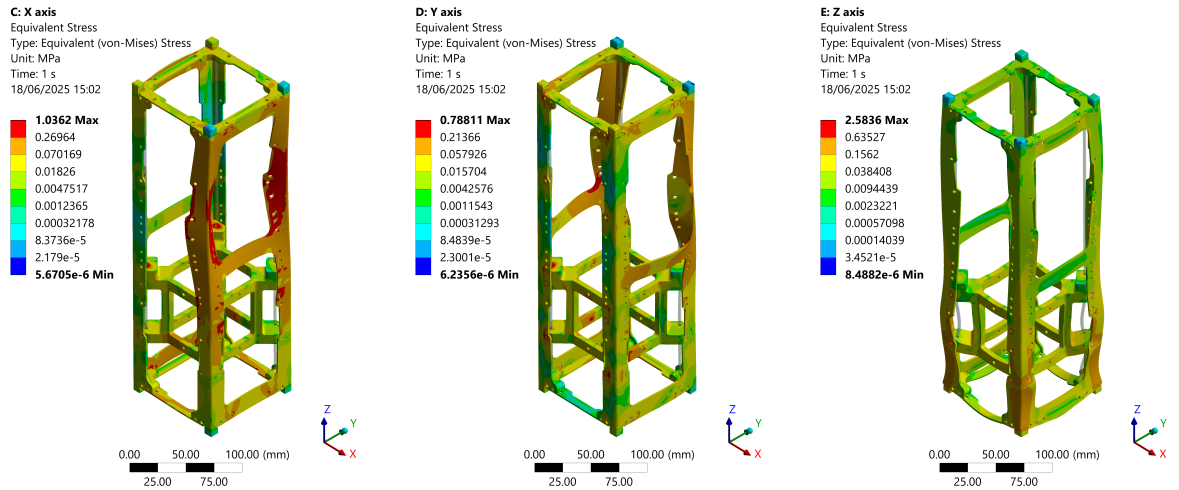


**(a)** Along $X$ axis **(b)** Along $Y$ axis **(c)** Along $Z$ axis

**Figure D.1:** Stresses from unit acceleration

## D.2. Rigid Body Modes

A three-dimensional FE model without internal mechanisms will show six rigid body modes, three of which are translations and three are rotations. These rigid body modes must have frequencies that are exactly 0, or close to 0 but not exceeding a typically agreed value of 0.005 Hz. As shown in Figure D.2, the frequencies of these rigid body modes in the current design were found to be 0 Hz, 0 Hz, 0 Hz, 0.0019 Hz, 0.0025 Hz, and 0.0079 Hz. Though the frequency of the sixth mode was comparatively high, it was still close to 0. Another check states that the ratio of the highest computed frequency of the rigid body modes and the lowest elastic mode frequency should be lower than an acceptable value of

$10^{-4}$. Upon looking at the sixth and seventh modes, having frequencies of 0.0079 Hz and 167.09 Hz, respectively, their ratio was computed as $4.72 \times 10^{-5}$. Hence, the FE model almost satisfies the first check, but completely satisfies the second check.

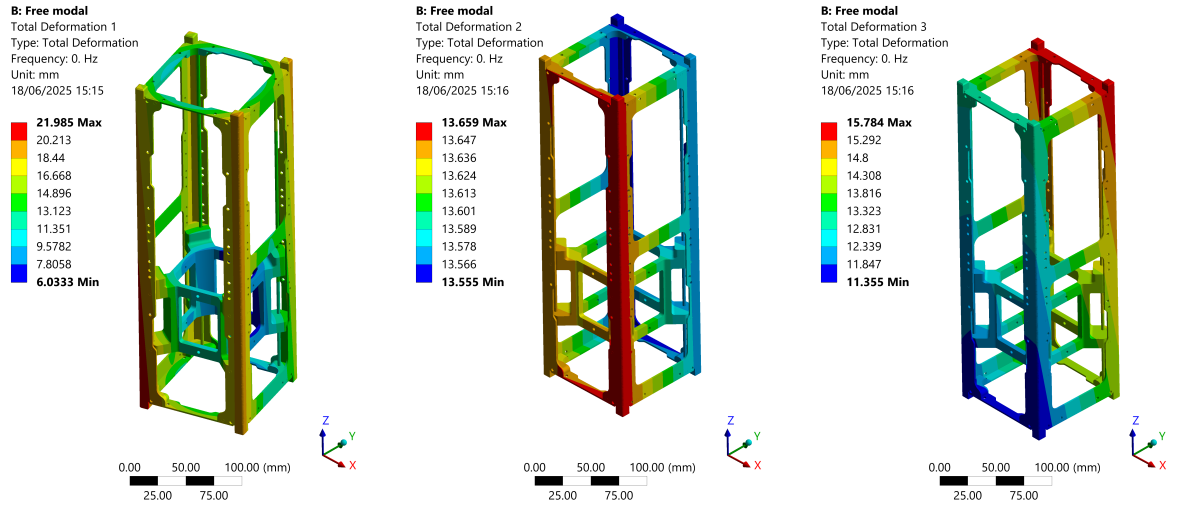


**(a)** First mode (rotation about $Z$ axis)

**(b)** Second mode (translation along $Z$ axis)

**(c)** Third mode (translation along $X$ axis)

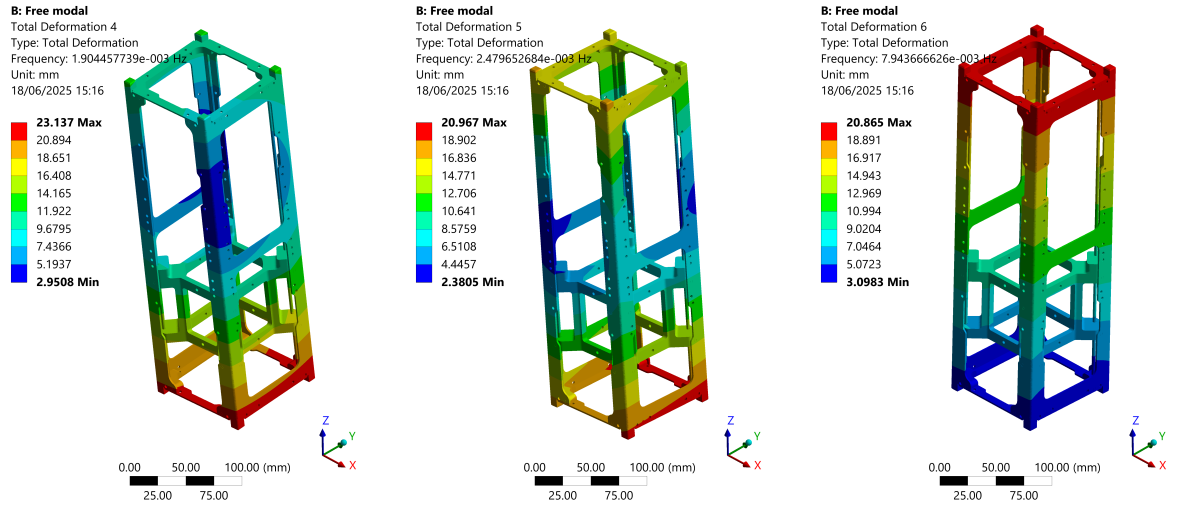


**(d)** Fourth mode (rotation about $X$ axis)

**(e)** Fifth mode (rotation about $Y$ axis)

**(f)** Sixth mode (translation along $Y$ axis)

**Figure D.2:** Rigid body mode shapes

## D.3. Isothermal Expansion and Contraction

This check is performed to ensure that, when the model is assigned a homogeneous and isotropic material and is submitted to an unconstrained isothermal expansion or contraction, the stresses do not exceed certain values. When Aluminium 7075-T6 alloy, having the properties in Table 4.1, was used as a dummy material for all components, along with a uniform temperature increase or decrease of 100 K applied to those components, the maximum von-Mises stress in the model should be less than 0.01 MPa. As shown in Figure D.3, these values were found to be $5.4 \times 10^{-4}$ MPa and $9.8 \times 10^{-4}$ MPa, for the expansion and contraction cases, respectively, thus satisfying the check.

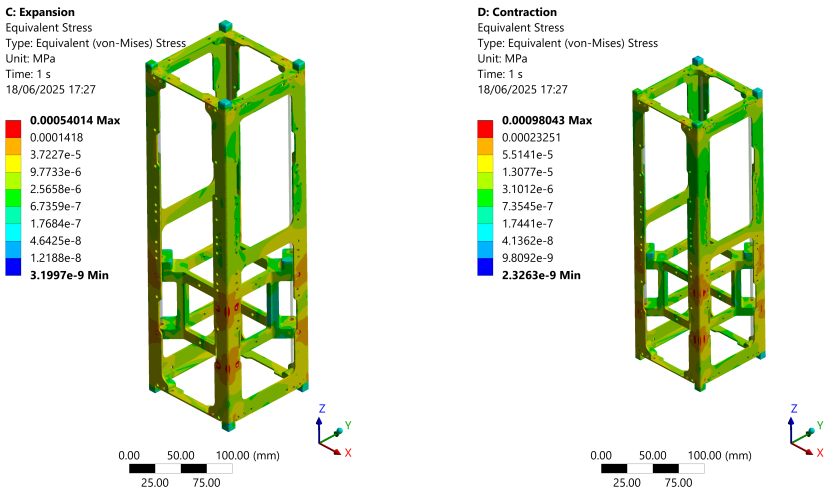


**(a)** Expansion **(b)** Contraction

**Figure D.3:** Isothermal thermoelastic stresses